

**Ultra-high Precision Scanning Beam
Interference Lithography and its Application
- Spatial Frequency Multiplication**

by

Yong Zhao

B.Eng., Mechanical Engineering, Tsinghua University, China (2002)

M.S., Mechanical Engineering, Massachusetts Institute of Technology,
(2004)

Submitted to the Department of Mechanical Engineering
in partial fulfillment of the requirements for the degree of

Doctor of Philosophy

at the

MASSACHUSETTS INSTITUTE OF TECHNOLOGY

[June 2008]

May 2008

© Massachusetts Institute of Technology 2008. All rights reserved.

Author

Department of Mechanical Engineering

May 8th, 2008

Certified by

Mark L. Schattenburg

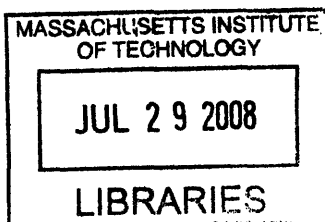
Senior Research Scientist

Thesis Supervisor

Accepted by

Lallit Anand

Chairman, Department Committee on Graduate Students



ARCHIVES

**Ultra-high Precision Scanning Beam
Interference Lithography and its Application
- Spatial Frequency Multiplication**

by

Yong Zhao

Submitted to the Department of Mechanical Engineering
on May 8th, 2008, in partial fulfillment of the
requirements for the degree of
Doctor of Philosophy

Abstract

Scanning beam interference lithography (SBIL) is a technique developed at MIT in 2003. The SBIL system, referred to as the Nanoruler, could fabricate grating patterns with around ten-nanometer phase repeatability. There were many factors which limit its precision and thus limit its utility for applications which require more precise phase control. In this thesis the main sources of error impairing the Nanoruler's patterning precision, which include thermal error of the environmental enclosure and the measurement error of a critical mirror in the stage interferometry system, have been identified. A digital PI-lead compensation controller has been designed to improve the air temperature stability of the environmental enclosure. A digital low-pass filter is utilized to reduce high spatial-frequency noise in the stage mirror non-flatness measurement. A factor that causes another kind of the mirror measurement error, which is an apparent location-dependent mirror non-flatness measurement, has been determined. A corresponding solution is developed to reduce this kind of error. Afterwards, as an application of ultra-high precision patterning, multiple-exposure SBIL is utilized to multiply the spatial frequency of patterns over large areas. The high nonlinearity of photo resists and the excellent pattern repeatability of the Nanoruler enable higher line densities to be achieved by applying a nonlinear process (development) between exposures of the Nanoruler. A phase control technique for accurately overlaying interference lithography exposures has been developed. Accurate phase control over large areas during spatial frequency multiplication by utilizing a surrounding alignment grating has been achieved. Three key factors- the angle, period, and phase of the alignment grating- have been accurately measured and utilized to position subsequent patterns with respect to previous patterns. Some factors that can dramatically diminish the accuracy of phase control, such as particle-induced substrate distortion and nonlinear distortion of the alignment grating, have also been considered and minimized in order to improve the accuracy of phase control. For spatial frequency doubling with a 574 nm principal pitch, we achieved overlay phase

errors with a mean of $-1.0 \text{ nm} \pm 2.8 \text{ nm}(1\sigma)$ between overlaid grating patterns over a $25 \times 32.5 \text{ mm}^2$ area. Utilizing the same technique, we fabricated 50 nm -pitch gratings with spatial frequency quadrupling starting from a principal pitch of 200 nm .

Thesis Supervisor: Mark L. Schattenburg
Title: Senior Research Scientist

To dad and mom

Acknowledgments

First of all I want to express my deepest gratitude to my advisor, Dr. Mark L. Schatternburg for his patience, encouragement, and guidance. I am extremely grateful to him for providing me with the opportunity to work on this project. Mark is a great advisor. His advice has significantly improved the quality of my research.

Special thanks to Prof. Kamal Youcef-Toumi and Prof. Warren P. Seering for serving as my thesis committee member. I benefitted a lot from their questions and suggestions.

Really appreciate Ralf, Chi, Mireille, Juan, Minseung, Bob, and Sara. Ralf and Juan gave me very helpful training on how to use the Nanoruler when I first joined the group. Chi works together with me on the spatial frequency multiplication project. Mireille very patiently helped me do the ProE simulation. Bob always provides support on mechanical devices and lab issues. Minseung is a very nice person and always helpful.

I am most grateful to my family in China who always supported and encouraged my work.

I furthermore deeply appreciate all the friendships I found here and who made my life throughly enjoyable. Finally, appreciate all my friends in China who gave me a lot of support and encouragement.

Contents

1	Introduction	21
1.1	Introduction	21
1.2	Motivation	21
1.3	Scanning beam interference lithography	22
1.3.1	Writing mode	24
1.3.2	Heterodyne reading mode and homodyne reading mode	29
1.4	Main sources of error affecting the precision of the SBIL system	32
1.5	Spatial frequency multiplication	33
1.6	Thesis structure	35
2	Thermal Issues	37
2.1	Introduction	37
2.2	Motivation	37
2.3	Thermal control of the environmental enclosure	38
2.3.1	The environmental enclosure of the Nanoruler	38
2.3.2	Measuring the transfer function	40
2.3.3	Controller Design	42
2.3.4	Performance of the thermal control system	44
2.4	Milli-degree temperature gradients mapping	46
2.4.1	Thermistor cross calibration and the self-heating effect	47
2.4.2	Mapping milli-degree temperature gradients	50
2.5	Summary	56

3	Mirror Non-flatness	59
3.1	Introduction	59
3.2	Measuring the X-stage mirror non-flatness	59
3.2.1	Position and angle measurements of the X-Y stage interferometer	62
3.2.2	The X-axis stage mirror non-flatness	70
3.2.3	Discrete measurement transfer function and mirror non-flatness results	74
3.3	High spatial-frequency noise in the mirror profile	76
3.4	Location-dependent mirror non-flatness	82
3.4.1	Twisting of optical bench with respect to the stage	84
3.4.2	Thermal errors along the X-axis stage interferometer beam paths	88
3.4.3	Granite table deformation	92
3.5	Summary	96
4	Spatial frequency multiplication - phase control	99
4.1	Introduction	99
4.2	Spatial frequency doubling process	99
4.3	Interference fringe phase control technique	102
4.3.1	Angle measurement of the alignment grating	105
4.3.2	Period measurement of the alignment gratings	109
4.3.3	Phase measurement and control of overlaid gratings	110
4.4	Experimental results	113
4.5	Substrate distortion issues	115
4.5.1	Particle-induced Substrate Distortion	115
4.5.2	The Nonlinear Distortion of the Alignment Grating	117
4.5.3	Pressure time-variance of the vacuum line of the chuck	118
4.6	Summary	119
5	Conclusions	121
A	Matlab Codes for Mirror Non-flatness Measurement	123

B Matlab Codes for Calculating Overlay Phase Error	127
C Procedure of Measuring Non-flatness of the X-axis Stage Mirror	133

List of Figures

1-1	Traditional Interference Lithography.	23
1-2	(a) Front view of the Nanoruler. (b) Rear view of the Nanoruler.	25
1-3	SBIL concept and writing scheme. (a) Concept of SBIL. (b) A small interference image is scanned over the substrate. (c) Intensity profile of the interference image. (d) Summed intensity of six overlapped scans.	26
1-4	The writing mode of the Nanoruler.	28
1-5	(a) The homodyne reading mode of the Nanoruler. (b) The heterodyne reading mode of the Nanoruler.	30
1-6	Two-beam single-exposure interference lithography.	33
2-1	Photograph of the inside of the environmental enclosure, which houses the Nanoruler. Temperature-controlled air leaves the ULPA filters and is directed towards the critical volume of the tool at the center.	39
2-2	Schematic of the enclosure showing air paths and temperature measurement points.	40
2-3	Thermal system control diagram including measurement points for determining the closed-loop frequency response.	41
2-4	Bode plot of measured system closed-loop frequency response, Y_2/Y_1	42
2-5	Bode plot of measured system open-loop transfer function for the thermal system, where ω_{pc} is the phase-crossover frequency.	43

2-6	Measured Bode plots of the open-loop transfer function for the lead-compensated and uncompensated system. ω_{uc} is the phase-crossover frequency of the uncompensated system and ω_c is the phase-crossover frequency of the compensated system.	44
2-7	Measured performance of the thermal control system (side B) without the PI controller. The thermal controller was turned on at time 0.	45
2-8	Diagram of the complete thermal control system. The portion inside the dashed area represents the digital controller. (a) The controller in s-domain. (b) The controller in z-domain.	46
2-9	Measured thermal system responses to a step input of the set point. . . .	47
2-10	Two hours of single-point temperature measurements of the thermal system. (a) Measured side B temperature with the system error. (b) Frequency content of measured side B temperature with the system sensor. (c) Measured side B temperature with an independent sensor. (d) Frequency content of measured side B temperature with the independent sensor.	48
2-11	Two hours of single-point side B temperature measurements of the thermal system with the system error. (a) Before the improvement of the thermal control. (b) After the improvement of the thermal control.	49
2-12	Schematic of calibration water bath.	52
2-13	Temperature measurements of 11 thermistor channels ($^{\circ}C$) over 9 hours in the thermal calibration bath.	52
2-14	Contour plots of relative temperatures ($m^{\circ}C$) over an an area 30 cm from the filter plane of air handler B. (a) Before the improvement of the single-point thermal control. (b) After the improvement of the single-point thermal control. The central rectangle represents the filter boundary, the circles represent the thermistor measurement positions, and the central cross represents the reference thermistor.	53

2-15	Standard deviation maps of temperatures ($m^{\circ}C$) over an an area 30 cm from the filter plane of air handler B. (a) Before the improvement of the single-point thermal control. (b) After the improvement of the single-point thermal control. The central rectangle represents the filter boundary, the circles represent the thermistor measurement positions, and the central cross represents the reference thermistor.	54
3-1	The column reference mirror, stage mirror, and interferometer head in the X-axis stage interferometry system.	61
3-2	The difference of the X-axis stage mirror non-flatness measurements on Nov. 19th 2007 and Aug. 24th 2007.	61
3-3	Demonstration of the effect of the X-axis stage mirror non-flatness time-dependent variation on pattern overlay.	62
3-4	The Zygo two-axis linear/angular column-reference interferometer system (the X-Y stage interferometer).	64
3-5	(a) Integrated displacement and angle interferometer head. (b) Schematic of integrated displacement and angle interferometer head.	65
3-6	Top view of the X-Y stage interferometer system without the column mirrors.	66
3-7	Definition of laboratory coordinates XY with origin O and stage coordinates UV with origin W. In the XY frame, the coordinates of point W is (x_w, y_w) . The coordinates of point K in the XY frame is (x_k, y_k) and in the UV frame is (u_k, v_k)	67
3-8	The X-axis and Y-axis stage mirrors with the X-Y stage interferometer heads.	68
3-9	The X-axis and Y-axis stage mirrors with the X-Y stage interferometer when there is rotation about point O'.	72
3-10	Zeroes and poles of $H(z)$	76
3-11	Zeroes and poles of $H_a(z)$. Zeroes are 0.99, -0.99, z_0 , z_0 , $-z_0$, $-z_0$ where $z_0 = 0.85e^{j\pi/2}$	77
3-12	The non-flatness measurement of the X-axis stage mirror.	78

3-13	(a) The non-flatness measurement of the X-axis stage mirror. (b) An exaggerated part of the X-axis stage mirror non-flatness measurement.	79
3-14	(a) Two sets of angle measurement $\Delta\theta$ before filtering, $\Delta\theta_1$ and $\Delta\theta_2$. (b) The $\Delta\theta$ measurement noise is $\Delta\theta_1 - \Delta\theta_2$. (c) Frequency content of $\Delta\theta_1 - \Delta\theta_2$. (d) Frequency contents of $\Delta\theta_1$ and $\Delta\theta_1 - \Delta\theta_2$	80
3-15	The solid line shows the transfer function $H(z)$; the dashed line shows its approximation $H_a(z)$	81
3-16	The 10th-order Butterworth low-path filter with the cutoff normalized frequency of 0.25. For the normalized frequency $\omega=0.5$, the attenuation of the filter is 65 dB.	82
3-17	The filtered angle measurement $\Delta\theta$ (top graph) and its frequency content (bottom graph).	83
3-18	(a) The non-flatness measurement of the X-axis stage mirror with a low-pass filter. (b) The exaggerated part of the X-axis stage mirror non-flatness measurement with a low-pass filter.	84
3-19	(a) The non-flatness measurement of the X-axis stage mirror without a low-pass filter. (b) The frequency content of the mirror non-flatness measurement in (a). (c) The non-flatness measurement of the X-axis stage mirror with a low-pass filter. (d) The frequency content of the mirror non-flatness measurement in (c).	85
3-20	The repeatability of measuring the X-axis stage mirror non-flatness.	86
3-21	(a) Non-flatness measurements of the X-axis stage mirror at $x=5$ mm, $x=150$ mm, and $x=300$ mm. (b) The difference of the mirror non-flatness measurements at $x=150$ mm with respect to that at $x=5$ mm and the mirror non-flatness measurements at $x=300$ mm with respect to that at $x=150$ mm.	87
3-22	The solid line represents the difference of the X-axis stage mirror non-flatness measurement at $x=150$ mm with respect to the measurement at $x=5$ mm with the original X-axis column mirror. The dotted line represents the same kind of difference with a mirror cover fixed in the front of the X-axis stage interferometer head.	88

3-23	Locations of four thermistors placed along the beam paths of the X-axis stage interferometer with equal spacing.	89
3-24	Six positions where the stage was located during temperature measurements.	90
3-25	Temperature measurements of the four thermistors when the stage is sequentially located at position 4-6.	92
3-26	The ProE simulation model.	93
3-27	The ProE simulation result for the Y-axis deformation of the granite table when the stage is at point A(x=300 mm, y=175 mm). Note the frame in the ProE simulation is defined differently with the XY frame. The z axis in the simulation is equivalent to the Y axis and the x axis of the simulation has the opposite direction with the X axis. The unit in the color bar is millimeter.	95
4-1	Schematic depiction of the spatial frequency doubling technique. (a) Spatial frequency doubling processing steps. (b) Phase control of spatial frequency doubling.	100
4-2	Schematic depiction of the alignment grating parameter measurement errors.	103
4-3	Demonstration that the angle difference between the scan direction and the interference fringes will increase the linewidth of grating patterns.	105
4-4	Scheme for measuring the angle (using path AB) and period (using path CE) of the alignment grating.	107
4-5	(a) The voltage measurements (raw data vs. filtered data) from the photodiode over 200 seconds for measuring the relative phase of the alignment grating at a single point. (b) The zoomed filtered measurements from the photodiode.	111
4-6	Electron micrographs of two-level overlay results. (a) Cross-section SEM image. The level 1 pattern has been etched into the silicon substrate. The level 2 pattern is exposed in the photoresist. (b) Top-view Raith image with the same configuration of the level 1 and level 2 patterns as (a). The photoresist is Sumitomo PFI-88 exposed with a wavelength of 351.1 nm.	114
4-7	Illustration of the cross-section SEM image.	115

4-8	Top-view electron micrographs of two-level overlay results, taken by Raith 150 over $20 \times 12.5 \text{ mm}^2$ with a grid size of 2.5 mm . Each electron micrograph area is approximately $1.5 \times 1.5 \text{ }\mu\text{m}^2$	116
4-9	2-D overlay phase error map (contours in nanometers) with a mean overlay error of $-1.0 \text{ nm} \pm 2.8 \text{ nm}$ (1σ).	117
4-10	50 nm-pitch grating patterns fabricated in MIT SNL and Intel 45-nm CMOS gate.	118
4-11	Depiction of substrate distortion due to particle between substrate and vacuum check.	118
4-12	2-D overlay phase error map (contours in nanometers) demonstrating particle-induced distortion.	119
4-13	(a) Pressure measurement of the chuck vacuum line in 10 minutes. (b) Grating phase measurement with the heterodyne reading mode at the same time.	120

List of Tables

1.1	The main sources of error affecting the precision of the SBIL system .	32
1.2	Overlay phase error budget	35
2.1	Cross calibration results of 11 thermistor channels	51
3.1	Non-flatness measurement errors of the X-axis stage mirror due to the temperature gradients among the beam paths of the X-axis stage interferometer.	90
3.2	The angle measurement error $\Delta\theta_e$ and the mirror non-flatness measurement error e due to the deformation of the granite table when the stage is at point A(x=300 mm, y=175 mm), B(x=150 mm, y=175 mm), C(x=300 mm, y=325 mm), and D(x=150 mm, y=325 mm). . .	94
3.3	The difference of the non-flatness measurements of the X-axis stage interferometer	96
3.4	The main sources of error affecting the patterning precision of the SBIL system	97
4.1	Errors of measuring alignment grating parameters	112

Chapter 1

Introduction

Scanning Beam Interference Lithography (SBIL) is a technique recently developed at the MIT Space Nanotechnology Laboratory (SNL). The current SBIL system, referred to as the Nanoruler, can fabricate periodic patterns over a large area (up to 12 inch substrates) with high phase fidelity.

1.1 Introduction

This chapter will first talk about the motivation to fabricate ultra-high precision patterns with the Nanoruler in Section 1.2. Next a brief introduction to the Nanoruler and some of its critical functions, which will help readers better understand the following chapters, will be made. Then Section 1.4 will identify the main sources of error limiting the precision of the interference lithography tool and points out which kinds of errors should be significantly reduced in order to achieve the desired precision. One application of ultra-high precision SBIL - spatial frequency multiplication, will be discussed in Section 1.5. In Section 1.6, the structure of the thesis will be summarized.

1.2 Motivation

Ultra-high precision periodic patterns (e.g., gratings and grids) fabricated by interference lithography tools have many applications. For example, the ultra-high precision

patterns can be applied in nanometrology as reference gratings to calibrate the coordinate frames of nano-imaging and metrology tools, or as metrology gratings in a position encoder (known as an optical encoder). Also these patterns over large areas can be used in high-resolution spectroscopy as diffraction gratings to collect incident x-rays.

Ultra-high precision patterns have another important application in nanomagnetic storage devices. Current, thin-film magnetic recording media is comprised of many small magnetic grains that are magnetically isolated but spatially connected [1], [2]. Increases in the recording density of hard disks will be limited by thermal instability (superparamagnetism) of the magnetic grains. The superparamagnetism limit has been predicted to occur at densities of $6 \sim 15 \text{ Gbit cm}^{-2}$ [3], [4]. Patterned recording medium, consisting of periodic grids of magnetic elements, is a promising medium for high-density magnetic recording (e.g., 150 Gbit cm^{-2}) [1]. Interference lithography, combined with magnetic material deposition and a pattern transfer process, is a technique to fabricate periodic grids of magnetic elements (also referred as to ordered magnetic nanostructures) [1], [5]. Another critical application of ultra-high precision gratings is to utilize the multi-exposure spatial frequency multiplication technique to fabricate high spatial-frequency gratings, which will be introduced in details in Section 1.5.

However, many sources of error limit the precision of the current Nanoruler, which will be discussed in Section 1.4. In this thesis, after identifying major sources of error that dramatically impair the precision of the Nanoruler, corresponding solutions in order to fabricate ultra-high precision patterns using the Nanoruler will be developed.

1.3 Scanning beam interference lithography

Scanning beam interference lithography (SBIL) is a new grating patterning technique recently developed in the Space Nanotechnology Laboratory aimed at patterning gratings with higher phase fidelity over larger area than "traditional" interference lithography (IL). Fig. 1-1 shows two "traditional" IL methods. In Fig. 1-1a, a UV

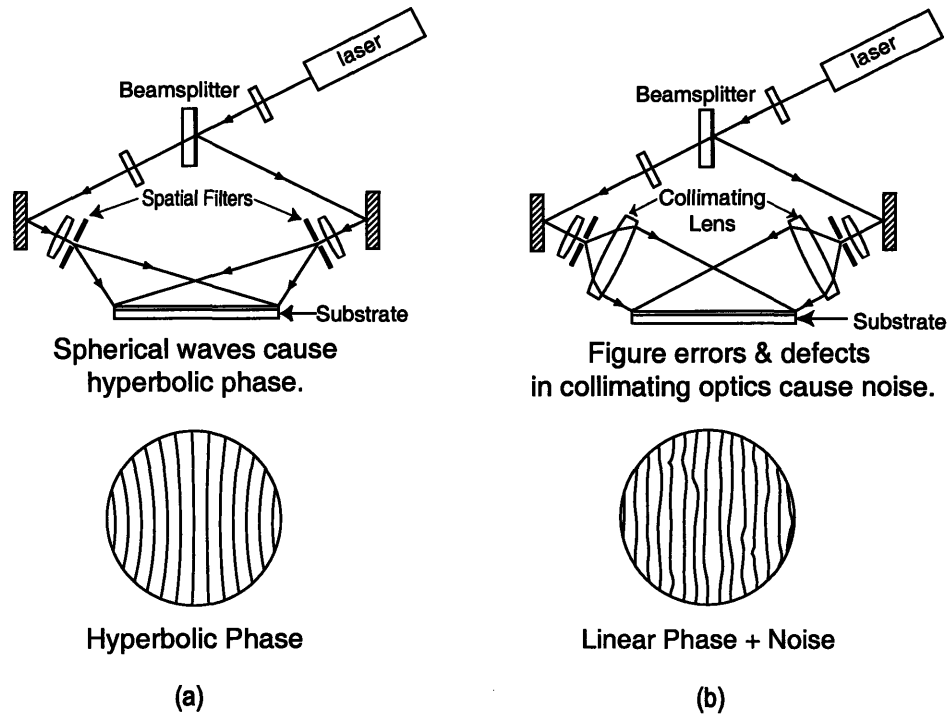


Figure 1-1: Traditional Interference Lithography.

laser beam is split into two coherent arms. These arms are filtered by spatial filters and expanded into spherical waves. Interference fringes in the overlapped spherical waves are utilized to fabricate gratings by a single exposure in UV-sensitive photoresist on the substrate. The spatial filters can attenuate wavefront distortion, but lead to undesirable hyperbolic phase curvature. To reduce the hyperbolic phase curvature, an alternative IL method (Fig. 1-1b) utilizes collimating lenses after the spatial filters. While the hyperbolic phase curvature disappears, some higher spatial-frequency phase errors are introduced due to manufacturing errors (also called figure errors) or defects in the collimating optics [6],[7].

The basic concept of SBIL is to use small diameter beams (about 1 mm^2) to generate interference fringes (also known as the interference image) and expose the interference image in the photoresist on the substrate that is scanned under the interference image by a high performance stage [6]. Due to the fact that the beams only pass a small area of the collimating lenses, the interference image has much

higher phase fidelity than that of "traditional" IL (Fig. 1-1b). Since the stage carries the substrate to be exposed under the interference image, we can write larger-area gratings, whose size is determined by the moving range of the stage, than the gratings patterned by "traditional" IL methods, whose size is determined by the size of the interference image.

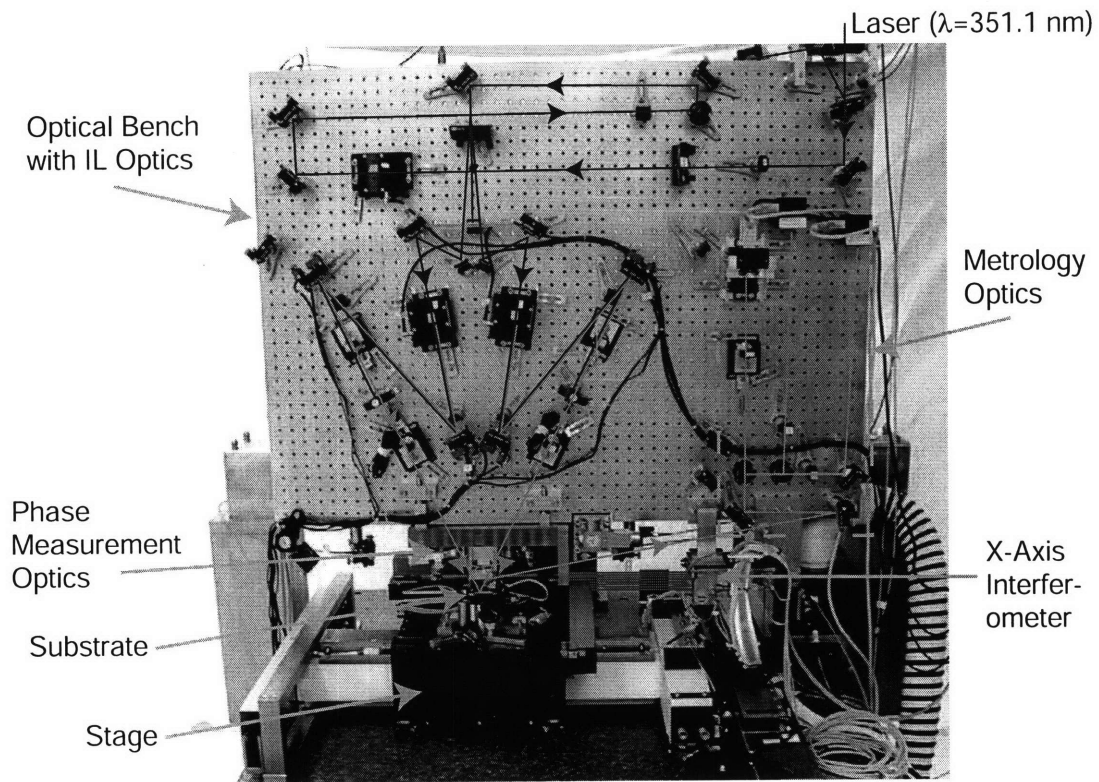
Fig. 1-2 shows the main parts of the Nanoruler, which sits inside an environmental enclosure. The environmental enclosure will be discussed in Chapter 2. A granite table is supported by an active vibration isolation system (Fig. 1-2b). A two-axis air-bearing stage is driven on the granite table by linear motors (Fig. 1-2a). A UV laser (CW 351.1 nm wavelength argon-ion laser) beam is directed into the enclosure by a beam steering system (Fig. 1-2b). As shown in Fig. 1-2a, IL optics and metrology optics are fixed on a vertical bench, and phase measurement optics are attached underneath the bench. An X-Y stage interferometry system, which consists of an X-axis stage interferometer (Fig. 1-2a) and a Y-axis stage interferometer (Fig. 1-2b), is used to measure the stage position. More details about the X-Y stage interferometry system are in Chapter 3. Next a brief review of writing mode and reading mode in the Nanoruler will be given. In the writing mode, the Nanoruler is utilized to pattern gratings on the substrate. In addition to fabrication, the Nanoruler has also functionality (reading mode) to measure phases of previously patterned gratings.

1.3.1 Writing mode

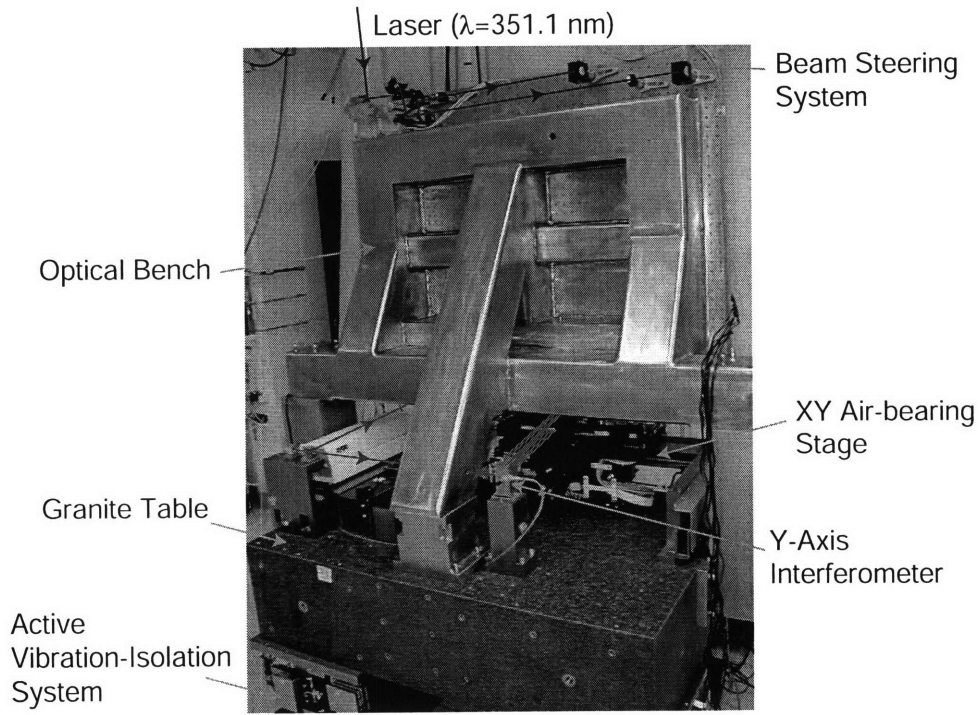
As shown in Fig. 1-3a, a UV laser (CW 351.1 nm wavelength argon-ion laser) beam is split by a grating beam-splitter to generate two coherent beams. These two beams interfere on the substrate surface and result in the interference image. The grating period of the interference image is given by

$$p = \frac{\lambda}{2 \sin \theta}, \quad (1.1)$$

where p is the grating period of the interference image, λ is the wavelength of the UV laser, and θ is the half-angle between the beams. Fig. 1-3b shows one of scanning

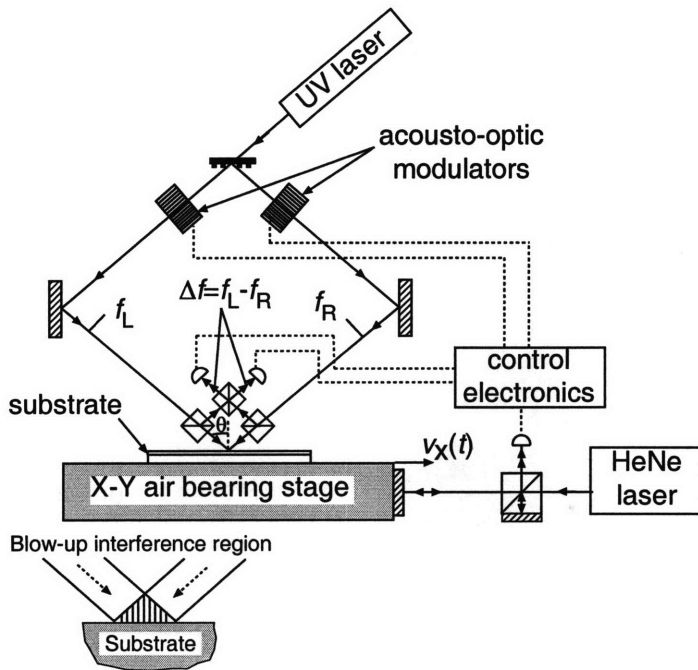


(a)

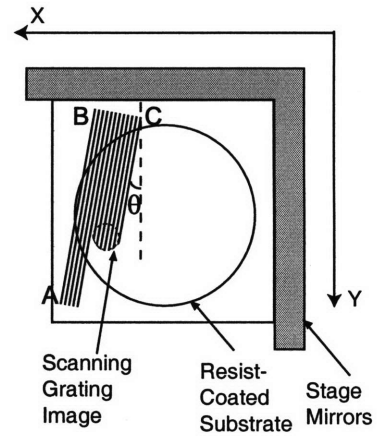


(b)

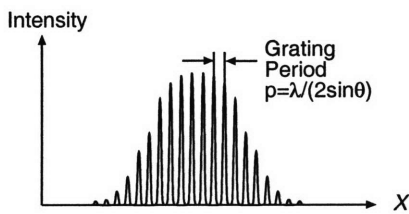
Figure 1-2: (a) Front view of the Nanoruler. (b) Rear view of the Nanoruler.



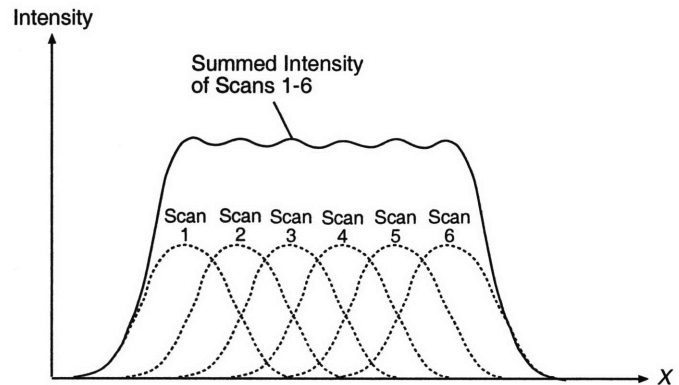
(a) Concept of SBIL



(b) Scanning scheme (parallel scanning)



(c) Interference image intensity profile



(d) Overlapping scans closely approximate a uniform intensity distribution

Figure 1-3: SBIL concept and writing scheme. (a) Concept of SBIL. (b) A small interference image is scanned over the substrate. (c) Intensity profile of the interference image. (d) Summed intensity of six overlapped scans.

schemes of the Nanoruler, called parallel scanning. A substrate sitting on the stage is scanned from point A to point B with a constant velocity. At the end of the scan, the stage steps over by an integer number of grating periods to point C and starts a new scan with an opposite scanning direction. In this way, the interference image will be exposed in the photoresist of the whole scanning area on the substrate. A fringe locking controller is used to stabilize the interference image with respect to the substrate when scanning the stage. As shown in Fig. 1-3c, the scanning interference image has a Gaussian intensity envelope since we interfere Gaussian beams. A uniform exposure dose is achieved by overlapping subsequent scans. Fig. 1-3d shows the interference image intensity envelopes of six individual scans in dashed lines and the summed intensity of these six overlapped scans in the solid line. For example, a step size of 0.9 times the Gaussian beam $1/e^2$ radius produces dose uniformity of better than 1% [6],[7], where e is the base of the natural logarithm.

It is very critical to stabilize the interference image with respect to the substrate during the exposure. A fringe locking control technique has been developed for this purpose. Before going through this technique, a few words will be spent to introduce acousto-optic modulators (AOM), which are utilized in the Nanoruler to modulate frequencies of the coherent beams. AOM is a device that uses the acousto-optic effect to diffract and shift the frequency of the incoming light by utilizing acoustic waves (usually at radio-frequency) across a crystal. In our application, as shown in Fig. 1-4, a frequency synthesizer generates radio-frequency (RF) signals to drive AOM1, AOM2, and AOM3. The AOM3, modulated by $f_R = 120 \text{ MHz}$, splits a weak reference beam of frequency $f_0 + f_R$ from the incident laser beam whose frequency $f_0 = 854.46 \text{ THz}$. The coherent left and right arms, which are generated by a beam splitter, are both modulated by $f_1 = f_2 = 100 \text{ MHz}$. The phase meter Φ_1 measures the phase difference between the left arm and the reference arm. The phase meter Φ_2 measures the phase difference between the right arm and the reference arm. The phase difference between the left and right arms $\Phi_1 - \Phi_2$ is calculated in a high-speed digital signal processor (DSP) by subtracting the measurements of the two phase meters.

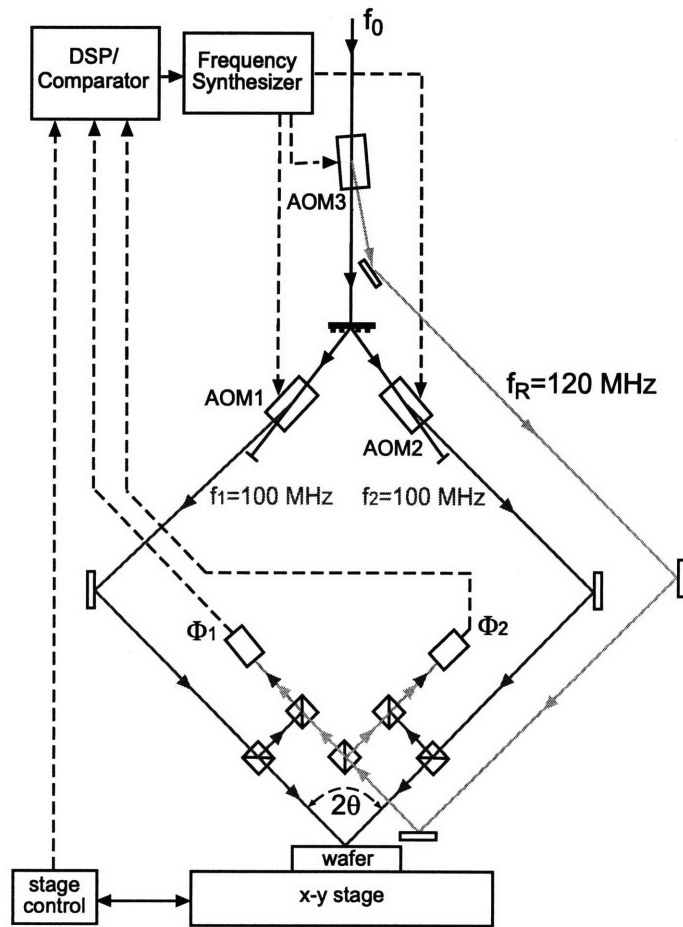


Figure 1-4: The writing mode of the Nanoruler.

During parallel scanning, the stage position error along the direction perpendicular to grating lines of the interference image is measured by a stage interferometry system (for details of the stage interferometry system, please see Section 3.2.1) and fed into the DSP. The DSP can change the frequency of the left arm by driving AOM 1 through the frequency synthesizer to change the phase difference between the left and right arms. In order to avoid printing the stage position error in grating patterns, the DSP controls the phase difference between the left and right arms such that,

$$\Phi_1 - \Phi_2 - \frac{2\pi}{p} \cdot [(x_{actual} - x_{goal})\cos\theta + (y_{actual} - y_{goal})\sin\theta] = const \quad (1.2)$$

where $\Phi_1 - \Phi_2$ is the phase difference between the left and right arms, p is the grating period of the interference fringe, θ is the angle of new grating lines with respect to the Y axis, x_{actual} and x_{goal} are respectively the actual and desired stage positions along the X axis, and y_{actual} and y_{goal} are respectively the actual and desired stage positions along the Y axis. The laboratory frame XY is defined in Section 3.2.1. The fringe locking technique assures gratings patterned with high phase fidelity of several nanometers over large areas (e.g., 12 inch substrates).

1.3.2 Heterodyne reading mode and homodyne reading mode

One powerful functionality in the Nanoruler is to measure the phase of patterned gratings. We name this feature as the reading mode of the Nanoruler. Depending on the phase detection scheme, there are homodyne and heterodyne reading modes in the Nanoruler.

For the homodyne reading mode, as shown in Fig. 1-5a, the left and right interference arms, both modulated by 100 MHz, are incident upon the patterned grating. The superimposed reflected right arm and back-diffracted left arm are detected by a photodiode. The voltage measurement of the photodiode represents the intensity of the combined beams, which is dependent on the phase difference between the incident left arm and the reflected right arm plus the phase of the grating pattern. With the assumption that the reflected right arm has the same phase as the incident

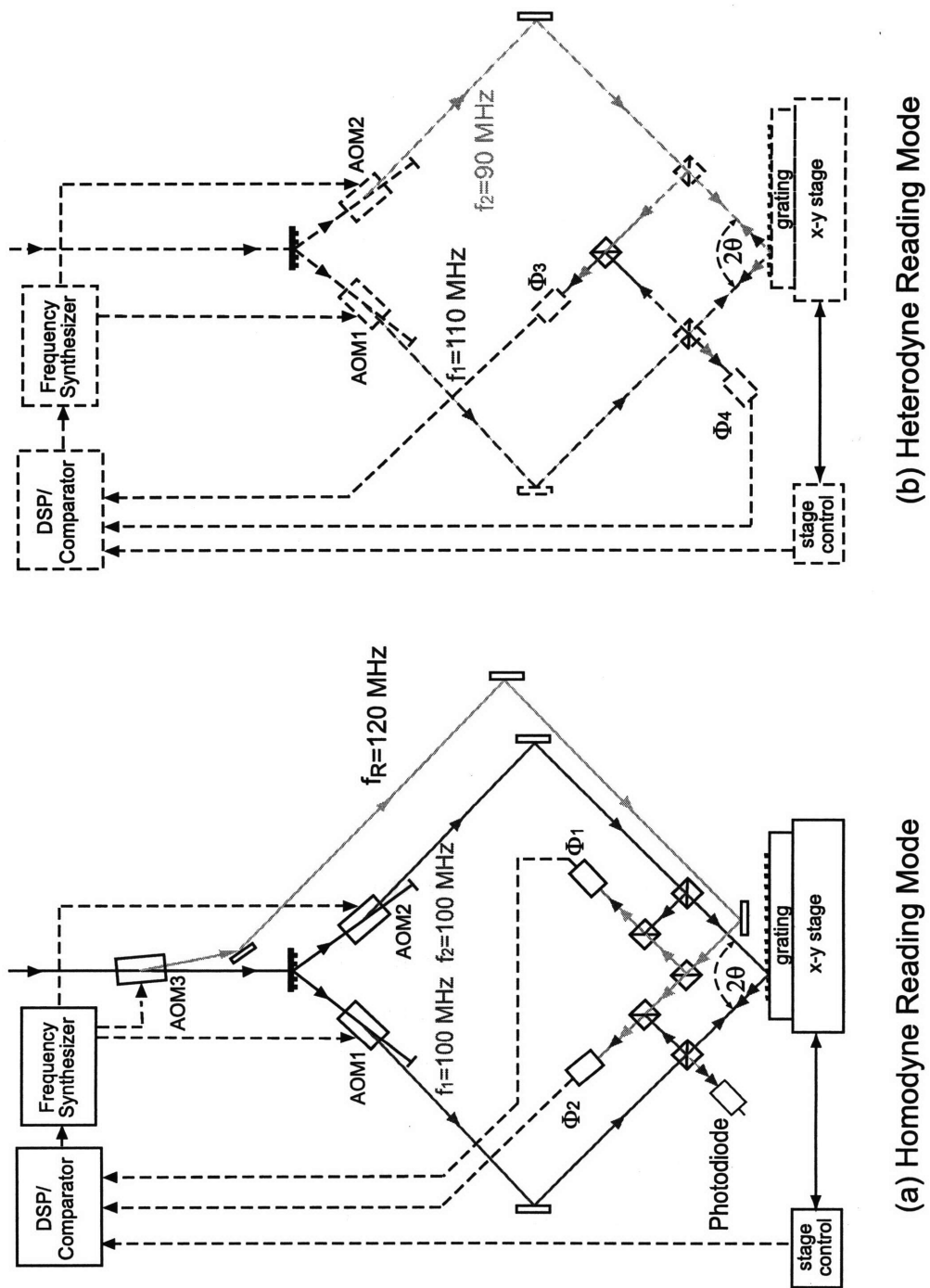


Figure 1-5: (a) The homodyne reading mode of the Nanoruler. (b) The heterodyne reading mode of the Nanoruler.

right arm [9], the phase difference between the incident left arm and the reflected right arm is equal to the phase difference between the left and right incident arms. From Equation (1.2), we know the fringe locking controller always drives this phase difference to $[(x_{actual} - x_{goal})\cos\theta + (y_{actual} - y_{goal})\sin\theta] \cdot 2\pi/p$. And x_{actual} and y_{actual} are respectively driven to x_{goal} and y_{goal} by the stage controller. Therefore, the phase of the grating can be detected by measuring the voltage readout from the photodiode (see Section 4.3 for details) when moving the stage.

For the heterodyne reading mode (Fig. 1-5b) [10], the left interference arm is modulated by 110 MHz and the right interference arm by 90 MHz. The phase difference between the incident left arm and the incident right arm is detected by phase meter Φ_3 ,

$$\Phi_3 = \Theta_L^i - \Theta_R^i \quad (1.3)$$

where Φ_3 is the phase measurement of phase meter Φ_3 , Θ_R^i is the phase of the incident right arm, and Θ_L^i is the phase of the incident left arm. Phase meter Φ_4 detects the phase difference between the back-diffracted left arm and the reflected right arm,

$$\Phi_4 = \Theta_L^d - \Theta_R^r \quad (1.4)$$

where Φ_4 is the phase measurement of phase meter Φ_4 , Θ_L^d is the phase of the back-diffracted left arm, and Θ_R^r is the phase of the reflected right arm. As we know, the phase of the back-diffracted left arm (Θ_L^d) is the summation of the phase of the incident left arm (Θ_L^i) and the phase of the grating pattern ($\Theta_{grating}$),

$$\Theta_L^d = \Theta_L^i + \Theta_{grating} \quad (1.5)$$

Since the reflected right arm has the same phase as the incident right arm, the phase of grating pattern can be calculated by subtracting the measurement of phase meter Φ_3 from the measurement of phase meter Φ_4 .

$$\Theta_{grating} = \Phi_4 - \Phi_3 \quad (1.6)$$

1.4 Main sources of error affecting the precision of the SBIL system

Table 1.1: The main sources of error affecting the precision of the SBIL system

Error Category	Corresponding Error (before my work)	Comments
X-axis stage mirror non-flatness measurement errors	~ 10 nm	
Changes in the refractive index of air	4.5 nm	for 300 mm substrate; ± 8 m°C thermal control
Thermal expansion of the substrate chuck	2.9 nm	for 300 mm substrate; ± 8 m°C thermal control
60 Hz noise	1.1 nm	
Phase distortion of interference fringes	~ 1 nm	
Total	~ 11 nm	

In this section the main sources of error impairing the precision of the Nanoruler before my PhD research will be discussed, which are listed in Table 1.1. The non-flatness measurement errors of the X-axis stage reference mirror could cause more than 10 nm phase error in the grating patterns when we utilize the mirror non-flatness information to make real-time correction during patterning, which I will address in Chapter 3. The errors due to air refractive index change and thermal expansion of the substrate chuck will be discussed in Chapter 2. 60 Hz noise causes 1.1 nm preci-

sion error [8], which is introduced in the Nanoruler by a variety of electrical devices. Dr. Chen discussed phase distortion of interference fringes in the Nanoruler [9]. The printed phase error of the interference fringes was less than 1 nm when stepping the stage with a step size of $1R=0.96$ mm (R is the Gaussian beam $1/e^2$ radius) during the exposure. Ultra-high precision patterns will be applied in spatial frequency multiplication. Based on the overlay error budget of the spatial frequency multiplication, which will be discussed in the next section, the precision of patterning gratings with the Nanoruler is required to be 3 nm. In order to achieve this precision, two major sources of error have to be significantly reduced. One of them is the non-flatness measurement error of the X-axis stage mirror in the stage interferometry system. Another is the thermal error inside the environmental enclosure of the Nanoruler.

1.5 Spatial frequency multiplication

High spatial-frequency periodic patterns have many applications in various fields. For example, high density patterns can be applied in nano-magnetics as magnetic storage media. In precision metrology, periodic patterns with fine pitch can be utilized as reference gratings. There are also important applications for high spatial-frequency patterns in nano-photonics.

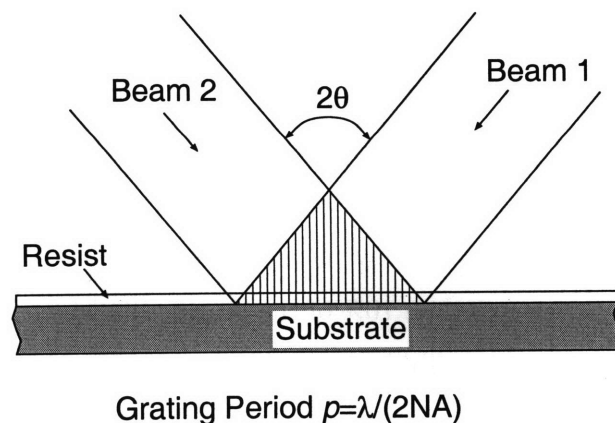


Figure 1-6: Two-beam single-exposure interference lithography.

For two-beam single-exposure interference lithography (Fig. 1-6), the period of

the interference pattern is given by $\lambda/(2n \sin \theta)$, where λ is the laser wavelength, n is the refractive index of the lithography medium, and θ is the half-angle of the interfering beams. The maximum spatial frequency of a single-exposure grating pattern is $2n/\lambda$ [28]. Higher spatial-frequency patterns can be fabricated by decreasing λ (e.g., by using shorter wavelength lasers) or increasing n (e.g., immersion lithography). However, these methods are both costly and have ultimate limits. Spatial frequency multiplication is an alternative method for achieving higher spatial-frequency patterns by interleaving new patterns among previous ones. At least three kinds of spatial frequency multiplication techniques have been developed over the past 30 years. Near-field lithography multiplies the spatial frequency of mask grating patterns based on the near-field properties of grating diffraction [29], [30]. Another technique is process-based spatial frequency multiplication, which has been used to fabricate sub-200-nm pitch gratings [31], [32]. Multi-exposure spatial frequency multiplication can extend the spatial frequency of patterns with integer factors 2, 3, 4, by applying a pattern transfer process between exposures [33], [34], thanks to the nonlinearity of modern photoresists which provide a sharp threshold between exposed and unexposed regions. Compared to previous techniques of multiplying the spatial frequency of IL-generated patterns, the technique reported here is able to perform spatial frequency multiplication over large areas with small phase errors.

Our research goal of spatial frequency multiplication is to fabricate 50 nm - period grating patterns with a grating linewidth of about 30 nm. One challenge is how to accurately place new grating patterns having some certain phase shift with respect to previous ones, which is also referred to as overlay phase control. In semiconductor industry, people usually choose overlay phase control error as 10 – 30% feature size. Here I set 1σ overlay error less than 10% of the grating linewidth, which is 3 nm. The overlay error budget is listed in Table 1.2.

In chapter 2 and 3 some techniques will be developed to reduce the Nanoruler patterning error and X-axis stage mirror time-dependent variation error to meet the error budget. In Chapter 4 I will discuss the multi-exposure spatial frequency multiplication technique developed in our lab and especially focus on reducing the alignment

Table 1.2: Overlay phase error budget

Error Category	Overlay positioning error budget (3σ)	Comments
Nanoruler patterning error	3 nm	affects alignment layer and two overlaid layers
X-axis stage mirror time-dependent variation error	~ 2 nm	
Alignment grating parameters measurement error	< 2 nm	affects two overlaid layers
Substrate distortion error	< 5 nm	affects two overlaid layers
Total	< 9 nm	

grating parameter measurement error and substrate distortion error.

1.6 Thesis structure

Chapter 2 discusses reducing thermal fluctuations of the environmental enclosure of the Nanoruler, which is one of the main sources of error affecting the patterning precision of the Nanoruler. Based on the measured open-loop transfer function of the thermal control system, a digital PI-lead compensation controller is designed to achieve sub-millidegree air temperature stability (i.e., 0.7 millidegree, 1σ) at a single point inside the enclosure over 2 hours. The temperature gradients over some critical planes inside the enclosure were measured with a sub-millidegree accuracy before and after the improvement of thermal control.

Chapter 3 first introduces a technique to measure the non-flatness of the X-axis stage mirror, which was developed by Juan Montoya, a previous PhD student in our lab. There were two kinds of measurement errors for the X-axis stage mirror non-flatness, which would impair the precision of the Nanoruler when using the profile measurement of the X-axis stage mirror to correct its non-flatness. One kind of measurement error is high spatial-frequency noise in the mirror non-flatness measurements. A digital low-pass filter is designed to reduce it. Several experiments have been carried out to determine what caused another kind of measurement error, which is an apparent location-dependent mirror non-flatness measurement. A corresponding solution was developed to reduce this kind of error.

After achieving ultra-high precision in the Nanoruler, multi-exposure spatial frequency multiplication is performed. Techniques to accurately place patterns with respect to previous patterns on the substrate are developed (here mainly discuss how to reduce the alignment grating parameters measurement error and substrate distortion error). For spatial frequency doubling with 547 nm principal pitch, overlay results between two layers of grating patterns over a $25 \times 32.5 \text{ mm}^2$ area will be shown. A 50 nm-pitch grating patterns with spatial frequency quadrupling of a 200 nm-pitch grating pattern will be shown at the latter of this chapter.

Chapter 2

Thermal Issues

2.1 Introduction

This chapter will discuss a technique to reduce the patterning errors of the Nanoruler due to thermal issues and address a method to rapidly and accurately map temperature gradients over large volumes. Section 2.2 will talk about the motivation. Section 2.3 will discuss a technique for improving the thermal control of an environmental enclosure designed for a precision lithography tool [8],[16],[17] to drive the single-point one-sigma temperature stability down to sub-millidegree levels is reported. In Section 2.4 a method for rapidly monitoring and mapping temperature gradients over critical areas inside the environmental enclosure will be developed. This chapter will be summarized in Section 2.5.

2.2 Motivation

Thermal control of environmental enclosures will become increasingly critical as precision metrology, lithography and machining systems require sub-nanometer tolerances. For the Nanoruler, the primary deleterious effects of air temperature fluctuations on tool precision are errors in interferometer beam paths and the thermal expansion of the workpiece. According to the updated Edlen equation for the refractive index of air with $\lambda = 633.0 \text{ nm}$ [11], for the laboratory conditions of one atmosphere pressure

(101.325 *kPa*), 50% relative humidity, and temperatures close to 20 °C, the linear approximation of the air refractive index, n , with respect to temperature, T , in degrees centigrade is

$$n = 1 + 2.713740 \times 10^{-4} - 9.298 \times 10^{-7}T \quad (2.1)$$

For example, thermal control within ± 0.01 °C, which is typical for state-of-the-art equipment, will cause a change of ± 9.3 *ppb* in the refractive index of air. This change will result in a ± 2.8 *nm* stage interferometer error for 300 *mm* stage translation. For a 300 *mm* wafer chuck, ± 0.01 °C thermal control will cause a ± 1.8 *nm* thermal expansion error for a super-invar chuck and a ± 0.16 *nm* thermal expansion error for a Zerodur chuck. For the same geometry and environmental conditions, improved thermal control to within ± 0.001 °C (1 *m°C*) can reduce the stage interferometer error to ± 0.28 *nm* and the thermal expansion error to ± 0.18 *nm* for a super-invar chuck and ± 0.016 *nm* for a Zerodur chuck.

Some thermal control systems have achieved temperature stability of millidegrees or better by using air-flow standard cell enclosures [12],[13] or enclosures utilizing flowing water as the thermal control medium [14]. Within large-volume air-flow enclosures, one-sigma air temperature stability of $2 \sim 3$ *m°C* at a single point has been demonstrated [8],[15].

2.3 Thermal control of the environmental enclosure

In the section, a technique to achieve sub-millidegree air temperature stability for the enclosure by utilizing a PI-lead compensation controller, which is designed based on the measured transfer function of the thermal system, will be discussed.

2.3.1 The environmental enclosure of the Nanoruler

Our environmental enclosure (see Fig. 2-1), whose internal dimensions are approximately 2.0-m long \times 1.7-m wide \times 2.1-m high, consists of two identical air handler

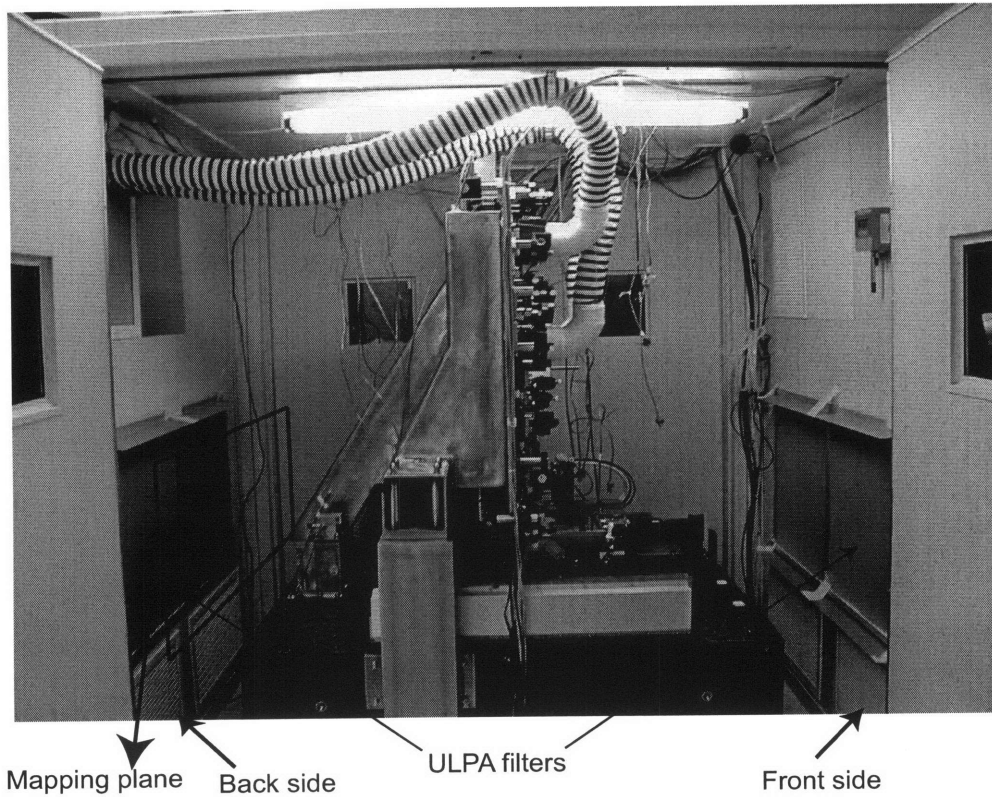


Figure 2-1: Photograph of the inside of the environmental enclosure, which houses the Nanoruler. Temperature-controlled air leaves the ULPA filters and is directed towards the critical volume of the tool at the center.

units [8]. As shown in Fig. 2-2, in each unit thermally controlled air is forced into the chamber in the center through 1.1-m by 0.56-m ULPA filters and returns through grills located at the top and bottom of the chamber. The air leaves the filters in laminar flow with velocity of approximately 1 m/s and is situated to bathe the critical volume of the lithography tool with well-controlled temperature from both sides. The air returned through the top grill is cooled by a chilled water coil (Neslab HX-300, whose water temperature $\sim 8 \text{ }^\circ\text{C}$) and then reheated by fast vendor-made electrical heaters to a controlled temperature. After mixing with the bottom return air, the reheated air is forced by a fan through an acoustic silencer to enter the chamber. The total air volume of the chamber, after accounting for the volume occupied by the lithography tool, is $\sim 6 \text{ m}^3$. The high air velocity results in a chamber air change-over time of 10 seconds. The thermal sensors (Deban Air010 thermistors) in each unit for

the feedback thermal control are located in front of the filter planes (see Tool Temp A and B in Fig. 2-2).

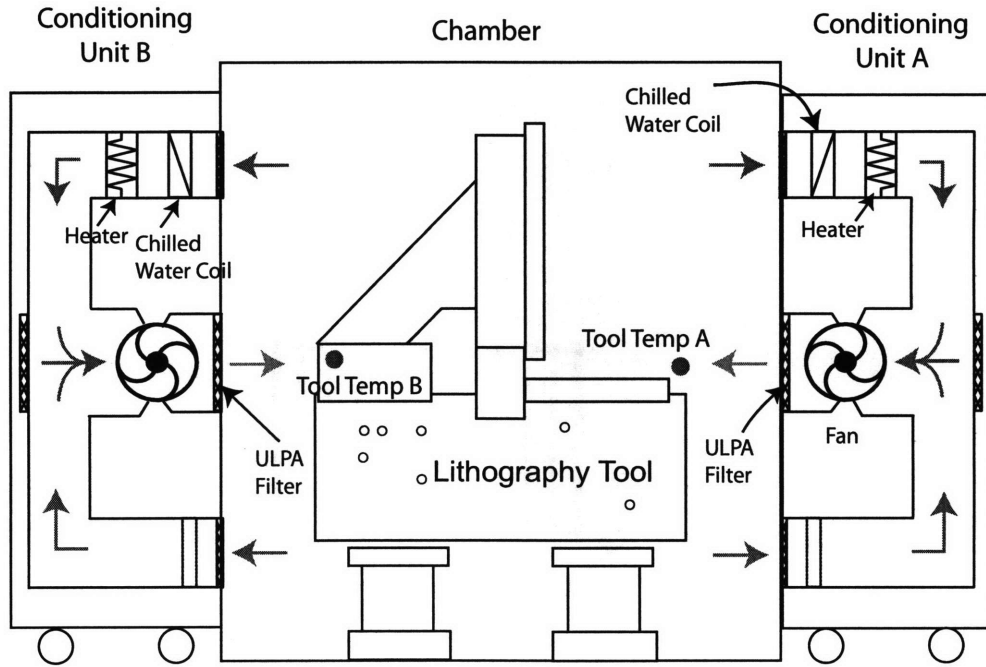


Figure 2-2: Schematic of the enclosure showing air paths and temperature measurement points.

2.3.2 Measuring the transfer function

Measuring a system's open-loop transfer function is a critical step during development of controls to achieve the desired performance. However, sometimes it is impossible to take a direct open-loop transfer function measurement because of noise issues or field-test limitations. Alternatively, we can calculate the transfer function based on closed-loop frequency response measurements. As shown in Fig. 2-3, we used an HP 35670A Dynamic Signal Analyzer to inject a swept-sine stimulus signal, N , into the loop. Frequency response measurements were then taken at points Y1 and Y2. The open-loop transfer function, GTH , of this thermal system is calculated from the

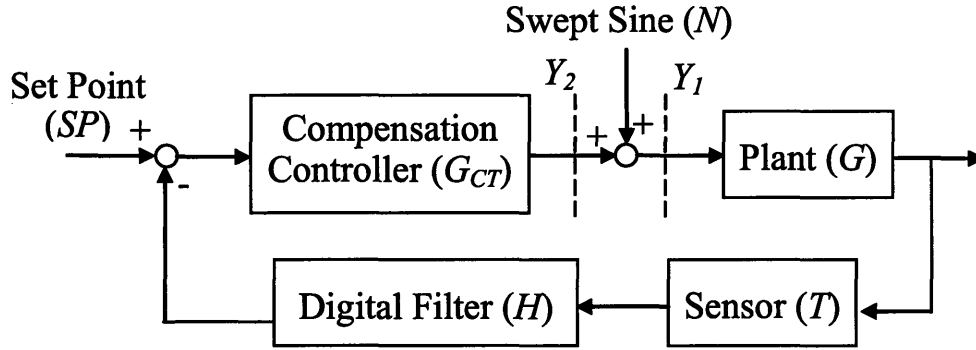


Figure 2-3: Thermal system control diagram including measurement points for determining the closed-loop frequency response.

measurements using equations,

$$\begin{cases} |GTH| = \frac{Y_2}{Y_1} |G_{CT}| \\ \Phi(GTH) = -180^\circ + \Phi\left(\frac{Y_2}{Y_1}\right) - \Phi(G_{CT}) \end{cases} \quad (2.2)$$

where the amplitude of the open-loop transfer function, $|GTH|$, is calculated in the first equation and the phase $\Phi(GTH)$ is given by the second equation.

A temporary PI compensation controller, G_{CT} , with transfer function GTH was utilized in the closed-loop frequency response measurement in order to control the thermal system around the desired temperature set point. Fig 2-4 shows the measured closed-loop frequency response, Y_2/Y_1 . Due to the limited minimum frequency of the 35670A for a swept sine signal, we could only perform frequency response measurements down to 0.015625 Hz. However, this proved to be low enough for us to design the controller. The open-loop transfer function of the thermal system obtained from Equation (2.2) is plotted in Fig. 2-5. The open-loop transfer function is obtained based on the frequency response measurements and there is no explicit formula for it.

From the figure note the 0.025 Hz phase-crossover frequency. This is much slower than the ~ 10 sec air change-over time or the ~ 1 sec electrical heater response time and is dominated by the ~ 1.5 min response time of the system's control thermistors.

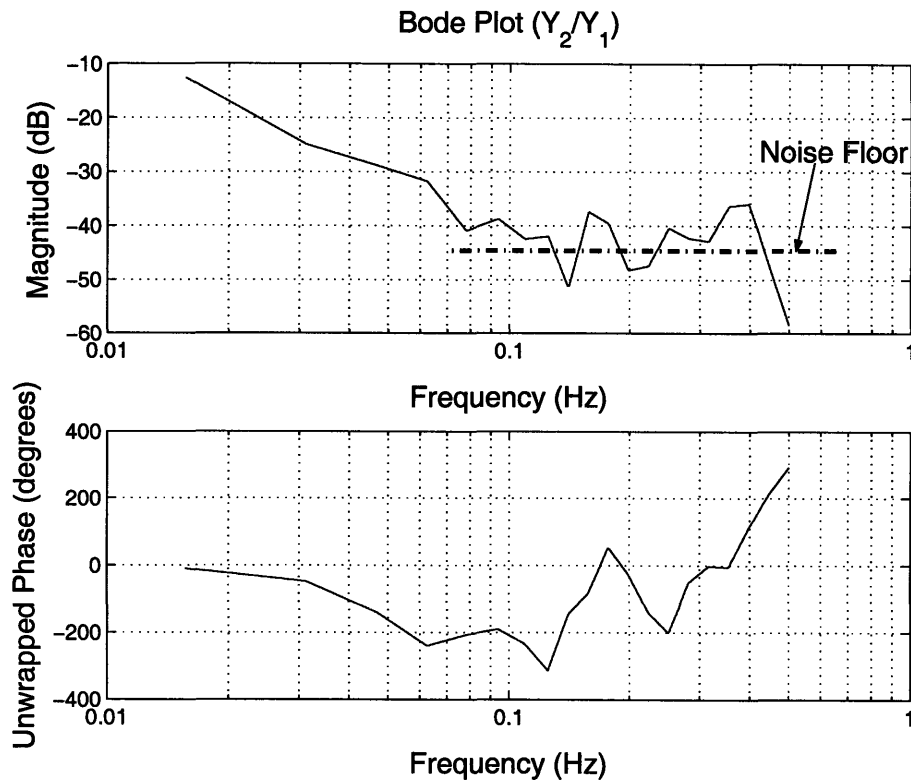


Figure 2-4: Bode plot of measured system closed-loop frequency response, Y_2/Y_1 .

2.3.3 Controller Design

In this subsection a controller will be designed in order to make the system stable in close-loop, speed system transient response, and eliminate steady-state error of the system. The thermal control system is stable in close-loop since the magnitude of the open-loop transfer function, which is about -40 dB, is less than 0 dB at the phase-crossover frequency (see Fig. 2-5).

In order to speed the transient response of the thermal system, a lead compensation controller with transfer function $\frac{100s+1}{15s+1}$ is designed, which reduced overshoot by increasing the phase margin and resulted in a faster transient response by increasing the phase-crossover frequency to 0.035 Hz. Bode plots of the open-loop transfer functions for the lead-compensated system and uncompensated system are shown in Fig. 2-6.

A PI controller with transfer function $1 + \frac{1}{1000} \frac{1}{s}$ was also added into the control

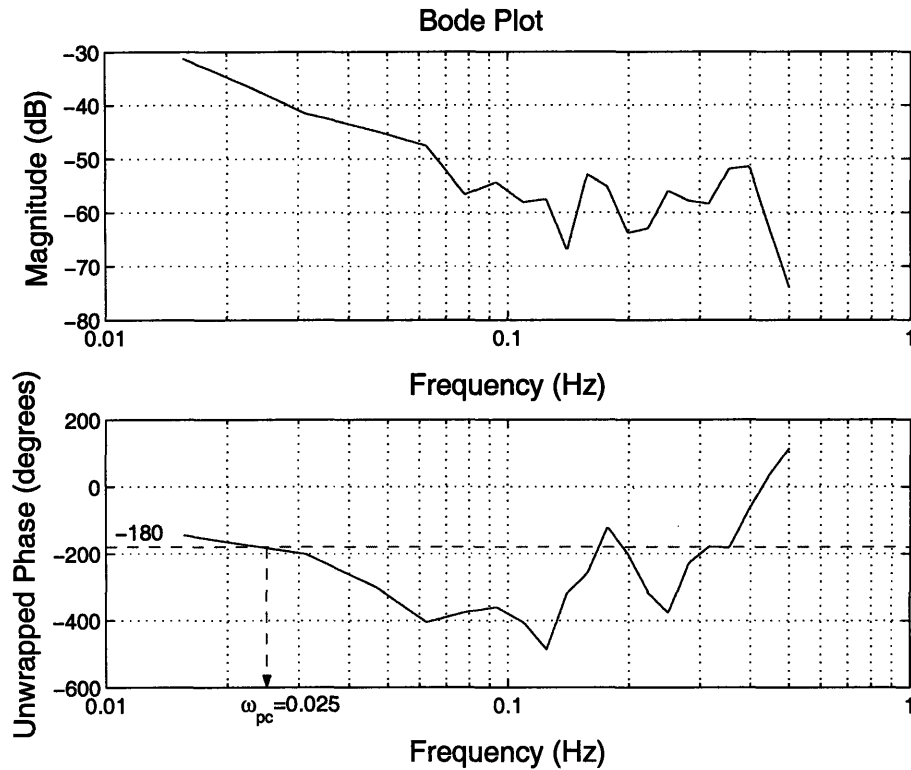


Figure 2-5: Bode plot of measured system open-loop transfer function for the thermal system, where ω_{pc} is the phase-crossover frequency.

system in order to eliminate the steady-state error. Fig. 2-7 shows a measured steady-state error of around $0.2\text{ }^{\circ}\text{C}$ with respect to the set point ($20\text{ }^{\circ}\text{C}$) when there is no PI controller.

Fig. 2-8 shows a diagram of our complete thermal control system. The s-domain system design (Fig. 2-8a) was converted to a z-domain design (Fig. 2-8b) using a bilinear approximation and implemented in a MicroLogix™ 1200 programmable logic controller, with a cycle speed of 1 Hz. In Fig. 2-8 the digital controller is enclosed by a dashed box. A digital filter, H , is utilized to reduce the measurement noise of the system thermistors by averaging 1-sec of thermistor measurements (approximately 50 ~ 100 data points). The averaging shrinks the measurement noise from $2\text{ }^{\circ}\text{C}$ ~ $3\text{ }^{\circ}\text{C}$ to $0.3\text{ }^{\circ}\text{C}$. We set the gain, K , to 16, which was selected to achieve an optimal transient response to a step input of the set point. An anti-windup block was utilized to avoid the effect of integrator windup [18], which reduces the transient response time

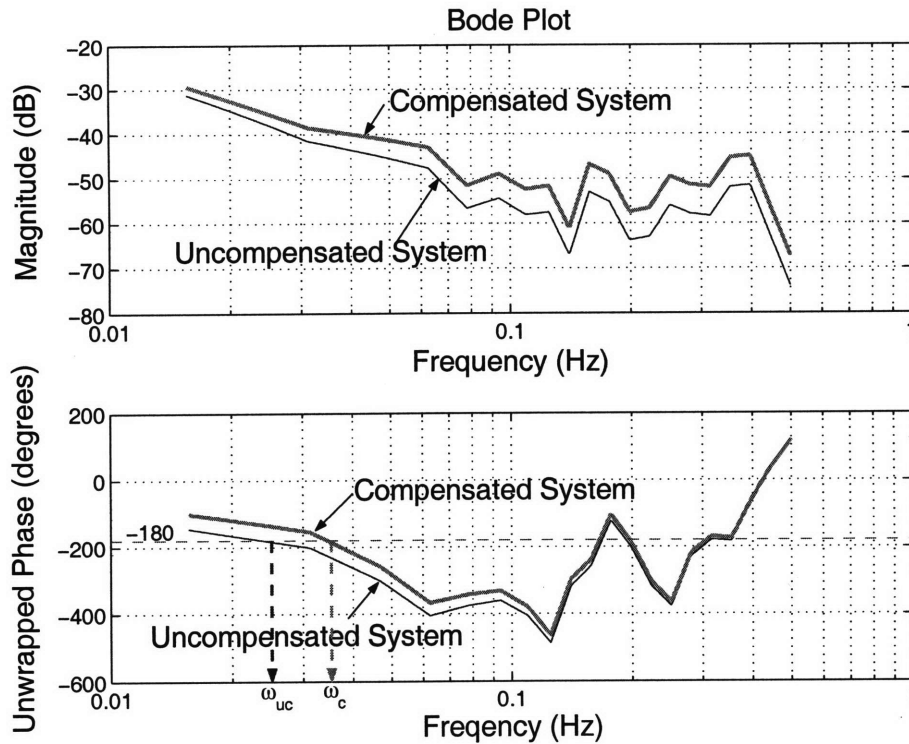


Figure 2-6: Measured Bode plots of the open-loop transfer function for the lead-compensated and uncompensated system. ω_{uc} is the phase-crossover frequency of the uncompensated system and ω_c is the phase-crossover frequency of the compensated system.

and speeds up temperature recovery from large thermal disturbances, for example, after opening the enclosure door. Fig. 2-9 shows the system response to a step input of the set point. The system with the anti-windup block will reach the new set point much more quickly than without the anti-windup block. For example, after setting new desired temperature, the system will reach within 3 minutes ± 0.002 °C of the new set temperature (Fig. 2-9).

2.3.4 Performance of the thermal control system

With the PI-lead compensation controller, a single-point air temperature stability of less than 1 $m^\circ C$, one-sigma, was obtained during a two-hour interval, which is shown in Fig. 2-10. The feedback temperature sensor of the thermal control system measured a one-sigma stability of 0.7 $m^\circ C$ and independent temperature sensor obtained a

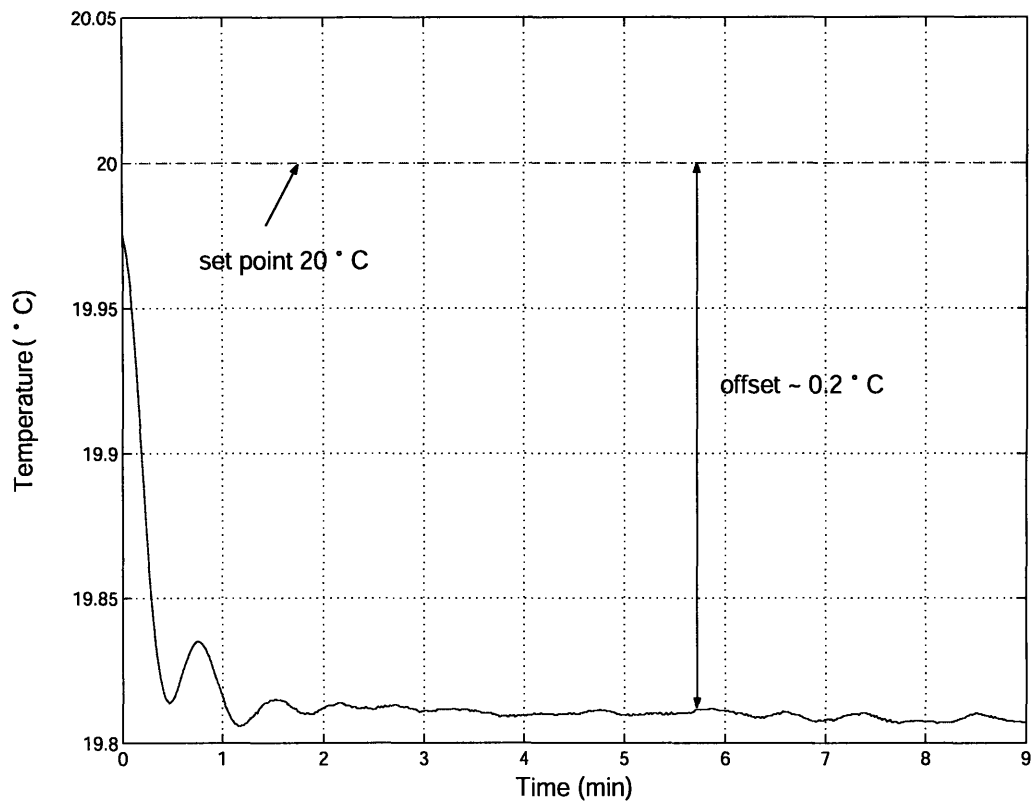


Figure 2-7: Measured performance of the thermal control system (side B) without the PI controller. The thermal controller was turned on at time 0.

one-sigma stability of $0.5\text{ m}^{\circ}\text{C}$. The difference in performance as measured by the system sensor and the independent sensor is due to their different response times (see section 2.4).

The previous thermal control system was designed by the vendor of the environmental enclosure, TAC-Control Solutions Inc (CSI). The structure of the controller is complicated but does not work well. In each unit two cascaded PID controllers were utilized to control electrical heaters. The performance of the thermal system, the system sensor measured a $2.4\text{ m}^{\circ}\text{C}$ one-sigma air temperature stability at a single point over a two hour interval, is not benefit from the complexity of the control system structure. In the current control system, only one well-designed compensation controller is used for each unit but with better performance than the previous one. The performance of the thermal control system before and after the improvements is

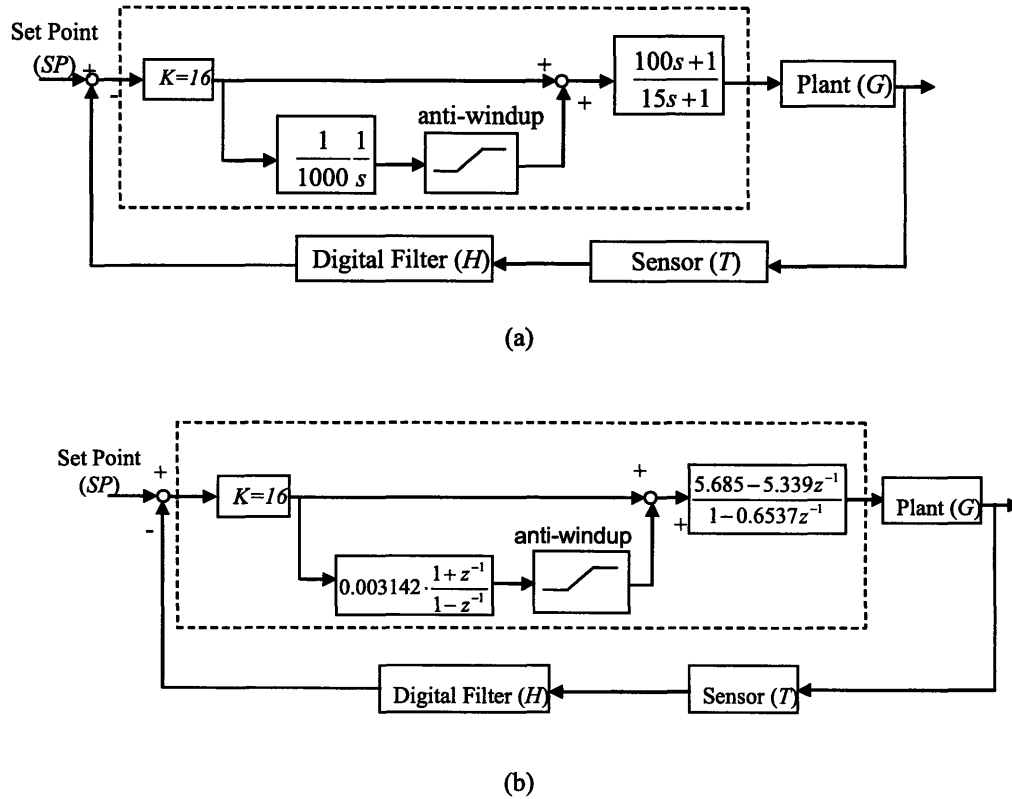


Figure 2-8: Diagram of the complete thermal control system. The portion inside the dashed area represents the digital controller. (a) The controller in s-domain. (b) The controller in z-domain.

shown in Fig. 2-11. All temperature measurements were sampled at 1 Hz.

2.4 Milli-degree temperature gradients mapping

The time-variant temperature gradient over larger volumes is another concern for us since the large time-variant temperature gradients will impair the patterning precision of the Nanoruler. In Section 2.3 stable temperature control at a single point has been achieved. In this section a technique to rapidly map the temperature gradients over an area will be presented. When mapping the temperature gradients over an area, it is required to accurately measure the temperatures at different locations at the same time. A technique to achieve accurate cross-calibration of thermistors will be

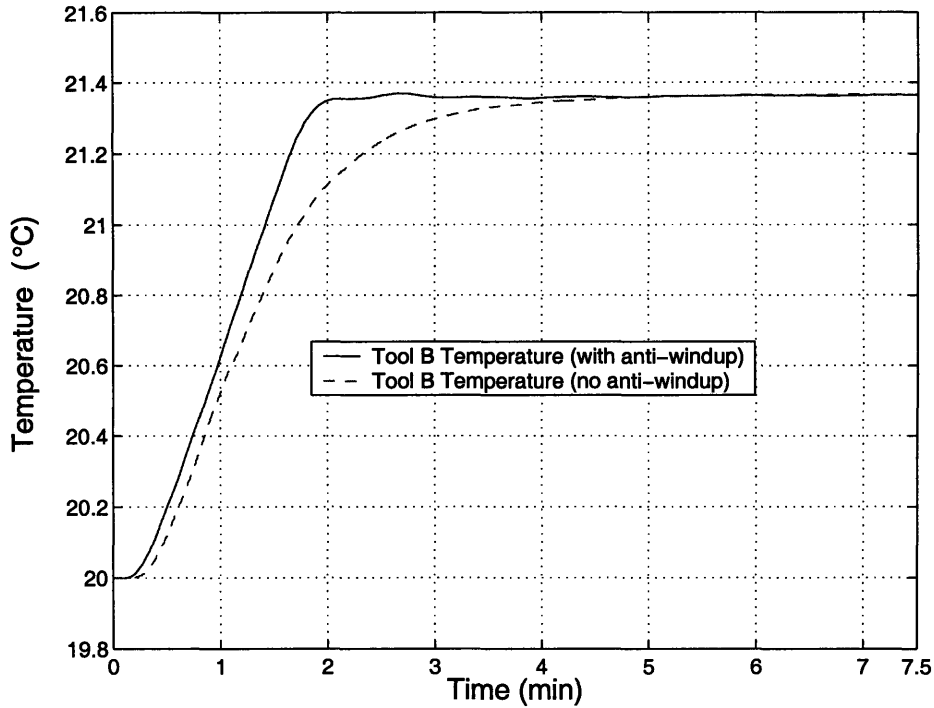


Figure 2-9: Measured thermal system responses to a step input of the set point.

developed.

2.4.1 Thermistor cross calibration and the self-heating effect

This subsection will talk about a technique to achieve accurate cross-calibration of the thermistors in order to accurately measure the temperatures at different locations at the same time when mapping the temperature gradients over an area. After this a discussion on self-heating effect of thermistors will be carried out to make sure this self-heating effect will not cause incorrect temperature measurement. An independent temperature measuring system (Instrulab Model 3312A 12-channel thermometer) was utilized to map temperature gradients and test the performance of the thermal control system. The temperature data acquisition system has a stated accuracy of $10\text{ m}^\circ\text{C}$ and a resolution of $1\text{ m}^\circ\text{C}$. We confirmed the system noise to be less than $1\text{ m}^\circ\text{C}$. The system uses model 052SS sensors which are 4-wire water-proof themistors with

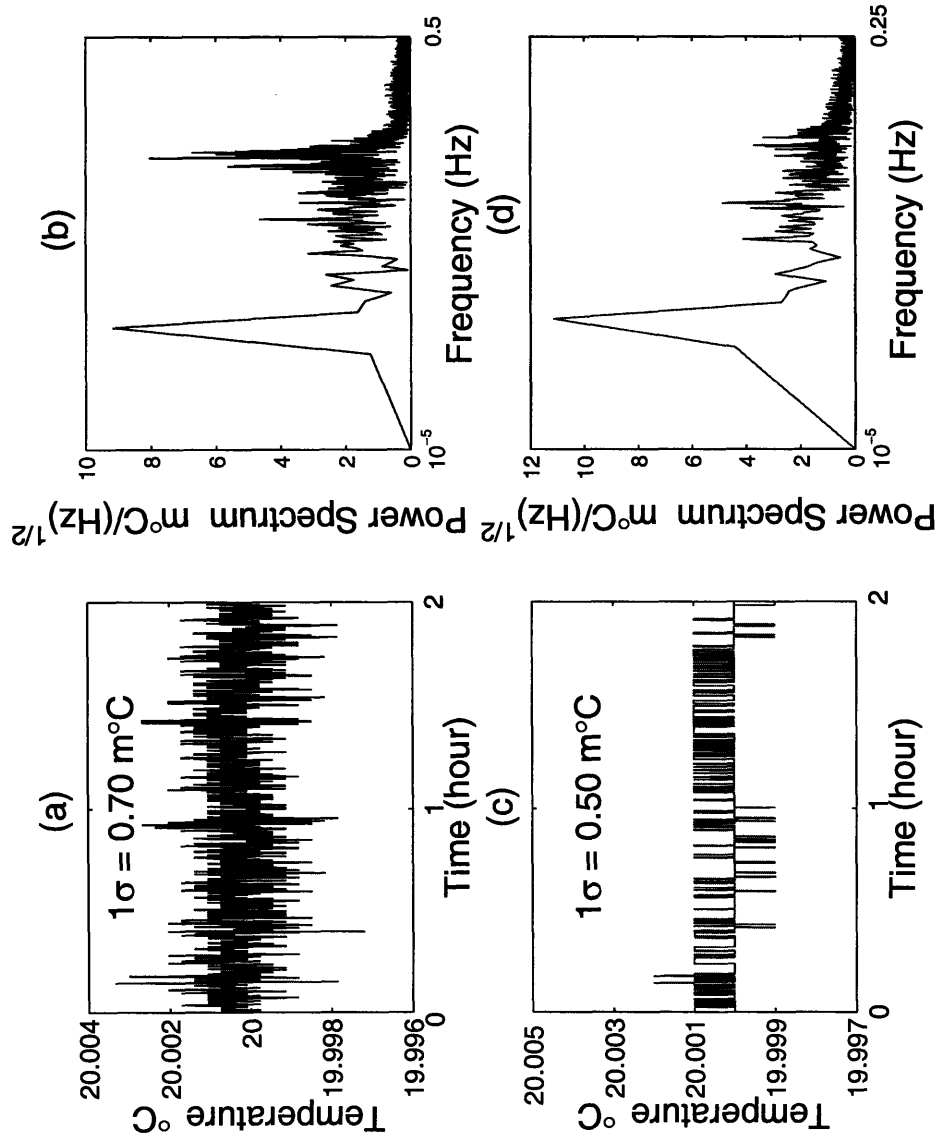
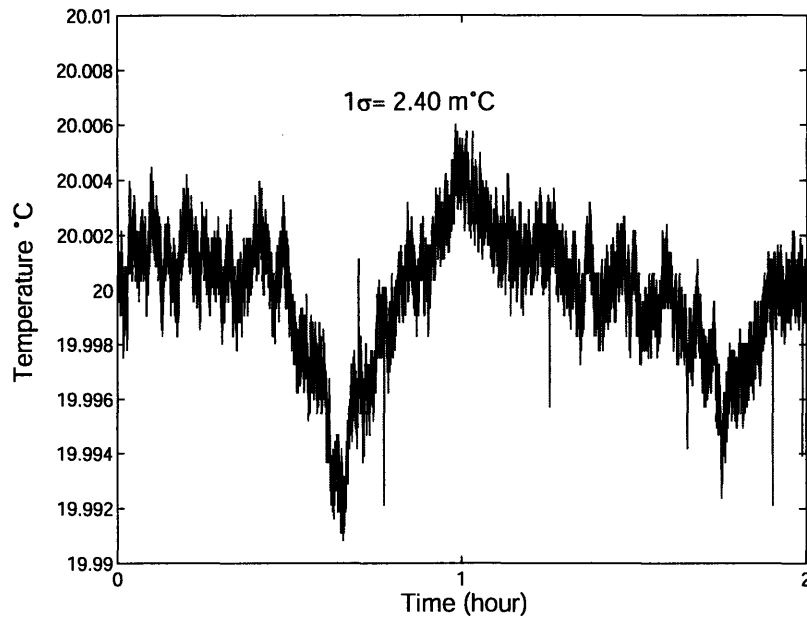
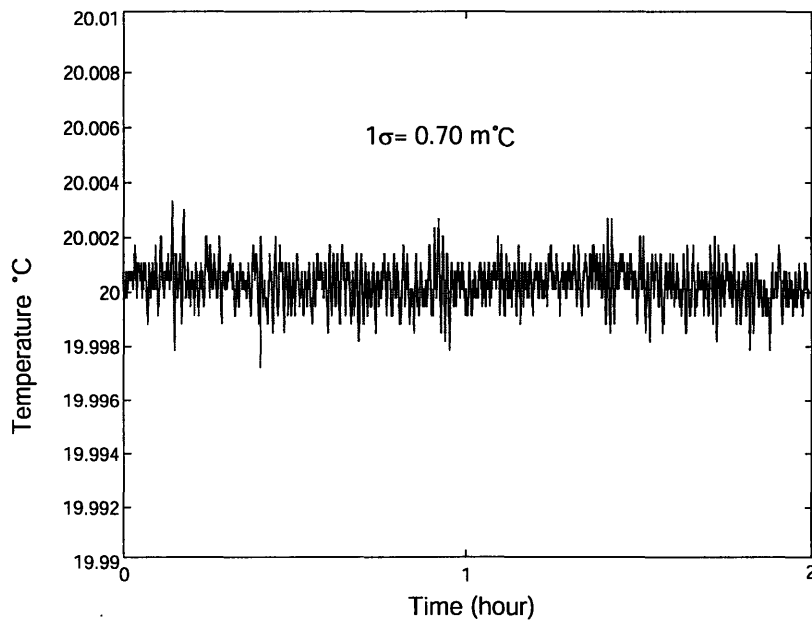


Figure 2-10: Two hours of single-point temperature measurements of the thermal system. (a) Measured side B temperature with the system error. (b) Frequency content of measured side B temperature with the system sensor. (c) Measured side B temperature with an independent sensor. (d) Frequency content of measured side B temperature with the independent sensor.



(a)



(b)

Figure 2-11: Two hours of single-point side B temperature measurements of the thermal system with the system error. (a) Before the improvement of the thermal control. (b) After the improvement of the thermal control.

a 3-minute time constant in air. Data sampling rate is 0.25 Hz.

Accurate cross calibration of the thermistors is important in order to obtain sub-millidegree-relative-accuracy temperature gradient maps. Some water baths can provide a temperature stability of $\pm 25 \mu^\circ C$ over 24 hours [19]. Here a simple calibration water bath shown in Fig. 2-12 was constructed with insulation foam and an electro-magnetic stirring rod and placed inside the environmental enclosure resulting in a temperature gradient of less than $1 m^\circ C$. Temperature measurements of 11 thermistor channels immersed in the calibration bath are shown in Fig. 2-13. The measurement of each thermistor over 9 hours varied within $1 m^\circ C$. In Table 2.1 the mean of each thermistor's measurement is provided. Based on the difference between the mean of each thermistor's measurement and the average of all the means of 11 thermistors' measurements, the offset for each thermistor is obtained. After offset correction, a $1 m^\circ C$ relative accuracy of 11 thermistor channels has been achieved.

The self-heating effect of thermistors may potentially cause incorrect measurements when thermistors traverse regions of changing wind velocity ($1 \sim 2 m/s$) [20],[21]. The excitation current of the Instrulab 3312A is about $80 \mu A$ which generates a heat pulse of $3.5 \mu J$ in each thermistor during the 0.3-second measurement. Based on a simple heat capacity calculation, the uncertainty due to self-heating is $< 70 \mu C$. The fact that the self-heating effect on temperature measurement in winds of $1 \sim 2 m/s$ is less than $1 m^\circ C$ was also verified in an experiment that compared the temperature measurements of an instantaneous turn-on thermistor channel and a reference thermistor channel.

2.4.2 Mapping milli-degree temperature gradients

The time-variant temperature gradient over larger volumes will impair the patterning precision of the Nanoruler. This section will discuss a technique to rapidly map the temperature gradients over an area. Monitoring and mapping temperature gradients over large volumes is usually limited by the number of thermistors and thermistor placement. A simple aluminum-rod frame is constructed for our study. Eight thermistors were attached to one vertical rod in this frame, which can be mechanically

Table 2.1: Cross calibration results of 11 thermistor channels

Thermistor channel	Mean of the measurement($^{\circ}C$)	Average of the means ($^{\circ}C$)	Offset to the average ($m^{\circ}C$)	Average of standard error of the offset ($m^{\circ}C$)
1	20.1070	20.107091	-0.091	0.004
2	20.1070		-0.091	
3	20.1070		-0.091	
4	20.1080		0.909	
5	20.1080		0.909	
6	20.1079		-0.809	
7	20.1060		-1.091	
8	20.1070		-0.091	
9	20.1075		0.409	
10	20.1066		-0.491	
11	20.1060		-1.091	

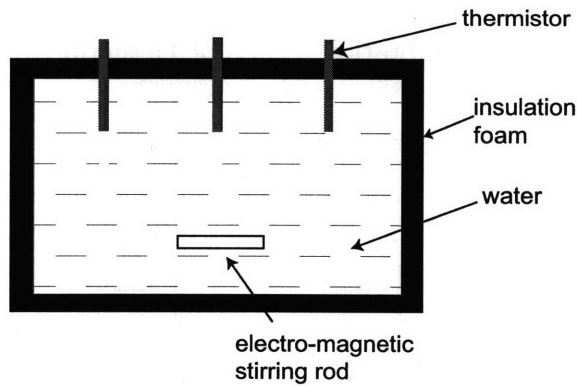


Figure 2-12: Schematic of calibration water bath.

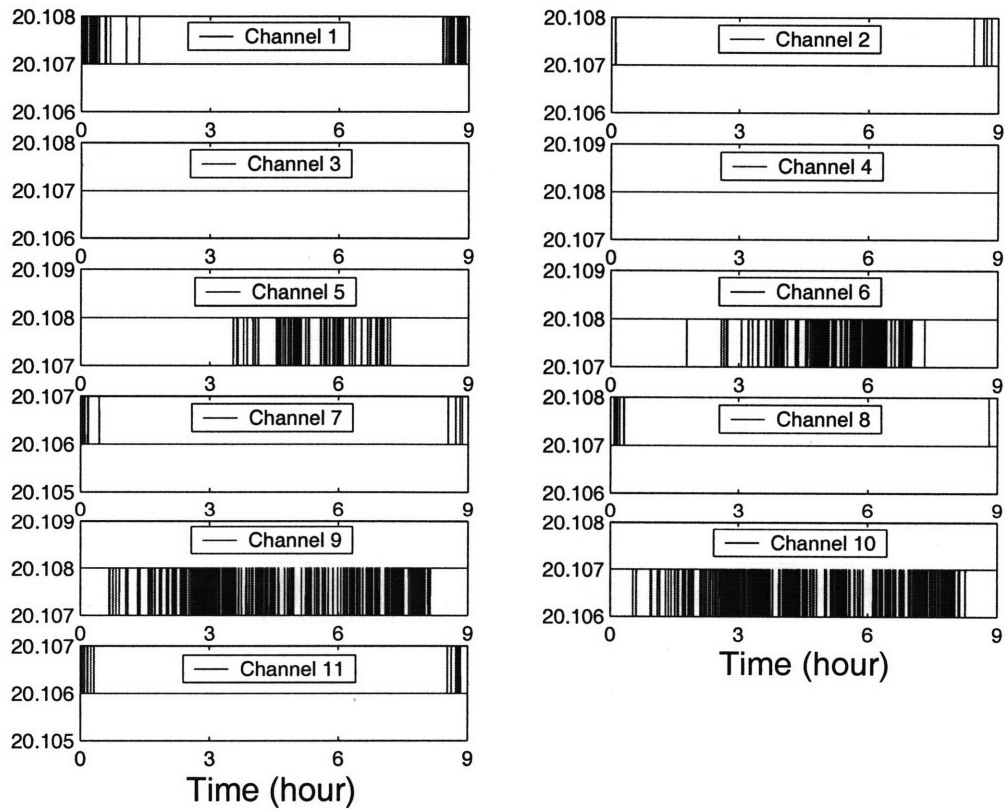
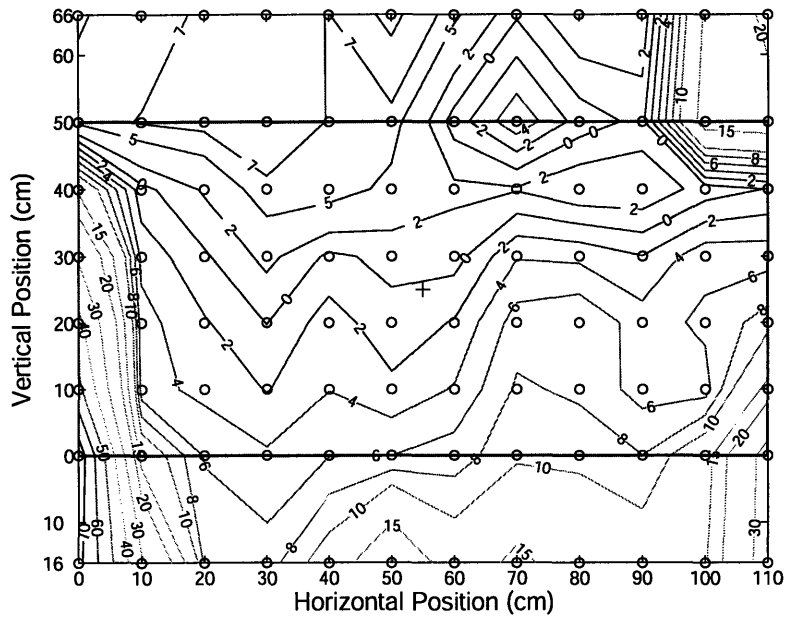
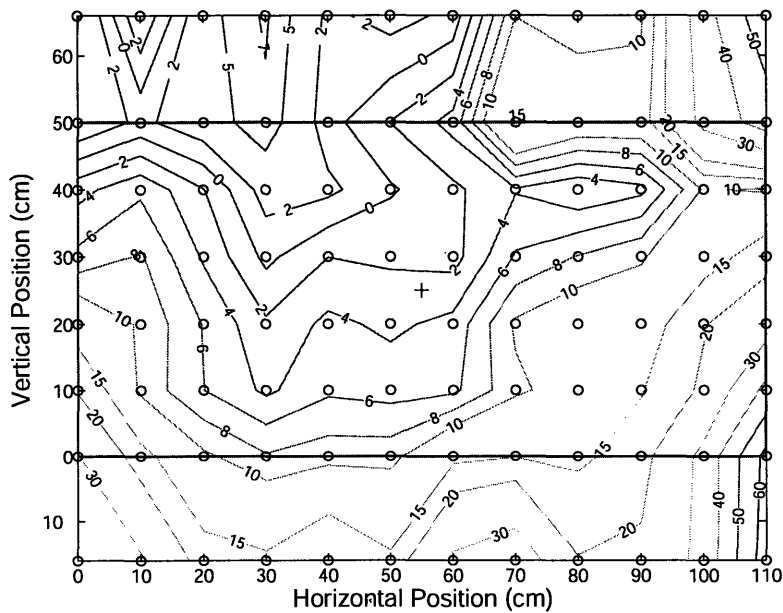


Figure 2-13: Temperature measurements of 11 thermistor channels ($^{\circ}\text{C}$) over 9 hours in the thermal calibration bath.

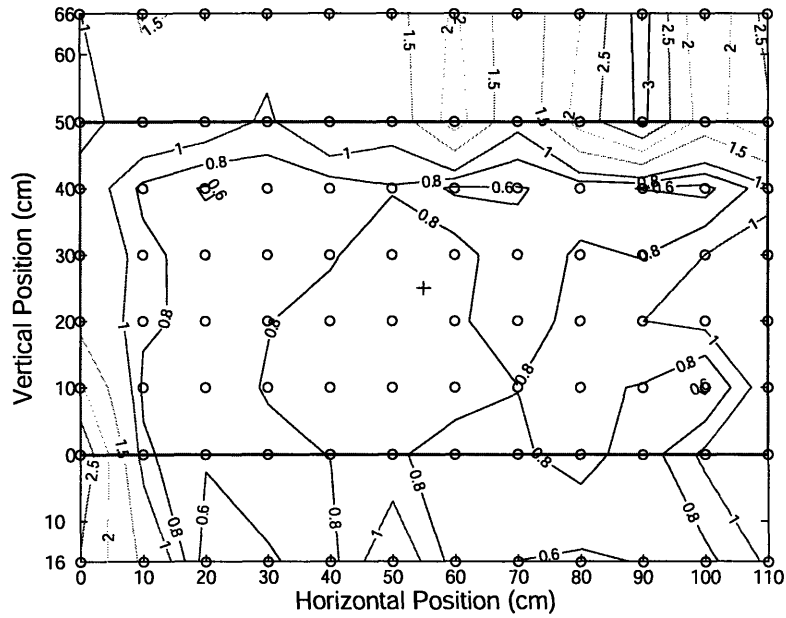


(a)

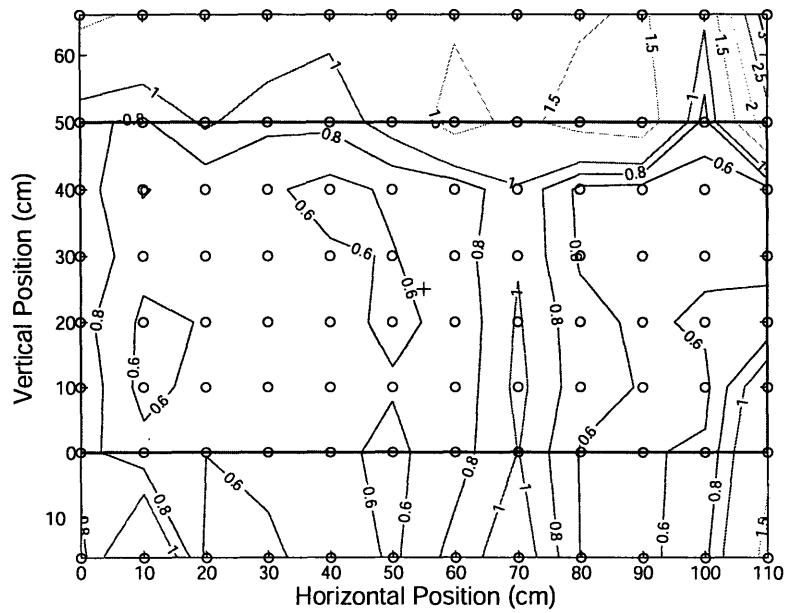


(b)

Figure 2-14: Contour plots of relative temperatures ($m^{\circ}C$) over an an area 30 cm from the filter plane of air handler B. (a) Before the improvement of the single-point thermal control. (b) After the improvement of the single-point thermal control. The central rectangle represents the filter boundary, the circles represent the thermistor measurement positions, and the central cross represents the reference thermistor.



(a)



(b)

Figure 2-15: Standard deviation maps of temperatures ($m^{\circ}C$) over an an area 30 cm from the filter plane of air handler B. (a) Before the improvement of the single-point thermal control. (b) After the improvement of the single-point thermal control. The central rectangle represents the filter boundary, the circles represent the thermistor measurement positions, and the central cross represents the reference thermistor.

moved in a horizontal direction by an external string, and thus used to map temperature gradients within a plane. The mapping plane is shown by a rectangle in Fig. 2-1. A stationary thermistor at the midpoint of the scan was utilized as a reference to eliminate the effect of temperature variations during mapping. During the mapping process, the vertical rod is moved from outside the enclosure, avoiding the large thermal disturbances due to opening and entering the enclosure and significantly reducing the mapping time. The vertical rod was stopped at 12 horizontal locations in sequence. At each location the eight thermistors took 15 minutes of measurements. Only the last 8 minutes of data were utilized to generate maps since there is a several-minute transient time due to rod movement. It takes only 3 hours to map a $110\text{ cm} \times 82\text{ cm}$ area, which is much more rapid than the case of opening the enclosure and relocating the thermistors by hand. At each measurement point, the mean of the relative temperature of this point with respect to the temperature at the center of the filter plane [8], averaged over 8 minutes, is calculated in order to generate a relative temperature map. The standard deviation of this relative temperature is also plotted. Fig. 2-14 shows the relative temperature gradients over a $110\text{ cm} \times 82\text{ cm}$ area which is 30 cm away from the ULPA filter plane of the air handler B, measured before and after the improvement of the thermal control. Fig. 2-14 shows before improving the thermal control, in the main areas of the mapping plane the temperature gradients are less than $8\text{ m}^\circ\text{C}$. After the thermal control improvement, the temperature gradients in the main areas of the mapping plane do not change much. In Fig. 2-14 the corresponding standard deviation maps are shown in Fig. 2-15. In main areas of the mapping plane the relative temperature gradients are within $10\text{ m}^\circ\text{C}$ and their corresponding standard deviation is no more than $1\text{ m}^\circ\text{C}$. The improvement of the single-point thermal control also improved the temperature stability over the mapped area, but did not dramatically change the temperature gradients within the same area.

2.5 Summary

In this chapter, a method to measure the open-loop transfer function of a thermal system has been presented. Based on the measured transfer function, a lead compensation controller together with a PI controller for the thermal control of an environmental enclosure has been designed. Sub-millidegree air temperature stability for a large-volume enclosure has been achieved. Compared with the old thermal controller, the current one is simpler and designed based on the measured open-loop transfer function (The old one was designed by a local company. The engineers only focuses on tuning the PID parameters instead of designing the controller based on the system transfer function). A method to rapidly monitor and map milli-degree temperature gradients over large volumes of enclosed space by mechanically scanning a network of thermistors has been developed and the temperature gradients within the critical tool volumes have been measured. Accurate cross calibration (within $1\text{ m}^\circ\text{C}$) of the thermistors has been performed. Self-heating errors have been shown to be less than $1\text{ m}^\circ\text{C}$. Sub-millidegree relative-accuracy temperature gradients maps have been utilized to test the enclosure thermal system improvements. These improvements reduce two kinds of errors affecting the patterning precision of the Nanuruler, which are the change in the air refractive index and thermal expansion of the substrate chuck.

Further improvement of thermal control could perhaps be achieved by use of control sensors with lower noise and a faster response time. The 0.02 Hz noise peak in the power spectrum (see Fig. 2-10), which lies just at the edge of the system's useful control bandwidth, could probably be reduced further with this improvement. While dramatic improvements in single point temperature stability is achieved, the persistent temperature gradients in the air flow are a concern. Considering only the central $30\text{ cm} \times 90\text{ cm}$ of the filter plane, gradients of up to $25\text{ m}^\circ\text{C}$ were observed (see Fig. 2-14). These hot spots could cause large interferometer errors if this laminar air becomes turbulently mixed downstream and gets into the beam paths, which is likely the case for our lithography tool, especially during stage motion. The origin of the temperature gradients is not known. Further improvements in this area could perhaps

be achieved by use of improved air mixing in the acoustic silencer and ducting with better insulation. Special ducts which direct air to the interferometer beams (also known as air showers) could also potentially reduce turbulent mixing and further reduce interferometer noise.

Chapter 3

Mirror Non-flatness

3.1 Introduction

This chapter will discuss another source of error affecting the precision of the Nanoruler - the measurement error of the non-flatness of the X-axis stage mirror which is one of two reference mirrors in the X-axis stage interferometry system. Section 3.2 will review a technique to measure the X-axis stage mirror non-flatness. However, in this technique there are two kinds of measurement errors - high spatial-frequency noise and location-dependent mirror non-flatness measurement, both which will dramatically reduce the precision of the Nanoruler when utilizing this measurement to correct the non-flatness of the X-axis stage mirror when patterning gratings. In section 3.3 a method will be developed to reduce the high spatial-frequency noise. Section 3.4 will identify the factor causing location-dependent mirror non-flatness measurement and propose a corresponding solution to reduce the location effect on the mirror non-flatness measurement. Section 3.5 will summary the whole chapter.

3.2 Measuring the X-stage mirror non-flatness

Juan Montoya, a previous Ph.D. student in our lab, developed a technique to measure the X-axis stage mirror non-flatness. This section will introduce his technique.

In the Nanoruler, a two-axis (x,y) air bearing stage is utilized to move the sub-

strate in a step-and-scan fashion when exposing the interference fringe patterns in the photoresist. A high-speed digital controller is used to control the stage movement based on the stage position measurements from a Zygo two-axis (x,y) linear/angular column-reference interferometer [22], which will be called the X-Y stage interferometer in the rest of the chapter. The stage position along one axis (e.g., the X axis) is determined by measuring the relative displacement between the X-axis column reference mirror and X-axis stage mirror (shown in Fig. 3-1). Both the X-axis and Y-axis column mirrors are attached to the optical bench, which is stationary. The X-axis and Y-axis stage mirrors are attached to the stage, and they will move together with the stage. The reason why we attach the column mirrors and stage mirrors to two different parts of the Nanoruler is to stabilize the interference fringes, which can be viewed as fixed on the optical bench, with respect to the substrate that is carried by the stage during the exposure. In another words, the scheme to separately attach these two kinds of mirrors helps to reduce the error of mechanical vibrations between the optical bench and the stage during patterning gratings. When patterning gratings via parallel scan, the stage is scanned closely parallel to the Y axis and the stage x position is controlled to be near to a constant (the angle difference between the scan direction and the Y axis is around $20 \mu rad$). Since the X-axis stage mirror is scanning together with the stage, and the X-axis stage interferometer head (shown in Fig. 3-1) is stationary, the non-flatness of the X-axis stage mirror will be imprinted in the gratings, which results in a phase error whose amplitude is proportional to the current-location X-axis stage mirror non-flatness. In the current Nanoruler, the interference fringes are almost parallel to the Y axis (the angle offset is around $20 \mu rad$). Thus the non-flatness of the Y-axis stage mirror will be written into gratings along the direction of grating lines and does not cause any significant error.

The non-flatness of the X-axis stage mirror varies with time, which is verified by taking the same mirror non-flatness measurements on two different dates – Nov. 19th, 2007 and Aug. 24th, 2007 (shown in Fig. 3-2). If we pattern two overlaid layers of grating respectively on Aug. 24th, 2007 and Nov. 19th, 2007 in the spatial frequency doubling, the variation of the X-axis stage mirror non-flatness will result

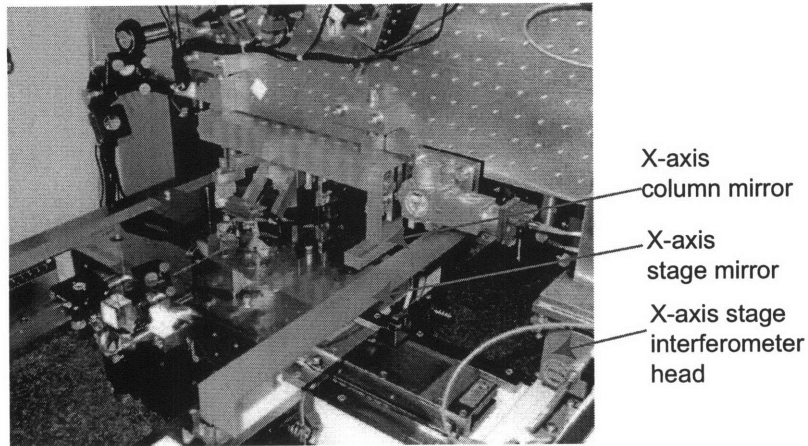


Figure 3-1: The column reference mirror, stage mirror, and interferometer head in the X-axis stage interferometry system.

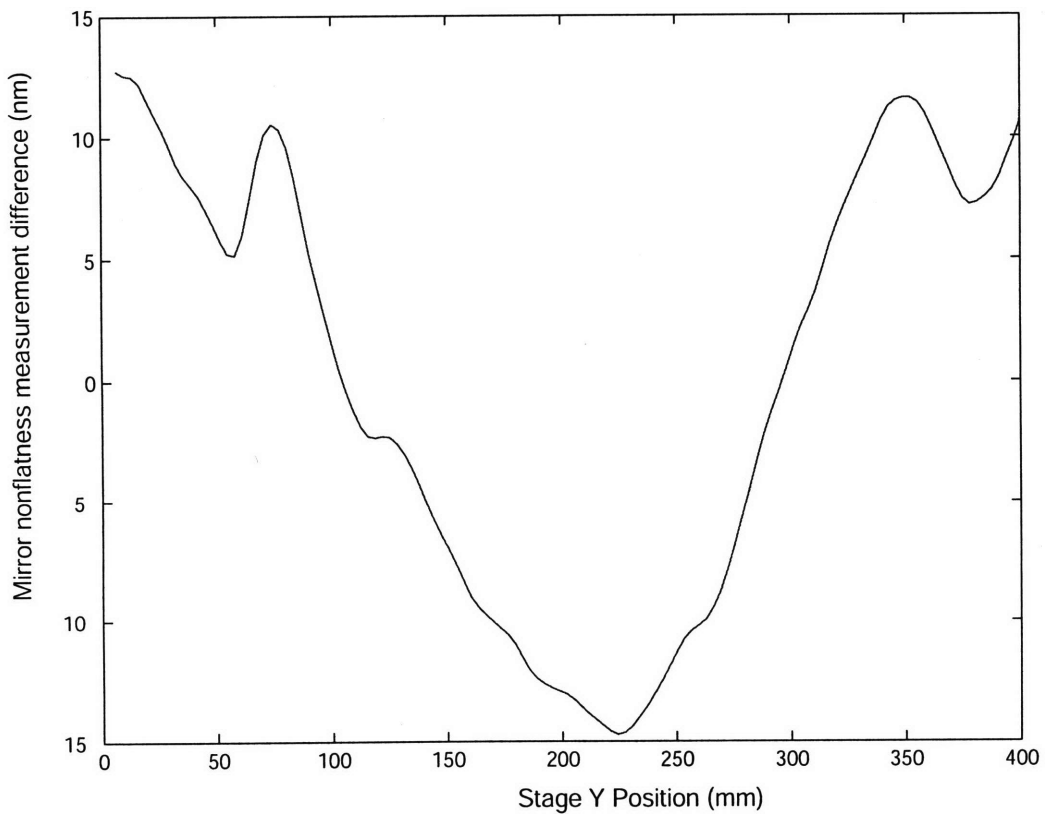


Figure 3-2: The difference of the X-axis stage mirror non-flatness measurements on Nov. 19th 2007 and Aug. 24th 2007.

in serious overlay phase error, which is demonstrated in Fig. 3-3.

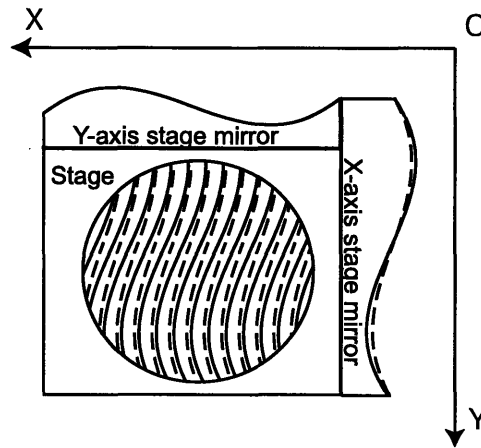


Figure 3-3: Demonstration of the effect of the X-axis stage mirror non-flatness time-dependent variation on pattern overlay.

How can we reduce the effect of the non-flatness of the X-axis stage mirror? One scheme is to perform real-time phase correction based on the non-flatness measurement of the X-axis stage mirror when patterning gratings in the photoresist. One technical challenge is how to measure the profile of the X-axis stage mirror. A self-calibration technique known as the three-flat test has been developed to measure the non-flatness of a mirror [23] [24]. However, for our case - a 400 millimeter mirror bonded onto the stage, there are some limitations for the application of this technique. Juan Montoya, a previous Ph.D. student in our lab, developed an alternative technique to measure the profile of the X-axis stage mirror [25] [26].

3.2.1 Position and angle measurements of the X-Y stage interferometer

Before reviewing Montoya's technique, a brief introduction on the position/angle measurement process of the X-Y stage interferometer system will be given. As shown in Fig. 3-4, the X-Y stage interferometer system includes a laser head with a 3 millimeter beam, an X-axis integrated displacement/angle interferometer (called the X-axis stage interferometer), and a Y-axis integrated displacement/angle interferometer (called the

Y-axis stage interferometer). In the X-axis or Y-axis stage interferometer, a input beam is fed into the interferometer head. After a series of reflections and beam splits, a total eight beams comes out of the interferometer head (Fig. 3-5). The upper four beams hit the reference mirror and the lower four beams hit the stage mirror. Fig 3-6 shows the top view of the X-Y stage interferometer system without the column mirrors. In the rest of the chapter, when illustrating the stage interferometers, the laser head, beam splitter, and fold mirrors are neglected in the graphs.

For the rest of this chapter a coordinate reference frame UV fixed to the stage and a laboratory coordinate frame XY (Fig 3-7) will be defined. The coordinates UV are defined by the X-axis and Y-axis stage mirrors. Its origin-point W is the intersection point of the average surface of the x-axis and y-axis stage mirrors. The V axis is defined to be parallel to the X-axis stage mirror and the U axis is defined to be perpendicular to the V axis. The coordinates XY define the laboratory frame with origin-point O that is defined to be the location of point W when the stage sits at the right top corner of its moving range. The yaw angle between the Y-axis and the V-axis is defined as α . The coordinates of point W in the XY frame is (x_w, y_w) .

As shown in Fig 3-7, an arbitrary point K has coordinates (x_k, y_k) in the XY frame and coordinates (u_k, v_k) in the UV frame. The relationship between (x_k, y_k) and (u_k, v_k) is given by,

$$\begin{cases} x_k = x_w + u_k \cos \alpha + v_k \sin \alpha \\ y_k = y_w - u_k \sin \alpha + v_k \cos \alpha \end{cases} \quad (3.1)$$

Referring to Fig. 3-8, the X-axis position of the stage is measured by the first two beams (Aa and Bb), and all four beams (Aa to Dd) are used to measure the angle of the surface of the X-axis stage mirror with respect to the Y axis. In the XY frame, the X-axis position measurement of the stage (x_{AB}) is given by

$$x_{AB}(x_w, y_w) = \frac{m_A(x_w, y_w) + m_B(x_w, y_w)}{2} \quad (3.2)$$

where the points A and B are the locations where the first two laser beams of the

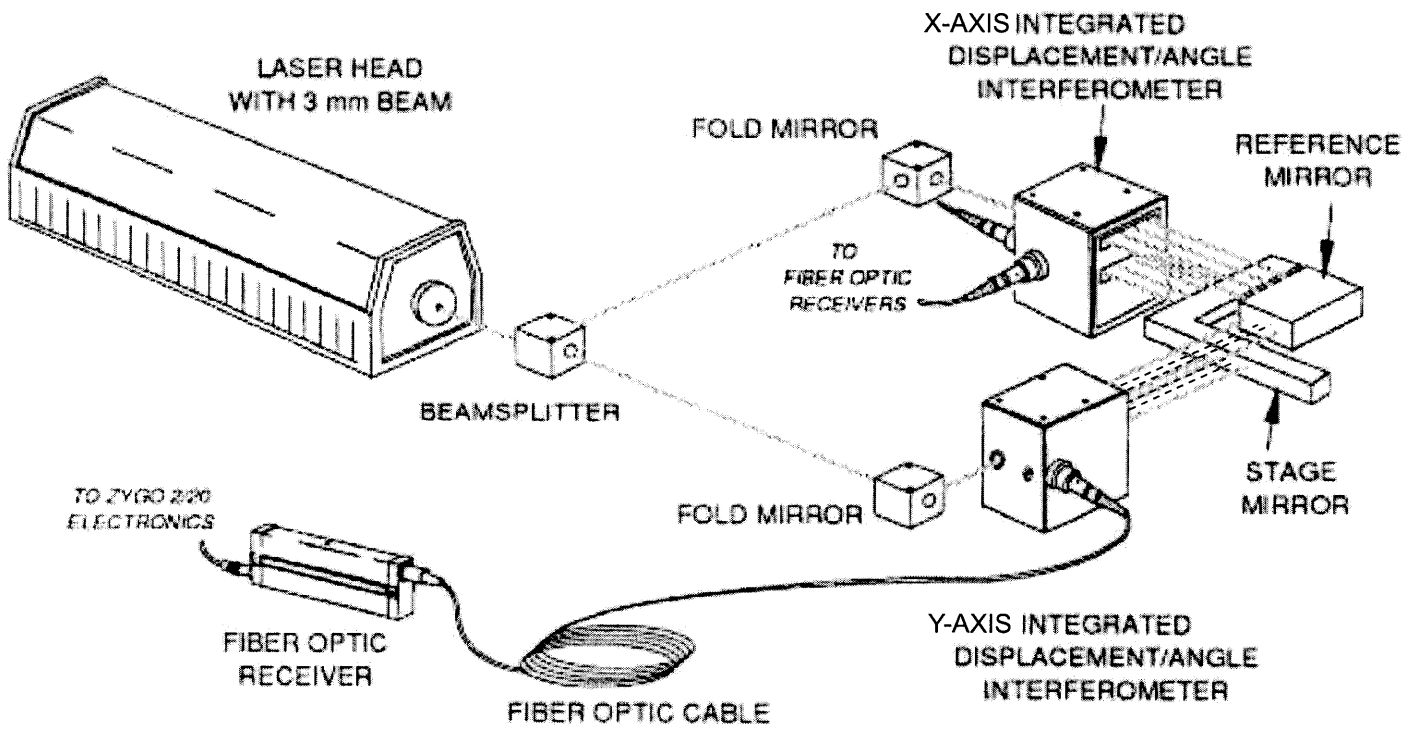
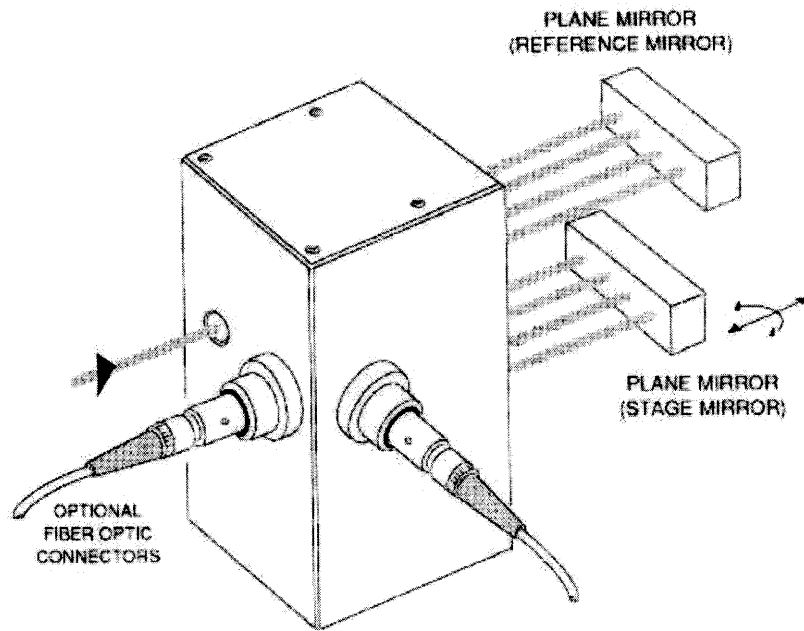
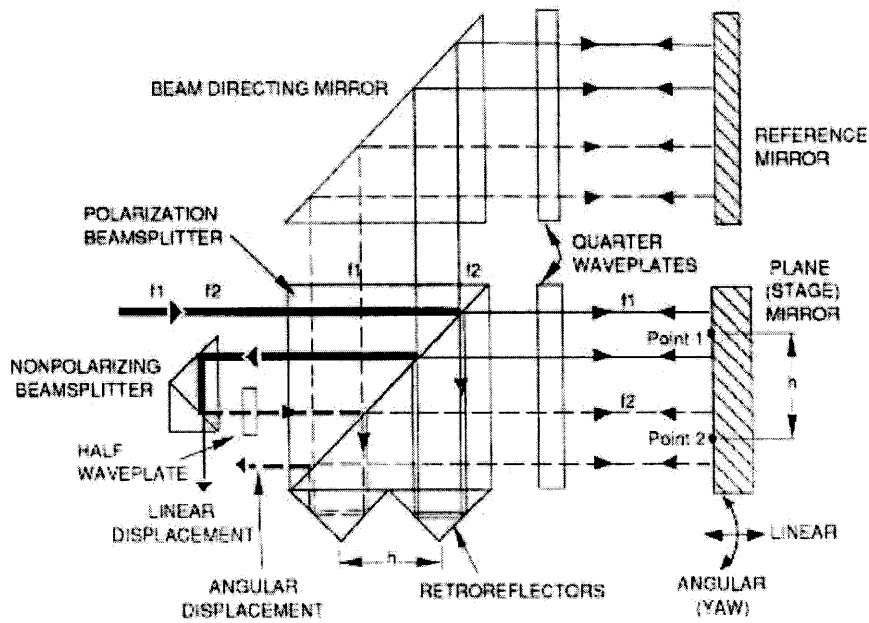


Figure 3-4: The Zygo two-axis linear/angular column-reference interferometer system (the X-Y stage interferometer).



(a) Integrated Displacement/Angle Interferometer



(b) Integrated Displacement/Angle Interferometer Schematic

Figure 3-5: (a) Integrated displacement and angle interferometer head. (b) Schematic of integrated displacement and angle interferometer head.

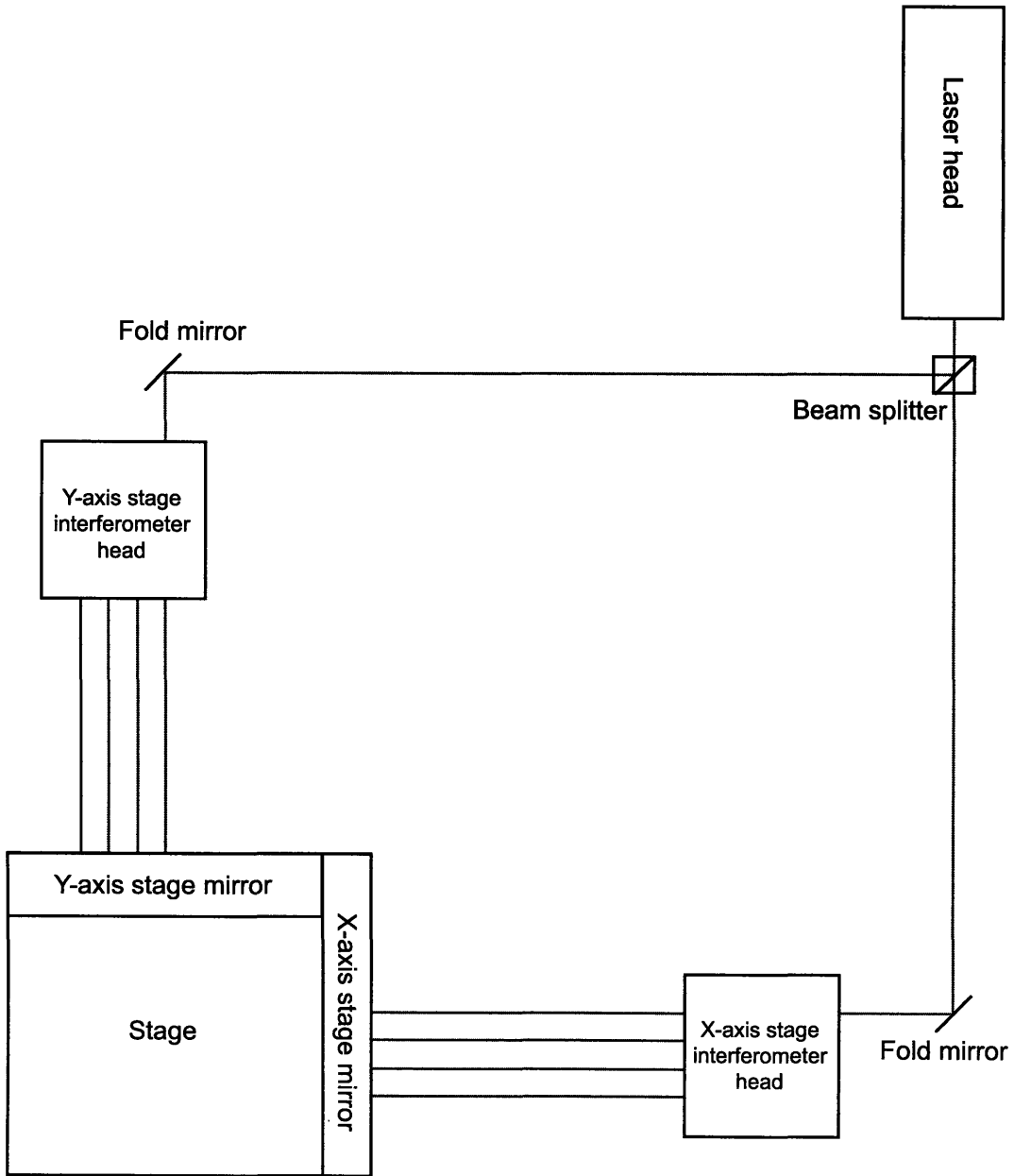


Figure 3-6: Top view of the X-Y stage interferometer system without the column mirrors.

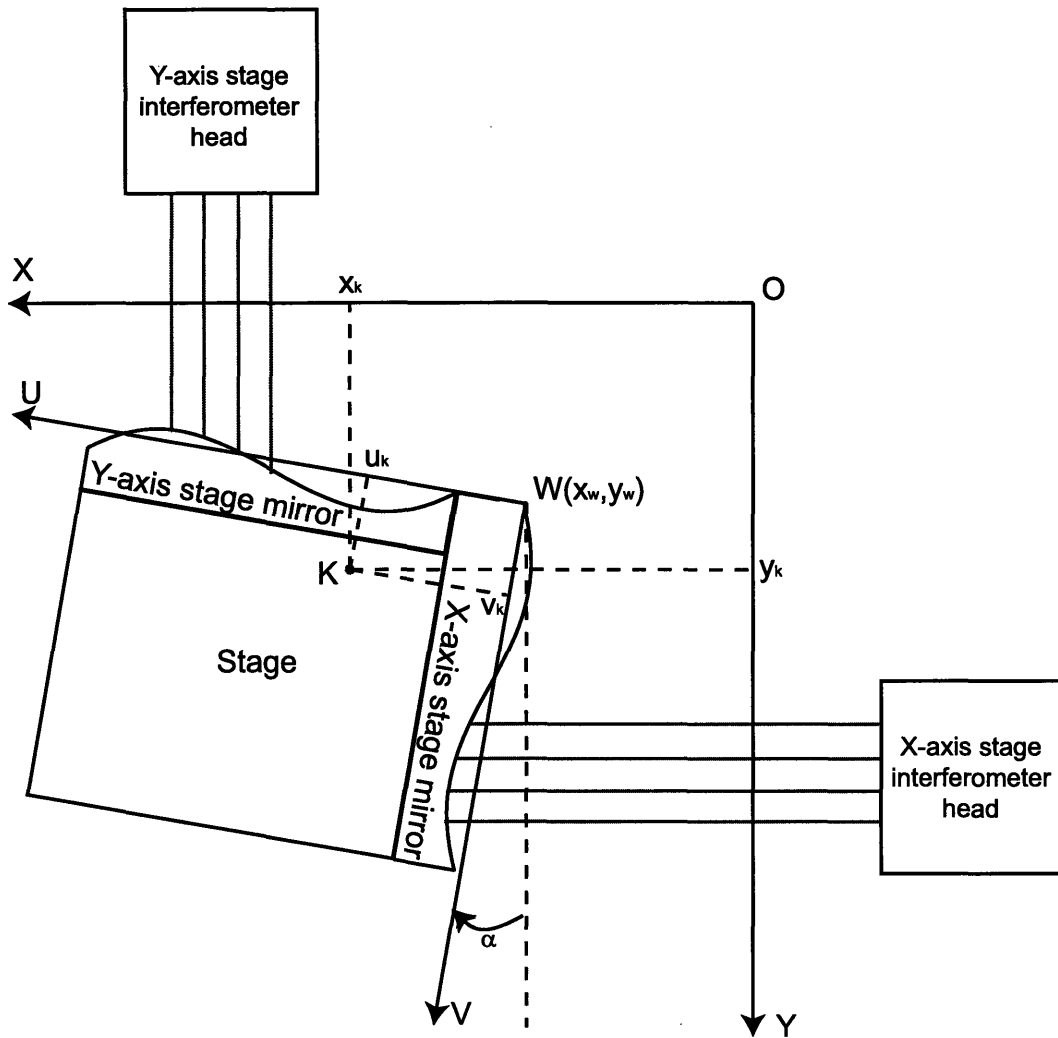


Figure 3-7: Definition of laboratory coordinates XY with origin O and stage coordinates UV with origin W. In the XY frame, the coordinates of point W is (x_w, y_w) . The coordinates of point K in the XY frame is (x_k, y_k) and in the UV frame is (u_k, v_k) .

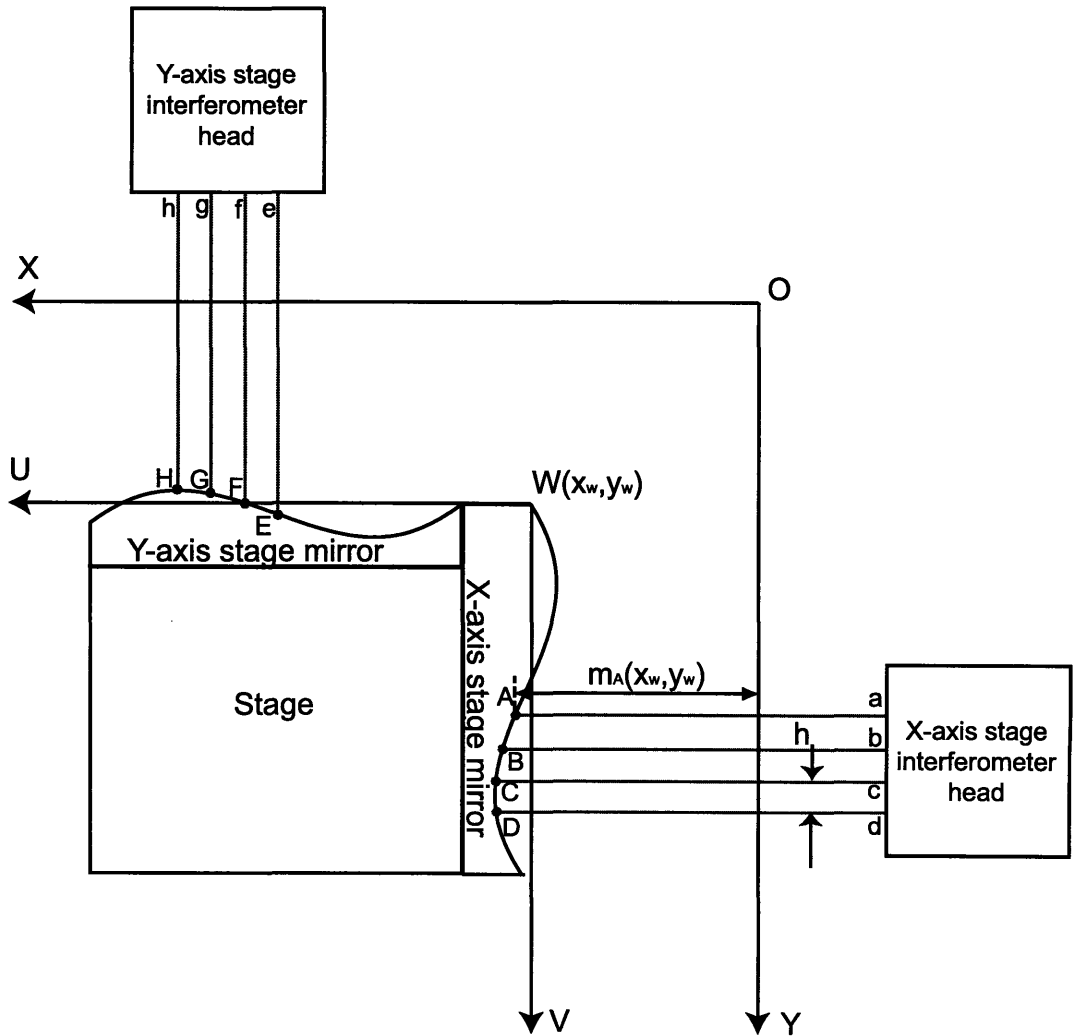


Figure 3-8: The X-axis and Y-axis stage mirrors with the X-Y stage interferometer heads.

X-axis stage interferometer hit the surface of the X-axis stage mirror (Fig. 3-8). As we know, x_{AB} is a function of stage position. Assuming the stage is a rigid body, the stage only translates and rotates on the granite table. Thus the position of any point on the stage together with the stage yaw angle can be used to represent the stage position. Also we assume that the stage yaw rotation only depends on the stage position. Thus we can use the position of any point on the stage to represent the stage position. Here, in order to simplify the deduction, we choose point W, whose coordinates in the XY frame are (x_w, y_w) , to express the stage position. Thus we know, $x_{AB}(x_w, y_w)$ represents the measurement of the stage x position when the stage is located at (x_w, y_w) , and $m_A(x_w, y_w)$ and $m_B(x_w, y_w)$ respectively represent the x positions of point A and B when the stage is at (x_w, y_w) .

What have to be made clear is that point W is a point on the stage while point A (and the same for points B, C, and D) is the point where one beam of the X-axis stage interferometer hits the X-axis stage mirror (in other words, when the stage moves along the Y axis, point W will move together with the stage and point A will be stationary if the X-axis stage mirror is perfectly flat).

With the same reasoning, the third and the fourth beams (Cc and Dd) of the X-axis stage interferometer can also give us another measurement of the X-axis stage position,

$$x_{CD}(x_w, y_w) = \frac{m_C(x_w, y_w) + m_D(x_w, y_w)}{2} \quad (3.3)$$

where the points C and D are the locations where the two laser beams (Cc and Dd) of the X-axis stage interferometer hit the surface of the X-axis stage mirror (Fig. 3-8). Here $m_C(x_w, y_w)$ and $m_D(x_w, y_w)$ respectively represent the x positions of points C and D when the stage is at (x_w, y_w) .

Then the angular measurement $\theta(x_w, y_w)$, i.e., the angle of the surface of the X-axis stage mirror with respect to the Y axis, can be calculated as,

$$\theta_x(x_w, y_w) = \frac{x_{AB}(x_w, y_w) - x_{CD}(x_w, y_w)}{2h} \quad (3.4)$$

where h is the spacing between the adjacent beams of the X stage interferometer. It

is important to understand that θ_x includes contributions from both the stage yaw angle α and the mirror non-flatness.

It have been clarified how the stage interferometer measures the X-axis position/angle of the stage. The same process is also applied in the Y-axis position/angle measurement. Note that for the X-axis measurements, the angle of the Y-axis stage mirror with respect to the X axis ($\theta_y(x_w, y_w)$) has the opposite sign definition of $\theta_x(x_w, y_w)$, which is due to

$$\theta_y(x_w, y_w) = \frac{y_{EF}(x_w, y_w) - y_{GH}(x_w, y_w)}{2h} \quad (3.5)$$

where $y_{EF}(x_w, y_w)$ represents the stage y position measurement given by the first two beams (Ee and Ff) when the stage position is (x_w, y_w) and $y_{GH}(x_w, y_w)$ represents the stage y position measurement given by the last two beams (Gg and Hh) when the stage is at (x_w, y_w) .

3.2.2 The X-axis stage mirror non-flatness

The next two subsections will discuss Montoya's technique to measure the non-flatness of the X-axis stage mirror. This subsection will derive a relation between the angle measurements $\Delta\theta$ and the X-axis stage mirror non-flatness. Recall the definitions of the XY and UV frames in Fig. 3-7. Since the non-flatness of the X-axis stage mirror depends only on the V position of the point in the UV frame, the non-flatness of the X-axis stage mirror at point B is defined as $D_x(v_B)$, where v_B is the V position of point B in the UV frame. Based on the definition of the UV frame, we know $D_x(v_B)$ is equal to the U position of point B in the UV frame.

Now let us consider how the stage rotation affects the angle measurement $\theta_x(x_w, y_w)$. Suppose the stage makes a clockwise rotation about point W (see Fig. 3-9), thus there is an angle $\alpha(x_w, y_w)$ between the V axis and the Y axis. Note $\alpha(x_w, y_w)$ means α depends on the stage location (x_w, y_w) . With Equation (3.1), the non-flatness of the

X-axis stage mirror surface at point B can be expressed as,

$$D_x(v_B) = D_x\left(\frac{y_B - y_w + u_B \sin(\alpha(x_w, y_w))}{\cos(\alpha(x_w, y_w))}\right) \quad (3.6)$$

where y_B and y_w are respectively the Y positions of point B and point W in the XY frame and u_B is the U position of point B in the UV frame. According to Equation (3.1) and the definitions of $m_B(x_w, y_w)$ and $D_x(v_B)$, we have,

$$m_B(x_w, y_w) = x_B = x_w + [y_B - y_w + u_B \sin(\alpha(x_w, y_w))] \cdot \tan(\alpha(x_w, y_w)) + D_x(v_B) \cdot \cos(\alpha(x_w, y_w)) \quad (3.7)$$

Since point A, B, C, and D are the locations where the four beams of the X-axis stage interferometer hit the X-axis stage mirror and the spacing between the adjacent beams is h , we have

$$\begin{cases} y_B = y_A + h \\ y_C = y_A + 2h \\ y_D = y_A + 3h \end{cases} \quad (3.8)$$

Therefore with Equation (3.6), (3.7), and (3.8), we can obtain,

$$\begin{cases} m_A(x_w, y_w) = x_w + (y_A - y_w + u_A \sin \alpha) \cdot \tan \alpha + D_x\left(\frac{y_A - y_w + u_A \sin \alpha}{\cos \alpha}\right) \cdot \cos \alpha \\ m_B(x_w, y_w) = x_w + (h + y_A - y_w + u_B \sin \alpha) \cdot \tan \alpha + D_x\left(\frac{h + y_A - y_w + u_B \sin \alpha}{\cos \alpha}\right) \cdot \cos \alpha \\ m_C(x_w, y_w) = x_w + (2h + y_A - y_w + u_C \sin \alpha) \cdot \tan \alpha + D_x\left(\frac{2h + y_A - y_w + u_C \sin \alpha}{\cos \alpha}\right) \cdot \cos \alpha \\ m_D(x_w, y_w) = x_w + (3h + y_A - y_w + u_D \sin \alpha) \cdot \tan \alpha + D_x\left(\frac{3h + y_A - y_w + u_D \sin \alpha}{\cos \alpha}\right) \cdot \cos \alpha \end{cases} \quad (3.9)$$

where $\alpha(x_w, y_w)$ is abbreviated as α . Since the amplitude of the actual stage rotation α is about $10 \mu rad$, we can approximate $\tan \alpha$ as α , $\cos \alpha$ as 1, and $\sin \alpha \cdot \tan \alpha$ as 0. Also $u_A \sin \alpha$, $u_B \sin \alpha$, $u_C \sin \alpha$, and $u_D \sin \alpha$ can be all approximated to zero since they are much less than $h = 6.4 \text{ mm}$. Based on the above approximations,

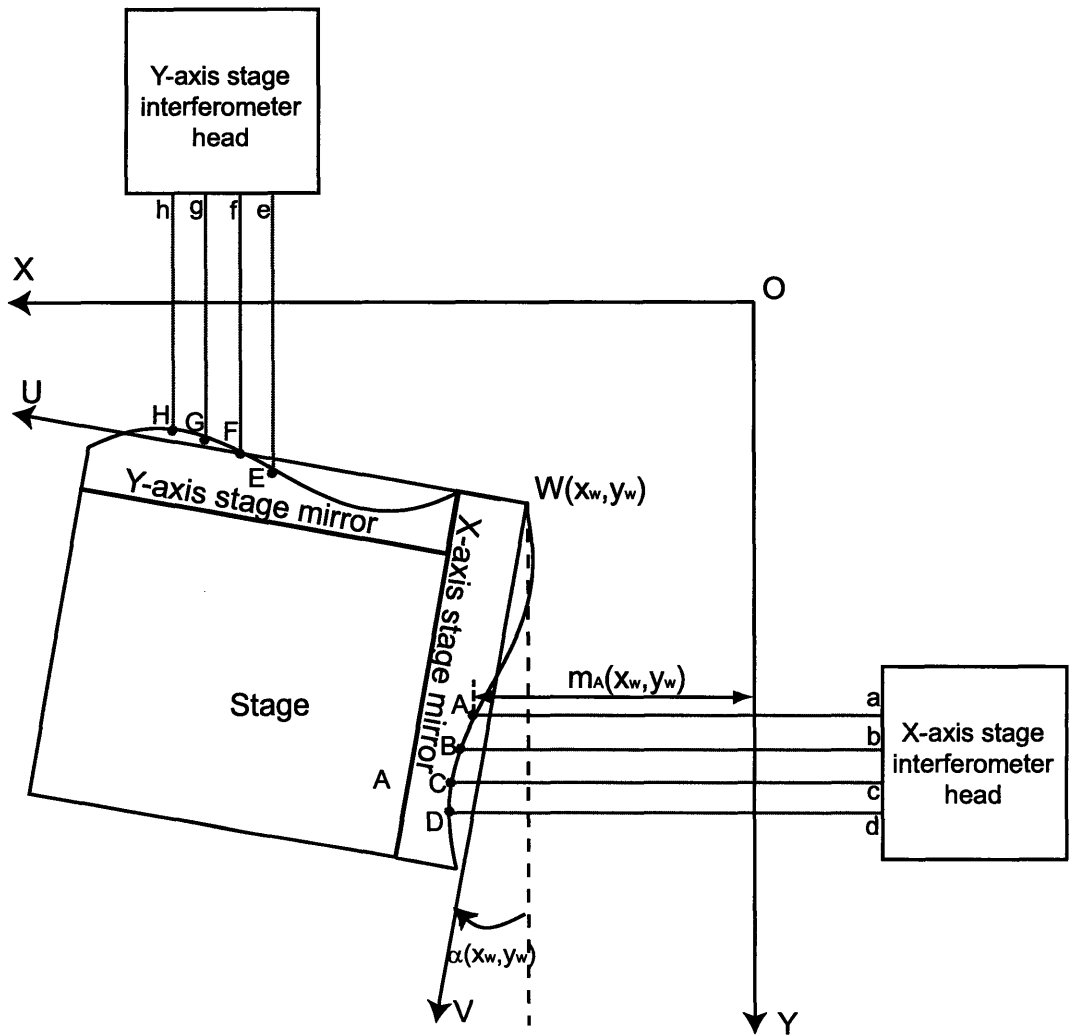


Figure 3-9: The X-axis and Y-axis stage mirrors with the X-Y stage interferometer when there is rotation about point O'.

Equation (3.9) can be rewritten as,

$$\begin{cases} m_A(x_w, y_w) = x_w + (y_A - y_w) \cdot \alpha + D_x(y_A - y_w) \\ m_B(x_w, y_w) = x_w + (h + y_A - y_w) \cdot \alpha + D_x(h + y_A - y_w) \\ m_C(x_w, y_w) = x_w + (2h + y_A - y_w) \cdot \alpha + D_x(2h + y_A - y_w) \\ m_D(x_w, y_w) = x_w + (3h + y_A - y_w) \cdot \alpha + D_x(3h + y_A - y_w) \end{cases} \quad (3.10)$$

Substituting Equation (3.2), (3.3), and (3.10) into Equation (3.4), we can obtain,

$$\theta_x(x_w, y_w) = \frac{D_x(y_A - y_w) + D_x(h + y_A - y_w) - D_x(2h + y_A - y_w) - D_x(3h + y_A - y_w)}{4h} - \alpha(x_w, y_w) \quad (3.11)$$

Following the previous definitions and procedure, we also obtain

$$\theta_y(x_w, y_w) = \frac{D_y(x_E - x_w) + D_y(h + x_E - x_w) - D_y(2h + x_E - x_w) - D_y(3h + x_E - x_w)}{4h} + \alpha(x_w, y_w) \quad (3.12)$$

where $\theta_y(x_w, y_w)$ is the angle measurement of the Y-axis stage interferometer, $\alpha(x_w, y_w)$ is the same stage rotation angle as that in Equation (3.11), and $D_y(x_E - x_w)$ is the non-flatness of the Y-axis stage mirror at point E. As we know, point E is the location where the first left beam of the Y-axis interferometer hits the Y-axis stage mirror. $D_y(x_F - x_w)$, $D_y(x_G - x_w)$, and $D_y(x_H - x_w)$ follow the same definition.

Equation (3.11) gives us a relationship between the X-axis angle measurement $\theta_x(x_w, y_w)$ and the non-flatness of the X-axis stage mirror at point A, B, C, and D (i.e., $D_x(y_A - y_w)$, $D_x(h + y_A - y_w)$, $D_x(2h + y_A - y_w)$, and $D_x(3h + y_A - y_w)$). However, $\alpha(x_w, y_w)$ is unknown. Fortunately, with the help of Equation (3.12), we can bypass the unknown $\alpha(x_w, y_w)$. Consider the situation where we scan the stage along the Y axis and take measurements of $\theta_x(x_w, y_w)$ and $\theta_y(x_w, y_w)$ at the same time. Since x_w is kept constant, in Equation (3.12) the term of $D_y(x_E - x_w) + D_y(h + x_E - x_w) - D_y(2h + x_E - x_w) - D_y(3h + x_E - x_w)$ will not change. Equation (3.12) can be rewritten as

$$\theta_y(x_w, y_w) = \text{const} + \alpha(x_w, y_w). \quad (3.13)$$

Adding Equation (3.13) to Equation (3.11), we have

$$\Delta\theta(x_w, y_w) = \frac{D_x(y_A - y_w) + D_x(h + y_A - y_w) - D_x(2h + y_A - y_w) - D_x(3h + y_A - y_w)}{4h} + const \quad (3.14)$$

where $\Delta\theta(x_w, y_w) = \theta_x(x_w, y_w) + \theta_y(x_w, y_w)$.

Now I define a new function $D(y_w) = D_x(y_A - y_w)$, where $D(y_w)$ is the non-flatness of the X-axis stage mirror at point A when the stage is located at (x_w, y_w) . Note y_A is constant because y_A is determined by the location of the X-axis stage interferometer head which is fixed on the granite table. With the definition of $D(y_w)$ and Equation (3.14), we have,

$$\Delta\theta(y_w) = \frac{D(y_w) + D(y_w - h) - D(y_w - 2h) - D(y_w - 3h)}{4h} + const \quad (3.15)$$

where $\Delta\theta(y_w)$ results from $\Delta\theta(x_w, y_w)$ by ignoring the x position of the stage (x_w) since x_w does not change when scanning the stage along the Y axis.

3.2.3 Discrete measurement transfer function and mirror non-flatness results

This subsection will talk about Juan's method, the inverse transfer function method, which recovers the X-stage mirror non-flatness based on the angle measurements $\Delta\theta$. Now let us discretize Equation (3.15). We scan the stage from $y_w = 0$ at $t = 0$ along +Y direction, and choose the spatial sampling period $\Lambda_s = h/2 = 3.2$ mm and the temporal sampling period $T_s = \Lambda_s / \text{velocity}$, where h (6.4 mm) is the spacing between the adjacent beams of the X-axis stage interferometer and *velocity* (32 mm/s) is the scanning velocity of the stage. According to this sampling scheme, we have the stage Y position $y_w(nT_s) = n\Lambda_s$ at time nT_s . We define $\Delta\theta_n = \Delta\theta(y_w(nT_s))$ and $D_n = D(y_w(nT_s))$. Based on the definitions of D_n and the relationship $h = 2\Lambda_s$, we know

$$\begin{cases} D(y_w(nT_s) - h) = D_{n-2} \\ D(y_w(nT_s) - 2h) = D_{n-4} \\ D(y_w(nT_s) - 3h) = D_{n-6} \end{cases} \quad (3.16)$$

With the definitions of $\Delta\theta_n$ and D_n and Equation (3.16), the discrete form of Equation (3.15) is,

$$\Delta\theta_n = \frac{D_n + D_{n-2} - D_{n-4} - D_{n-6}}{4h} + \text{const} \quad (3.17)$$

Subtracting the constant term from $\Delta\theta_n$, we have

$$\Delta\theta_n^{\text{new}} = \frac{D_n + D_{n-2} - D_{n-4} - D_{n-6}}{4h} \quad (3.18)$$

where $\Delta\theta_n^{\text{new}} = \Delta\theta_n - \text{const}$ and the constant term can be calculated with $\text{const} = \frac{1}{n} \cdot (\sum_{i=1}^n \Delta\theta_i - \frac{(D_n + D_{n-1} + D_{n-2} + D_{n-3}) - (D_{-2} + D_{-3} + D_{-4} + D_{-5})}{4h}) \approx \text{mean}(\Delta\theta_n)$ when n is large enough.

After we obtain Equation (3.18), the key problem of measuring the non-flatness of the X-axis stage mirror has been transferred to how to obtain D_n based on the measurement of $\Delta\theta_n^{\text{new}}$. Montoya proposed a method called the inverse transfer function method to solve this problem, which can be summarized as the following. First we take the Z transform of Equation (3.18), yielding the discrete transfer function $H(z)$ from D_n to $\Delta\theta_n^{\text{new}}$,

$$H(z) = \frac{1}{4h}(1 + z^{-2} - z^{-4} - z^{-6}) \quad (3.19)$$

Fig. 3-10 shows $H(z)$ has two sets of double zeroes located in the imaginary axis of the z plane and two single zeroes located in the real axis of the z plane. Since all zeroes of $H(z)$ are on the unit circle of the z plane, it is impossible to obtain a stable inverse transfer function of $H(z)$. Montoya made an approximation for $H(z)$ to get $H_a(z)$, whose zeroes and poles are shown in Fig 3-11. Definitely the inverse of $H_a(z)$, $H_a^{-1}(z)$, is stable,

$$H_a^{-1}(z) = G \frac{4h}{a_0 + a_1 z^{-1} + a_2 z^{-2} + a_3 z^{-3} + a_4 z^{-4} + a_5 z^{-5} + a_6 z^{-6}} \quad (3.20)$$

where $a_0 = 1$, $a_1 = 0$, $a_2 = 0.4649$, $a_3 = 0$, $a_4 = -0.8942$, $a_5 = 0$, $a_6 = 0.5116$, and the gain $G = 0.7367$.

The X-axis stage mirror non-flatness $D(y_w)$ (Fig 3-12) can be obtained by applying the inverse filter $H_a^{-1}(z)$ to the discrete measurement $\Delta\theta_n^{\text{new}}$.

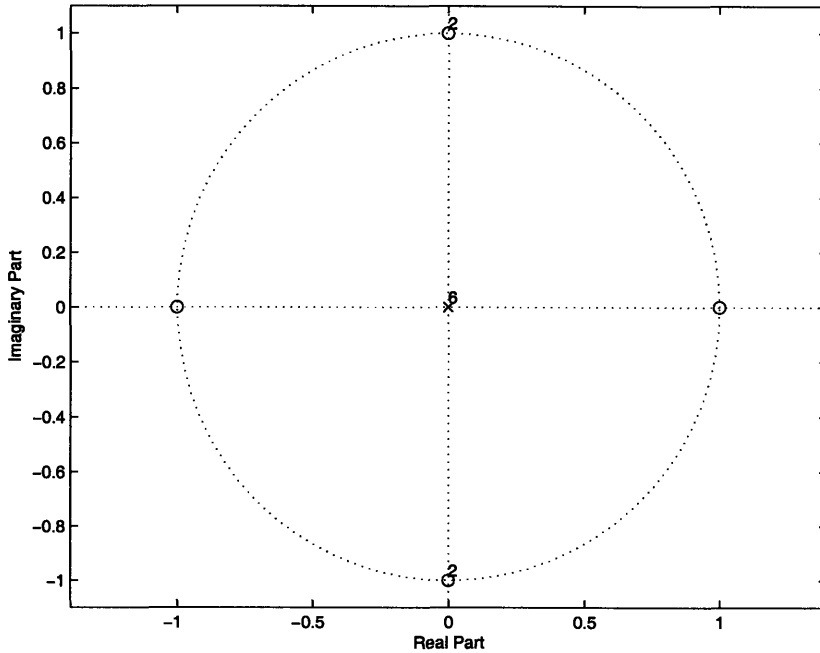


Figure 3-10: Zeroes and poles of $H(z)$.

3.3 High spatial-frequency noise in the mirror profile

In this section, we will discuss a technique to reduce the high spatial-frequency noise in the non-flatness measurement of the X-axis stage mirror profile. Fig 3-13(a) shows there are some sawtooth features in the measurement of the X-axis stage mirror non-flatness. When repeating the mirror non-flatness measurement, these sawtooth features are not constant. Thus these sawtooth features are a kind of high spatial-frequency noise. From Fig 3-13(b), we can see the noise amplitude is around 20 nm, which will dramatically reduce the precision of the Nanoruler when using the mirror profile measurement to correct the mirror non-flatness.

Where does the high spatial-frequency noise in the mirror non-flatness measurement come from? Fig. 3-14(a) shows two sets of $\Delta\theta$ measurements. In Fig. 3-14(b) we can see measurement noise by subtract $\Delta\theta_2$ from $\Delta\theta_1$, whose frequency content is shown in Fig. 3-14(c). The measurement noise in $\Delta\theta$ is the source of the high

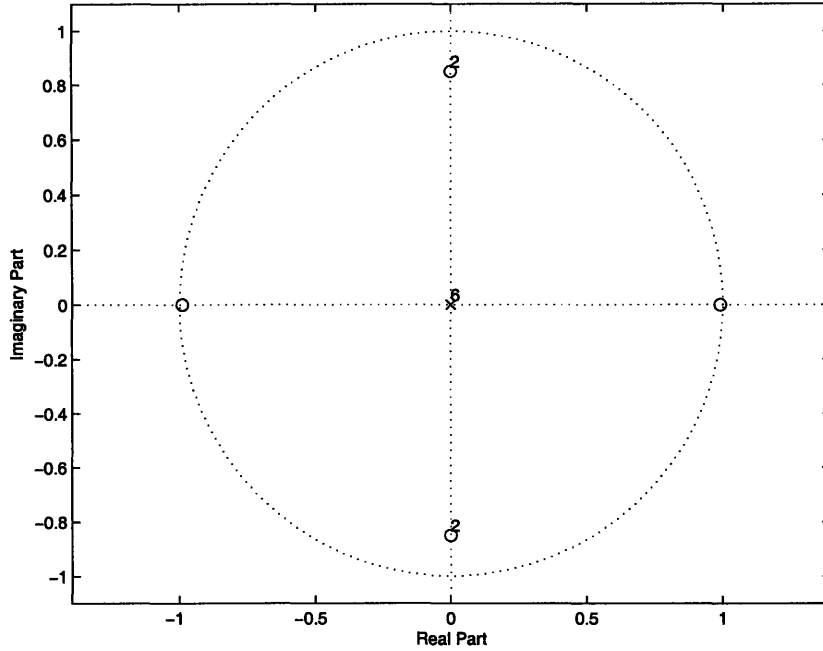


Figure 3-11: Zeros and poles of $H_a(z)$. Zeros are 0.99, -0.99, z_0 , z_0 , $-z_0$, $-z_0$ where $z_0 = 0.85e^{j\pi/2}$.

spatial-frequency noise in the mirror non-flatness measurement. The inverse transfer function method will blow up the part of $\Delta\theta$ noise whose normalized frequency is around 0.5 since the approximate transfer function $H_a(z)$ of the measurement process has a notch at the normalized frequency $\omega = 0.5$ (Fig 3-15).

Utilizing a low-pass filter to reduce the noise in $\Delta\theta$ is a promising method to reduce the high spatial-frequency noise of the mirror non-flatness measurement. Fig. 3-14(d) plots the frequency contents of $\Delta\theta_1$ together with that of $\Delta\theta_1 - \Delta\theta_2$. From it, we know in the frequency domain the data information of $\Delta\theta$ is primarily in a low-frequency band whose upper limit of normalized frequency is 0.25 (that is also the reason why $H_a(z)$ is a good approximation of $H(z)$). Therefore, we used Matlab to design a digital Butterworth low-pass filter $H_B(z)$,

$$H_B(z) = \frac{b_0 + b_1z^{-1} + b_2z^{-2} + b_3z^{-3} + b_4z^{-4} + b_5z^{-5} + b_6z^{-6} + b_7z^{-7} + b_8z^{-8} + b_9z^{-9}}{a_0 + a_1z^{-1} + a_2z^{-2} + a_3z^{-3} + a_4z^{-4} + a_5z^{-5} + a_6z^{-6} + a_7z^{-7} + a_8z^{-8} + a_9z^{-9}} \quad (3.21)$$

where $a_0 = 1$, $a_1 = -4.2785$, $a_2 = 8.8461$, $a_3 = -11.2842$, $a_4 = 9.6717$, $a_5 = -5.7301$,

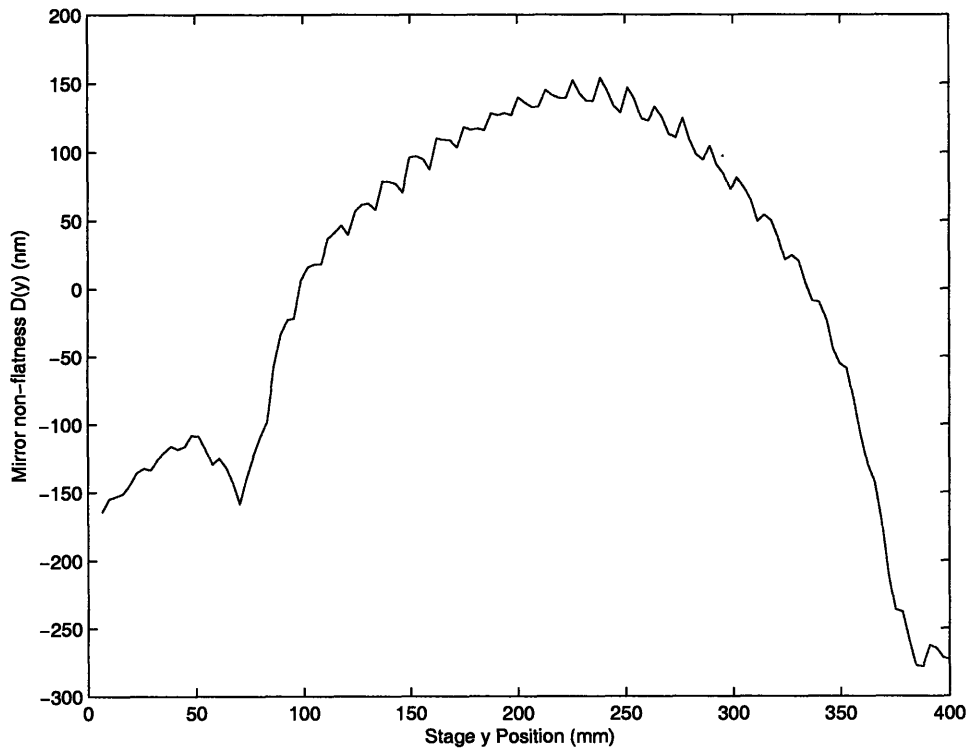


Figure 3-12: The non-flatness measurement of the X-axis stage mirror.

$a_6 = 2.3339$, $a_7 = -0.6276$, $a_8 = 0.1008$, $a_9 = -0.0073$, $b_0 = 0.0000$, $b_1 = 0.0004$,
 $b_2 = 0.0017$, $b_3 = 0.0041$, $b_4 = 0.0061$, $b_5 = 0.0061$, $b_6 = 0.0041$, $b_7 = 0.0017$,
 $b_8 = 0.0004$, and $b_9 = 0.0000$. The passband corner normalized frequency ω_p is
 0.25 with the maximum permissible passband loss of 3 dB, and the stopband corner
 normalized frequency ω_s is 0.4 with a 40 dB stopband attenuation. This IIR filter
 is shown in Fig 3-16. The reason why we choose the Butterworth filter is that the
 magnitude of the Butterworth filter in the low-pass band is almost equal to 0 dB,
 which will maximally preserve the mirror profile information that is critical for us to
 recover. However, another important thing we need to pay attention to is its phase
 delay. Fortunately, in the low-pass band this phase delay is almost linear. Based
 on the slope of the filter phase curve, we can make a corresponding spatial advance
 on the filtered data to eliminate the phase delay effect. The spatial advance for the

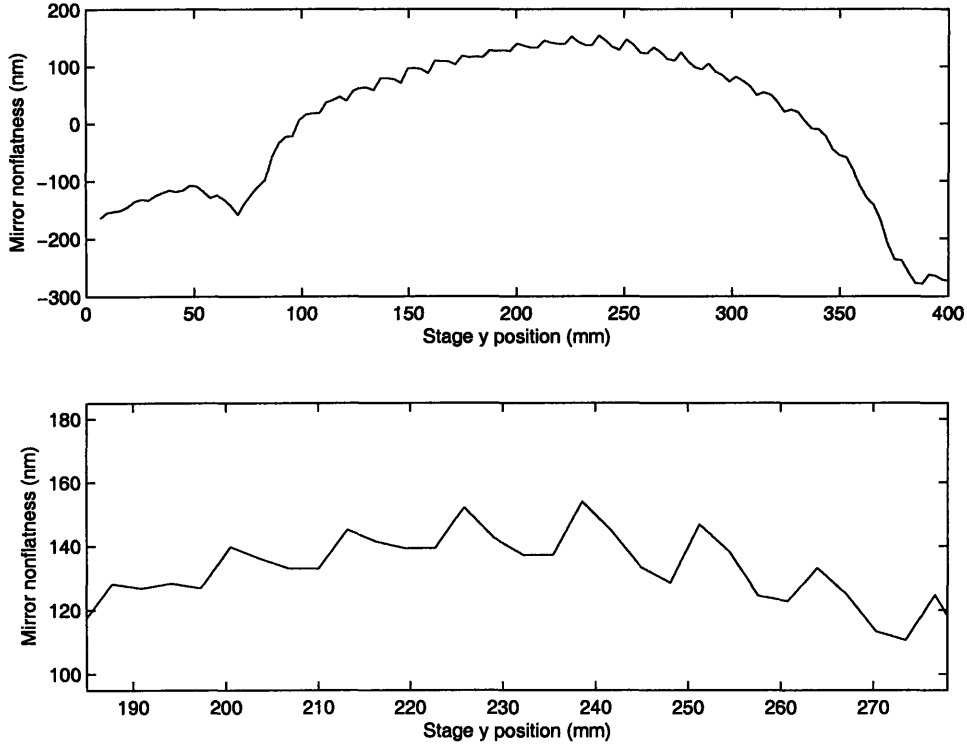


Figure 3-13: (a) The non-flatness measurement of the X-axis stage mirror. (b) An exaggerated part of the X-axis stage mirror non-flatness measurement.

phase delay correction is given by,

$$S_{adv} = \frac{\Phi_{delay}(f)}{2\pi} \cdot P_s(f) = \frac{slope \cdot f / (f_s/2)}{2\pi} \cdot \frac{V}{f} = \frac{slope}{2\pi} \cdot \frac{V}{f_s/2} \quad (3.22)$$

where S_{adv} is the spatial advance on the filtered data to correct the filter phase delay, $\Phi_{delay}(f)$ is the filter phase delay at the frequency f , $P_s(f)$ is the spatial period corresponding to the frequency f , $slope$ is the slope of the phase curve in the low-pass band in Fig 3-16 (that is, 22 samples), f_s is the sampling frequency (i.e., 10 Hz), and V is the stage scanning velocity (i.e., 32 mm/s). The spatial advance is calculated to be equal to 22.4 mm with Equation (3.22).

Before passing $\Delta\theta$ into the low-pass digital filter, we make the first data point of $\Delta\theta$ be equal to zero by subtracting it from the whole set of $\Delta\theta$ to avoid the non-zero step input effect (we add the first data point back to $\Delta\theta$ after filtering). There is no

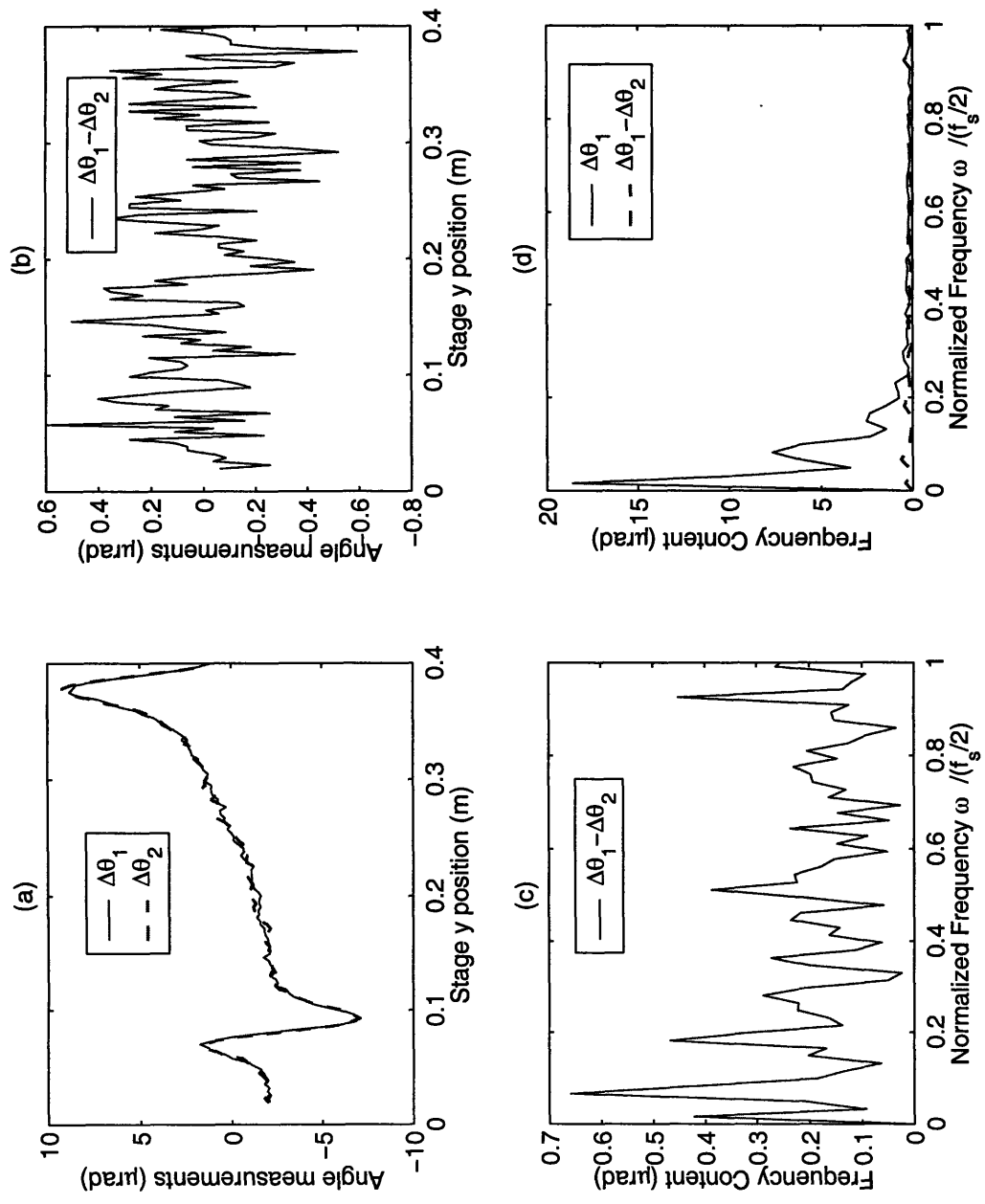


Figure 3-14: (a) Two sets of angle measurement $\Delta\theta$ before filtering, $\Delta\theta_1$ and $\Delta\theta_2$. (b) The $\Delta\theta$ measurement noise is $\Delta\theta_1 - \Delta\theta_2$. (c) Frequency content of $\Delta\theta_1 - \Delta\theta_2$. (d) Frequency contents of $\Delta\theta_1$ and $\Delta\theta_1 - \Delta\theta_2$.

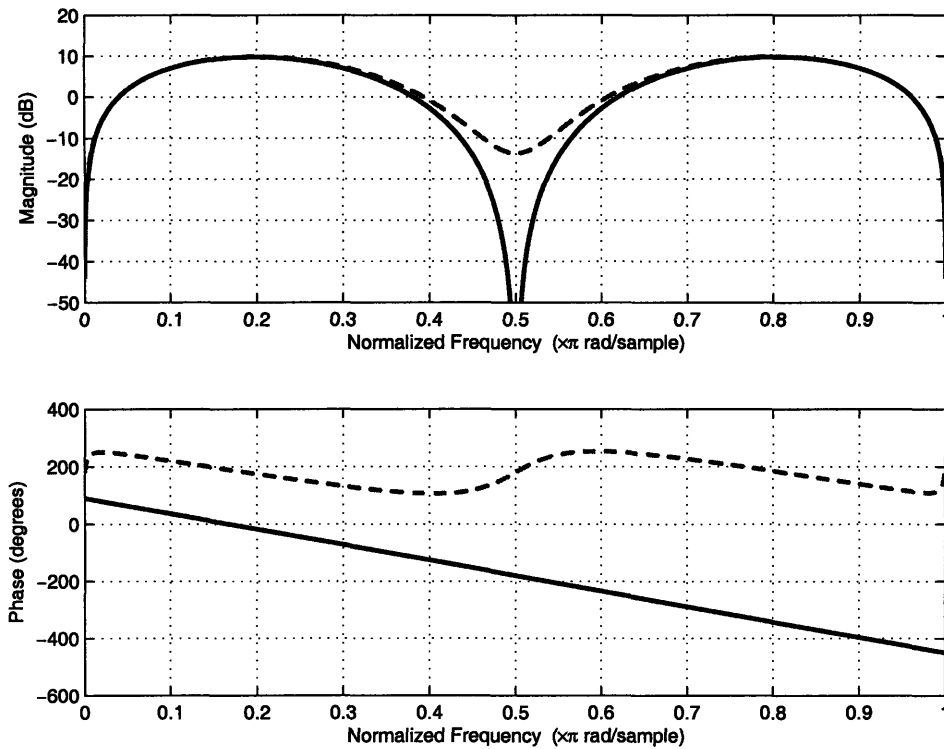


Figure 3-15: The solid line shows the transfer function $H(z)$; the dashed line shows its approximation $H_a(z)$.

ramp input issue since the beginning part of the $\Delta\theta$ curve is flat (Fig 3-14(a)). Fig 3-17 shows $\Delta\theta$ after passing the Butterworth low-pass filter. From the bottom graph, we can see the high-frequency noise in $\Delta\theta$ has been filtered out. After obtaining a clean $\Delta\theta$, we follow the same procedure as Montoya did to recover the X-axis mirror non-flatness, which is shown in Fig 3-18. Fig 3-19 compares the X-axis mirror non-flatness measurements with and without the low-pass filter and shows their corresponding frequency content. Note the original high spatial-frequency noise, whose normalized frequency is 0.5 (Fig 3-19(b)), has been reduced by 95 percent.

Fig. 3-20 shows the repeatability of measuring the X-axis stage non-flatness with the low-pass filter. I took two sets of the X-axis stage mirror non-flatness measurements within 2 minutes and subtracted the non-flatness measurements between one and another. When patterning gratings on the substrate, we only utilize the part of the X-axis stage whose coordinates along the Y direction are from $y = 0.075 m$

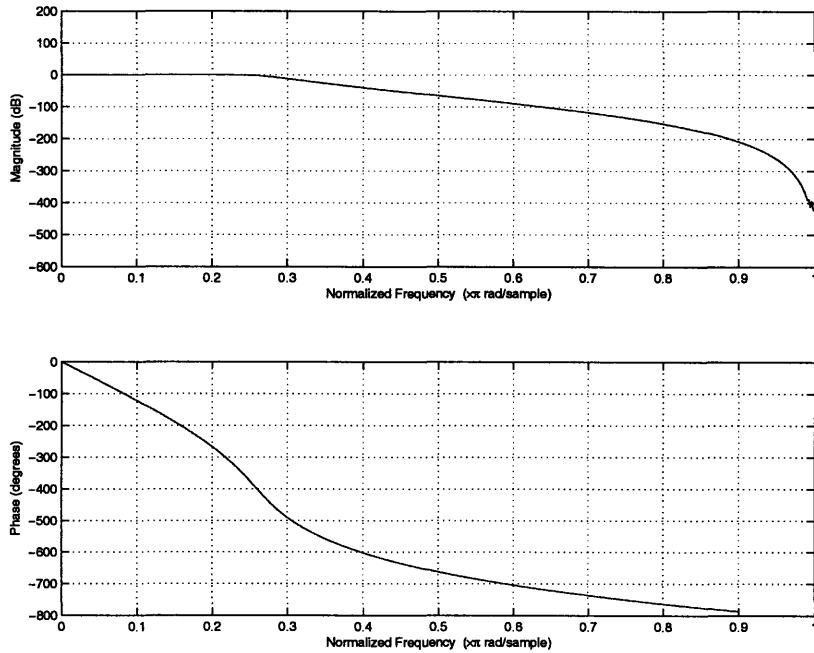


Figure 3-16: The 10th-order Butterworth low-path filter with the cutoff normalized frequency of 0.25. For the normalized frequency $\omega=0.5$, the attenuation of the filter is 65 dB.

to $y = 0.375$. Thus we can claim that the non-flatness measurement repeatability of the X-axis stage mirror portion that we actually utilizes during patterning is less than $\pm 1nm$. Of course, the mirror measurement error could be further reduced by averaging many mirror measurement sets.

3.4 Location-dependent mirror non-flatness

After reducing the high spatial-frequency noise in the mirror non-flatness measurement, in this section we will address another problem - that the mirror non-flatness appears to vary with the measurement location. Remember that we measure the X-axis stage mirror non-flatness by scanning the stage along the Y axis and keeping the x position of the stage constant. Now we take the mirror non-flatness measurement at different stage x positions (i.e., $x = 5\text{ mm}$, $x = 150\text{ mm}$, and $x = 300\text{ mm}$). Fig 3-21(a) shows these three sets of the mirror non-flatness measurements are not consistent. The mirror non-flatness appears to vary by several nanometers with the

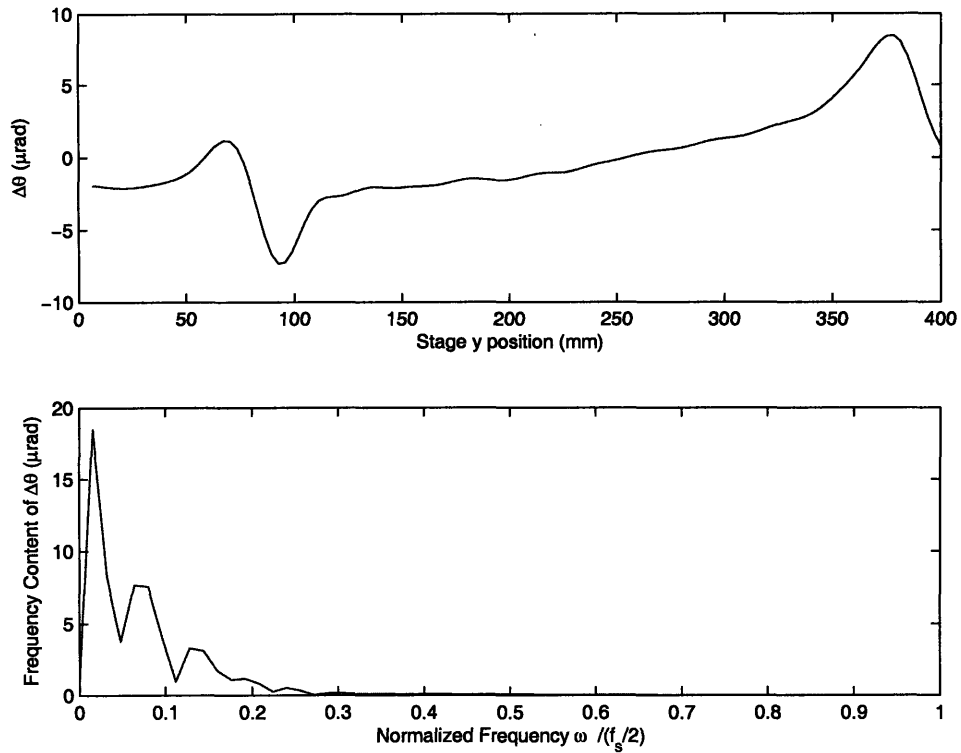


Figure 3-17: The filtered angle measurement $\Delta\theta$ (top graph) and its frequency content (bottom graph).

measurement location (i.e., the x position of the stage), which is shown in Fig 3-21(b).

After comprehensively considering the factors affecting the non-flatness measurement of the X-axis stage mirror, we proposed four possible reasons that may explain the location-dependent measurement of the mirror non-flatness. The location-dependent mirror non-flatness measurement may be caused by twisting of the optical bench with respect to the stage, thermal errors along the beam paths of the X-axis stage interferometer, location-dependent granite table deformation, or actual mirror shape change due to magnetic field variation or stage cable forces. In the rest of the section we will examine them one by one until we determine their main factor causing the problem.

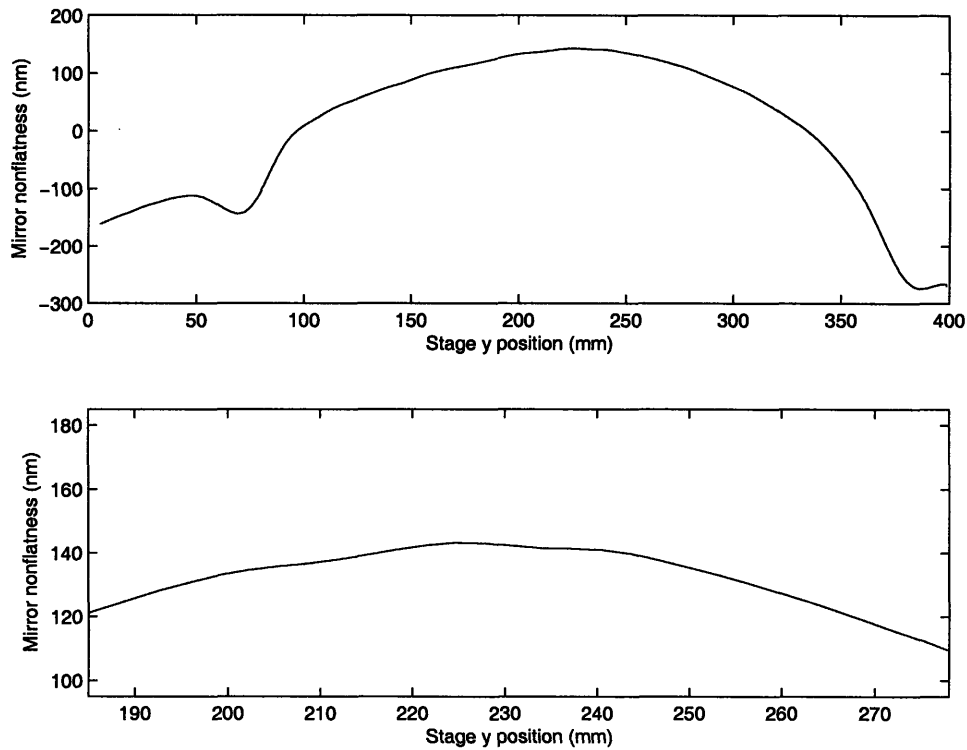


Figure 3-18: (a) The non-flatness measurement of the X-axis stage mirror with a low-pass filter. (b) The exaggerated part of the X-axis stage mirror non-flatness measurement with a low-pass filter.

3.4.1 Twisting of optical bench with respect to the stage

As we discussed in section 3.2, the X-axis stage interferometer measures the stage x position by measuring the relative displacement between the X-axis column mirror and the X-axis stage mirror. As shown in Fig 3-1, the X-axis column mirror is attached to the optical bench and the X-axis stage mirror is attached to the stage. Mechanical twisting of the optical bench with respect to the stage may occur during the stage movement, which will result in a location-dependent mirror non-flatness measurement if the twisting is large enough and location-dependent. Recall Montoya's technique to measure the mirror non-flatness. We measured the angle $\Delta\theta(y_w)$ and used the inverse transfer function method to solve Equation (3.15) and obtain the mirror non-flatness $D(y_w)$. In this technique, we assumed the X-axis column reference mirror is stationary. However, when mechanical twisting results in the rotation of the X-axis

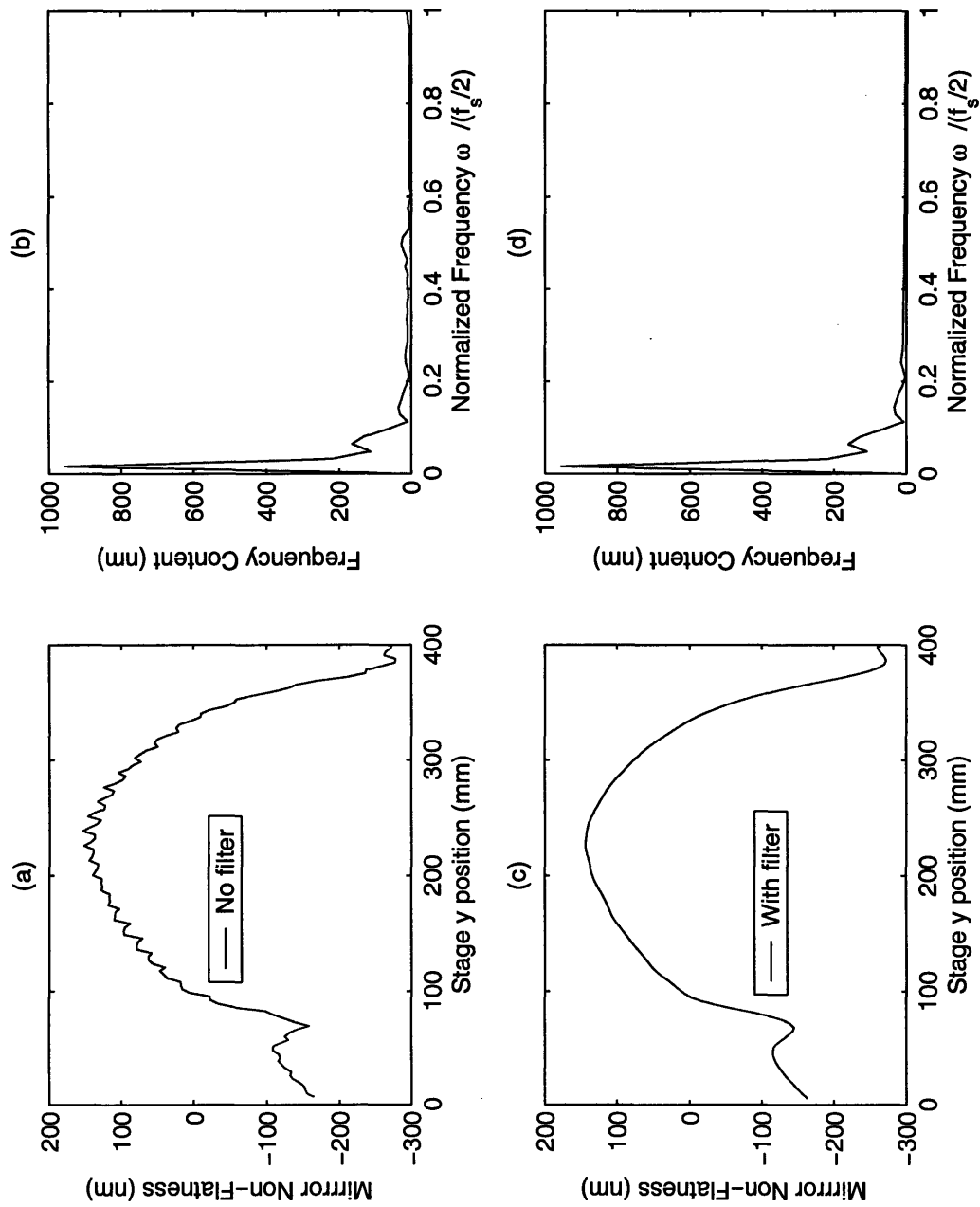


Figure 3-19: (a) The non-flatness measurement of the X-axis stage mirror without a low-pass filter. (b) The frequency content of the mirror non-flatness measurement in (a). (c) The non-flatness measurement of the X-axis stage mirror with a low-pass filter. (d) The frequency content of the mirror non-flatness measurement in (c).

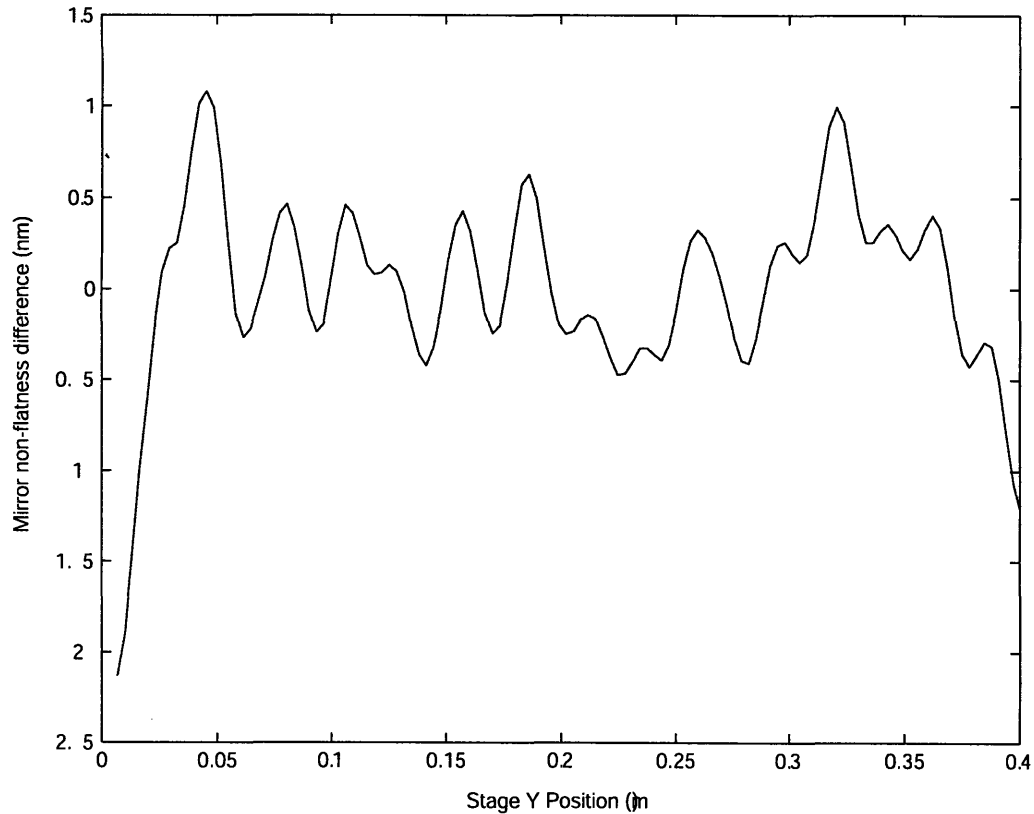


Figure 3-20: The repeatability of measuring the X-axis stage mirror non-flatness.

column mirror or the interferometer head, the stationary assumption is destroyed. There will be a measurement error in $\Delta\theta(y_w)$, which directly causes an X-axis stage mirror non-flatness measurement error. If the X-axis column mirror rotation caused by the mechanical twisting is location-dependent, the non-flatness measurement of the X-axis stage mirror will also show a location-dependent error.

In order to test whether the twisting is the reason for the location-dependent mirror non-flatness measurement, we use a mirror fixed to the head of the X-axis stage interferometer to replace the original X-axis column mirror. In this configuration, the mechanical twisting between the optical bench and the stage does not affect the mirror non-flatness measurement process. We remeasured the mirror non-flatness at different stage x positions (i.e., $x = 5 \text{ mm}$ and $x = 150 \text{ mm}$) and compared with the previous measurements taken at the same stage x positions but with the

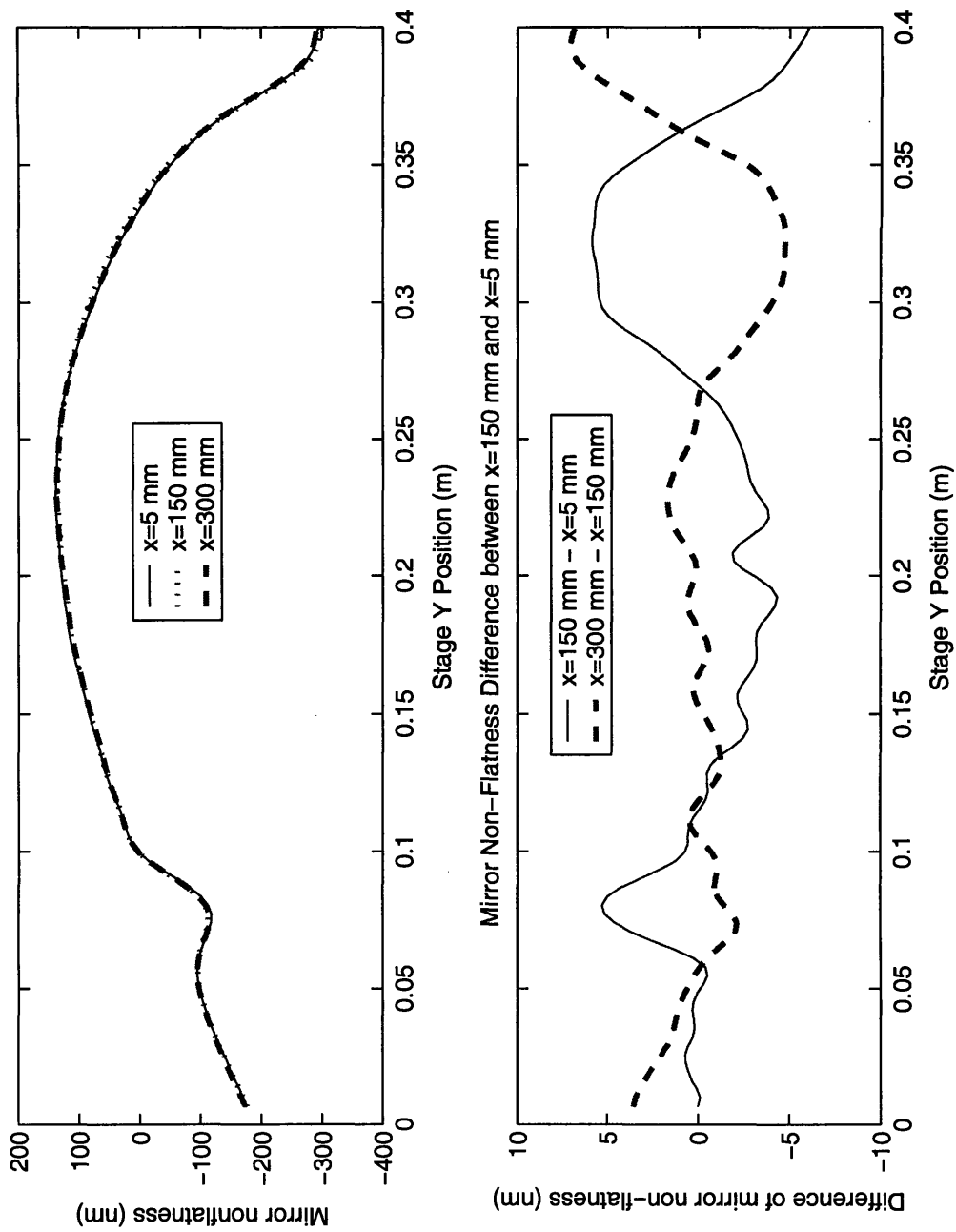


Figure 3-21: (a) Non-flatness measurements of the X-axis stage mirror at $x=5$ mm, $x=150$ mm, and $x=300$ mm. (b) The difference of the mirror non-flatness measurements at $x=150$ mm with respect to that at $x=5$ mm and the mirror non-flatness measurements at $x=300$ mm with respect to that at $x=150$ mm.

original X-axis column mirror. Fig 3-22 shows the location-dependency of the mirror non-flatness measurements does not disappear. We will proceed with the discovery process.

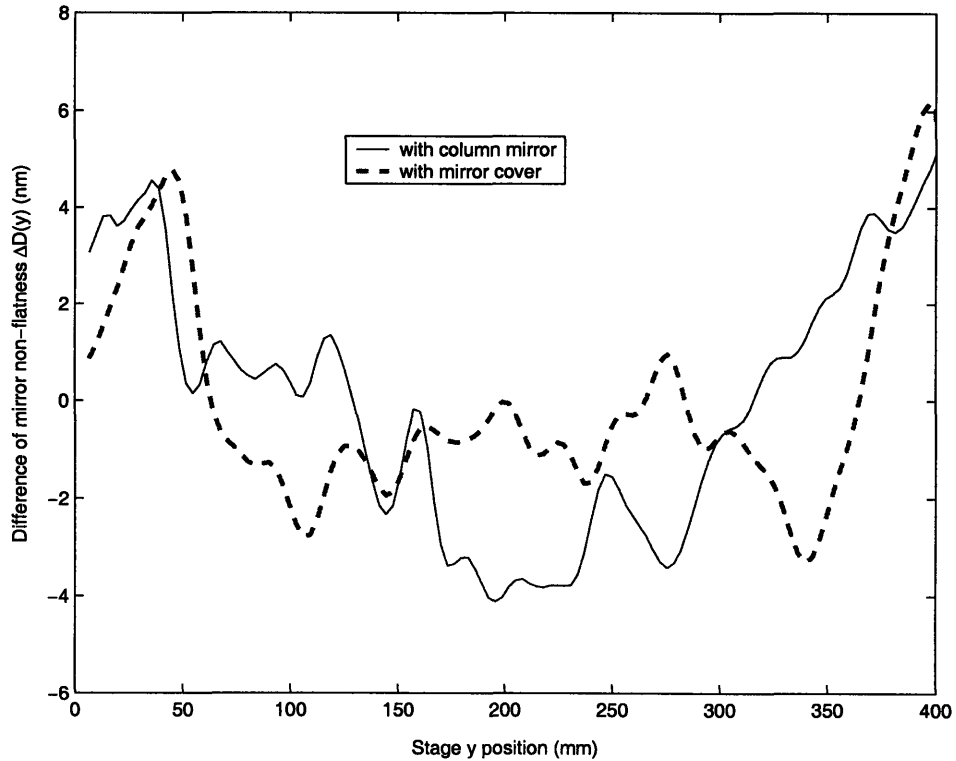


Figure 3-22: The solid line represents the difference of the X-axis stage mirror non-flatness measurement at $x=150$ mm with respect to the measurement at $x=5$ mm with the original X-axis column mirror. The dotted line represents the same kind of difference with a mirror cover fixed in the front of the X-axis stage interferometer head.

3.4.2 Thermal errors along the X-axis stage interferometer beam paths

In this subsection, we will discuss the possibility that the location-dependency of the mirror non-flatness measurements is due to the temperature gradients, which is one kind of thermal error, among the X-axis stage interferometer beam paths. In Chapter 2, we measured the temperature gradients in some critical planes inside the environmental enclosure of the Nanoruler. From the measurements we know

there should exist temperature gradients among the beam paths of the X-axis stage interferometer. If the temperature gradient varies with the stage location, it will cause a change of the air refractive index along the X-axis beam paths, which will change the wavelength of the laser of the stage interferometer. Thus the phase detected by the stage interferometer will change due to the change of the laser wavelength. Since the stage interferometer measures the stage position based on measuring the phase change during the stage movement, the change of the air refractive index will lead the stage interferometer to wrongly conclude the stage position is changing but in fact it is the change of air index that results in the phase change being detected by the stage interferometer. Therefore, based on the above analysis, the X-axis stage interferometer will measure the wrong x position of the X-axis stage mirror, which is equivalent to a measurement error of the X-axis stage mirror non-flatness. In other words, a location-dependent temperature gradient along the beam paths will lead to location-dependent measurement error of the mirror non-flatness, which makes the mirror non-flatness seem to vary with measurement location.

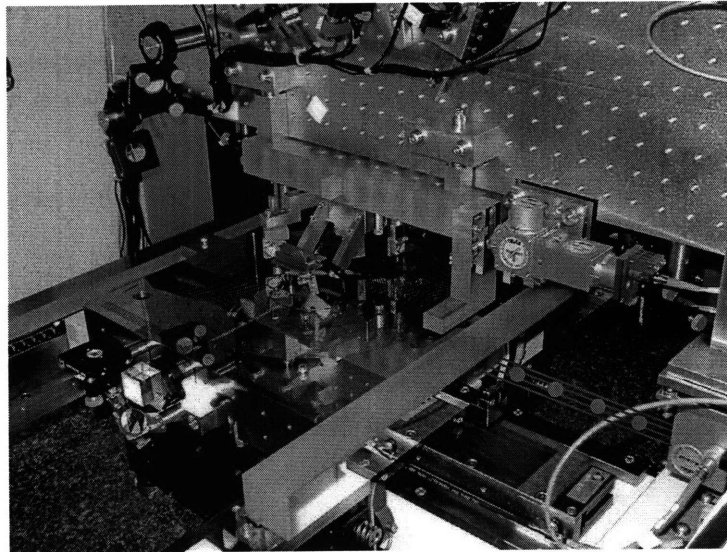


Figure 3-23: Locations of four thermistors placed along the beam paths of the X-axis stage interferometer with equal spacing.

We designed an experiment to determine whether temperature gradients along the beam paths are the reason leading to location-dependent mirror non-flatness

Table 3.1: Non-flatness measurement errors of the X-axis stage mirror due to the temperature gradients among the beam paths of the X-axis stage interferometer.

	y=25 mm (reference)	y=175 mm	y=325 mm
x=5 mm	0	0.1 nm	-0.1 nm
x=150 mm	0	-0.5 nm	0.7 nm
Mirror non-flatness measurement difference due to temperature gradients (<i>row 3 - row 2</i>)	0	-0.6 nm	-0.6 nm
Actual mirror non-flatness measurement difference between x=150 mm and x=5 mm	0	-3.5 nm	-5.0 nm

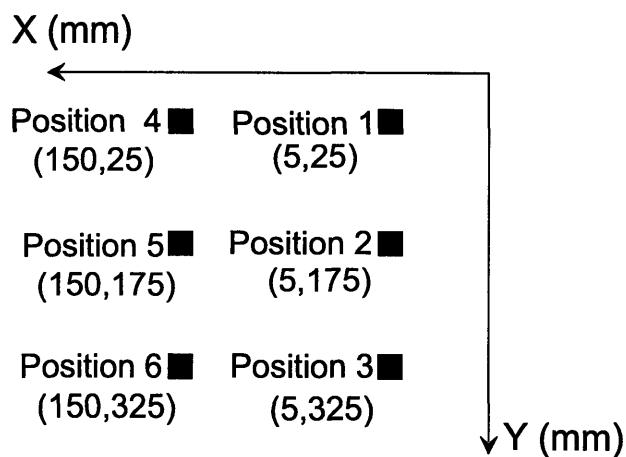


Figure 3-24: Six positions where the stage was located during temperature measurements.

measurements. As shown in Fig. 3-23, we placed four thermistors along the beam paths of the X-axis stage interferometer with the equal spacing. Fig. 3-24 shows the six stage positions. We took the temperature measurements from those four thermistors when the stage sequentially sits at those six positions. Fig. 3-25 shows the temperatures measured by the thermistors when the stage sitting at position 4, 5, and 6. At each stage position, we use the Edlan's equation (see Equation (2.2)) to calculate the refractive index of the air at the locations of the thermistors. Choosing position 4 as the reference and assuming temperature change is linear between two adjacent thermistors, the stage X-position measurement when the stage is located in position 5, $D(\text{position}5)$, is given by,

$$D(\text{position} 5) = \int n(x)dx = \sum_{i=1}^4 n_i(\text{position}5) \cdot M$$

where $n_i(\text{position} 5)$ represents the refractive index of the air at the location of the i th thermistor when the stage is at position 5 and M is the spacing between the adjacent thermistors.

The measurement error of the X-axis stage mirror non-flatness e can be obtained as below,

$$\begin{cases} e(\text{position} 5) = \sum_{i=1}^4 \frac{n_i(\text{position} 5) - n_i(\text{position} 4)}{n_i(\text{position} 4)} \cdot M \\ e(\text{position} 6) = \sum_{i=1}^4 \frac{n_i(\text{position} 6) - n_i(\text{position} 4)}{n_i(\text{position} 4)} \cdot M \end{cases} \quad (3.23)$$

where $e(\text{position} 5)$ and $e(\text{position} 6)$ are respectively the X-axis stage mirror non-flatness measurement errors when the stage is located at position 5 and position 6, and $n_i(\text{position} 6)$ and $n_i(\text{Position} 4)$ follow the same definition as $n_i(\text{position} 5)$.

After choosing position 1 as the reference, we can use the same method to calculate the measurement errors of the X-axis stage mirror non-flatness when the stage is at position 2 and position 3. The second and third rows of Table 3.1 list the mirror non-flatness measurement errors when the stage sits at positions 1-6. From the fourth and fifth rows of Table 3.1, we see the mirror non-flatness measurement errors due to the temperature gradients among the beam paths can only explain 10~20% of the

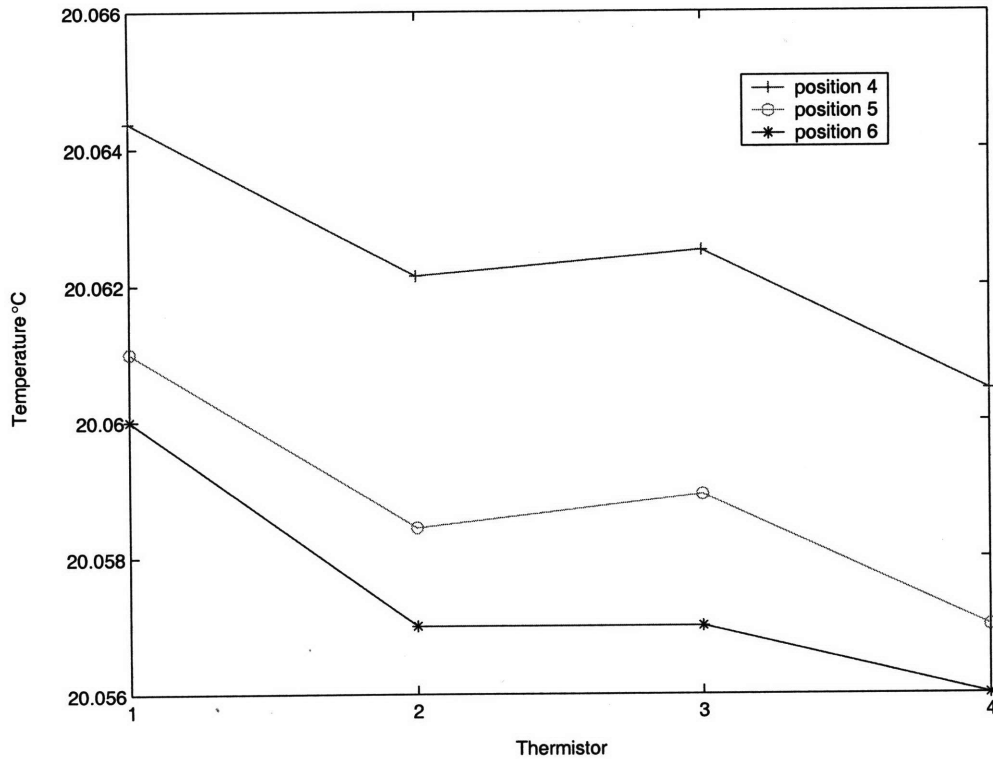


Figure 3-25: Temperature measurements of the four thermistors when the stage is sequentially located at position 4-6.

actual mirror non-flatness measurement difference.

3.4.3 Granite table deformation

The main part of the Nanoruler sits on a large granite table (55 inch \times 48 inch \times 12 inch). The deformation change of the granite table during stage motion is also a possible cause measurement error of the X-axis stage mirror non-flatness. The X-axis stage interferometer head is fixed on the granite table by four screws. When there are the deformations at the locations of these four screws, a yaw rotation of the interferometer head will be generated. The same thing can occur with the Y-axis stage interferometer head. When the yaw rotation of the X-axis interferometer head is different with that of the Y-axis interferometer head, which is likely to occur,

there will be angle measurement errors for $\Delta\theta$. Recall from Montoya's technique we introduced in Section 3.2, the measurement errors of $\Delta\theta$ will induce measurement error of the X-axis stage mirror non-flatness. If the deformation of the granite table depends on the location of the stage, then the non-flatness measurement error of the X-axis stage mirror is also location-dependent.

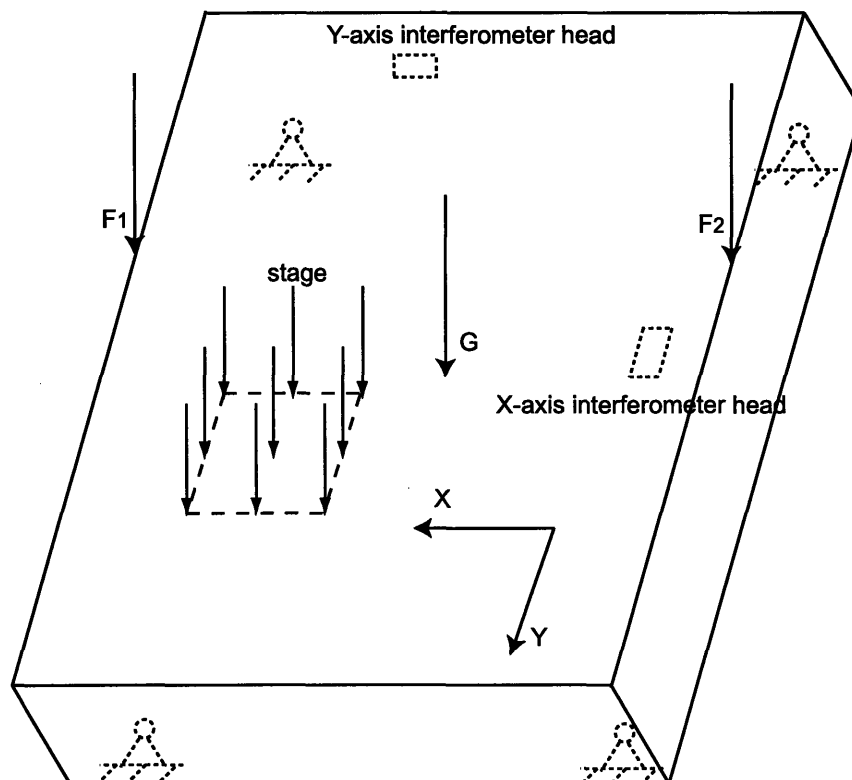


Figure 3-26: The ProE simulation model.

My labmate, Mireille Akilian, helped me to simulate the deformation of the granite table using ProE. The simplified model we built up in ProE is demonstrated in Fig. 3-26. The 55-inch long \times 48-inch wide \times 12-inch thick cuboid granite table sits on four hinges. There are no translation but rotation freedoms between the granite table and the four hinges because in actual the table is supported by an vibration isolation system and linear motors of the vibration isolation system make the positions of the table unchanged in all translation directions. The stage is modelled as an 100-kg load

uniformly acting in a 12 inch by 12 inch area. F_1 and F_2 represent the load of the optical bench together with the optics on the bench. G represents the gravity of the granite table. We simulate the deformation of the granite table when the stage is at four points A(x=300 mm, y=175 mm), B(x=150 mm, y=175 mm), C(x=300 mm, y=325 mm), and D(x=150 mm, y=325 mm). Fig. 3-27 shows the simulation result of the Y-axis deformation of the granite table when the stage is at point A. Based on the simulation results on the granite table deformation along the X and Y axis, the measurement errors of $\Delta\theta$, which is $\Delta\theta_e$, can be calculated and listed in Table 3.2, where $\Delta\theta_e$ with a positive sign is defined as clockwise. The measurement error of the X-axis stage mirror non-flatness when the stage is at point B ($e(B)$) is given by,

$$e(B) = 2h \cdot \Delta\theta_e(B) \quad (3.24)$$

where $h = 6.4 \text{ mm}$ is the spacing between the adjacent beams of the X-axis stage interferometer.

Table 3.2: The angle measurement error $\Delta\theta_e$ and the mirror non-flatness measurement error e due to the deformation of the granite table when the stage is at point A(x=300 mm, y=175 mm), B(x=150 mm, y=175 mm), C(x=300 mm, y=325 mm), and D(x=150 mm, y=325 mm).

	point A	point B	point C	point D
$\Delta\theta_e (\mu rad)$	0.12	-0.06	-0.02	-0.01
$e (nm)$	1.6	-0.8	-0.2	-0.1

The third row of Table 3.2 lists the mirror non-flatness measurement error e due to the granite table deformation when the stage sits at point A, B, C, and D. From Table 3.3 we can see the mirror non-flatness measurement error due to the granite table deformation provides a plausible explanation on the location-dependency of the

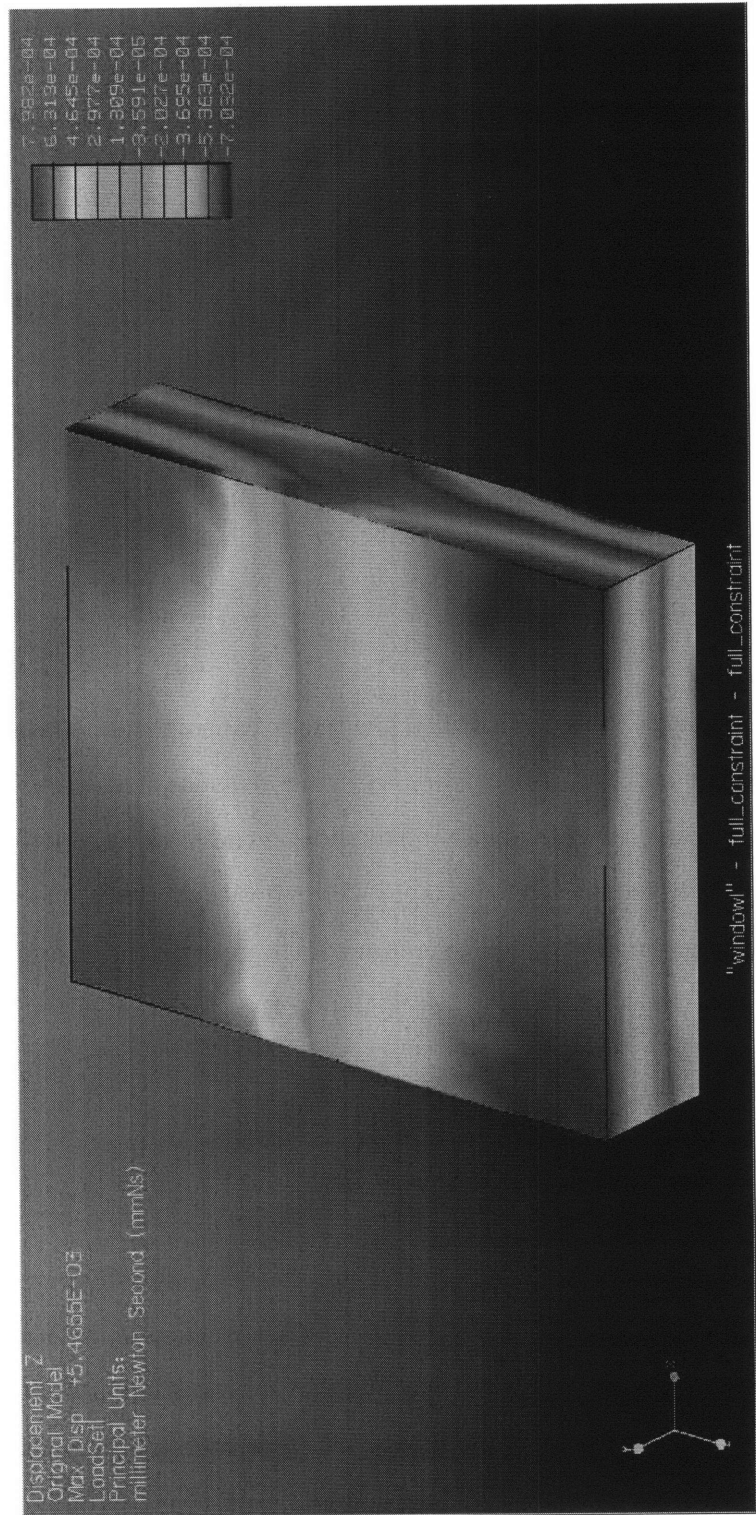


Figure 3-27: The ProE simulation result for the Y-axis deformation of the granite table when the stage is at point A(x=300 mm, y=175 mm). Note the frame in the ProE simulation is defined differently with the XY frame. The z axis in the simulation is equivalent to the Y axis and the x axis of the simulation has the opposite direction with the X axis. The unit in the color bar is millimeter.

X-axis stage mirror non-flatness measurements.

Table 3.3: The difference of the non-flatness measurements of the X-axis stage interferometer

The mirror non-flatness measurement difference	y=50 mm (reference position A & B)	y=200 mm (position C & D)
The value that can be explained by simulation	0	-2.5 nm
The actual value	0	$-4 \text{ nm} \pm 1 \text{ nm}$

Finally, we believe we have identified the factor causing the non-flatness measurement of the X-axis stage mirror to vary with the measurement location. In order to reduce the measurement error of the mirror non-flatness, we can perform the mirror non-flatness measurement at the $x = 150 \text{ mm}$ position where the deformation of the granite table is smallest so as to minimize the X-axis stage mirror non-flatness measurement error.

3.5 Summary

In this chapter we reduced another source of error affecting the precision of the Nanoruler - the measurement errors of the non-flatness of the X-axis stage mirror. First we developed a technique to reduce the high-frequency noise in the mirror non-flatness measurement. Later we carried out several experiments and identified the factor that results in the X-axis stage mirror non-flatness measurements depending on measurement location. Afterwards a corresponding solution is proposed to reduce the location effect on the mirror non-flatness measurement. Table 3.4 lists the improved patterning precision of the Nanoruler and the main sources of error affecting it. After the work of Chapter 2 and 3, the patterning precision of the Nanoruler has been

improved to about 3 nm, which satisfies the overlay error budget (Section 1.5).

Table 3.4: The main sources of error affecting the patterning precision of the SBIL system

Error Category	Corresponding Error (after my work)	Comments
X-axis stage mirror non-flatness measurement error	~ 2 nm	
Changes in the refractive index of air	0.6 nm	for 300 mm substrate; ±1 m°C thermal control
Thermal expansion of the substrate chuck	0.4 nm	for 300 mm substrate; ±1 m°C thermal control
60 Hz noise	1.1 nm	
Phase distortion of interference fringes	~ 1 nm	
Patterning precision of the Nanoruler	~ 3 nm	

Chapter 4

Spatial frequency multiplication - phase control

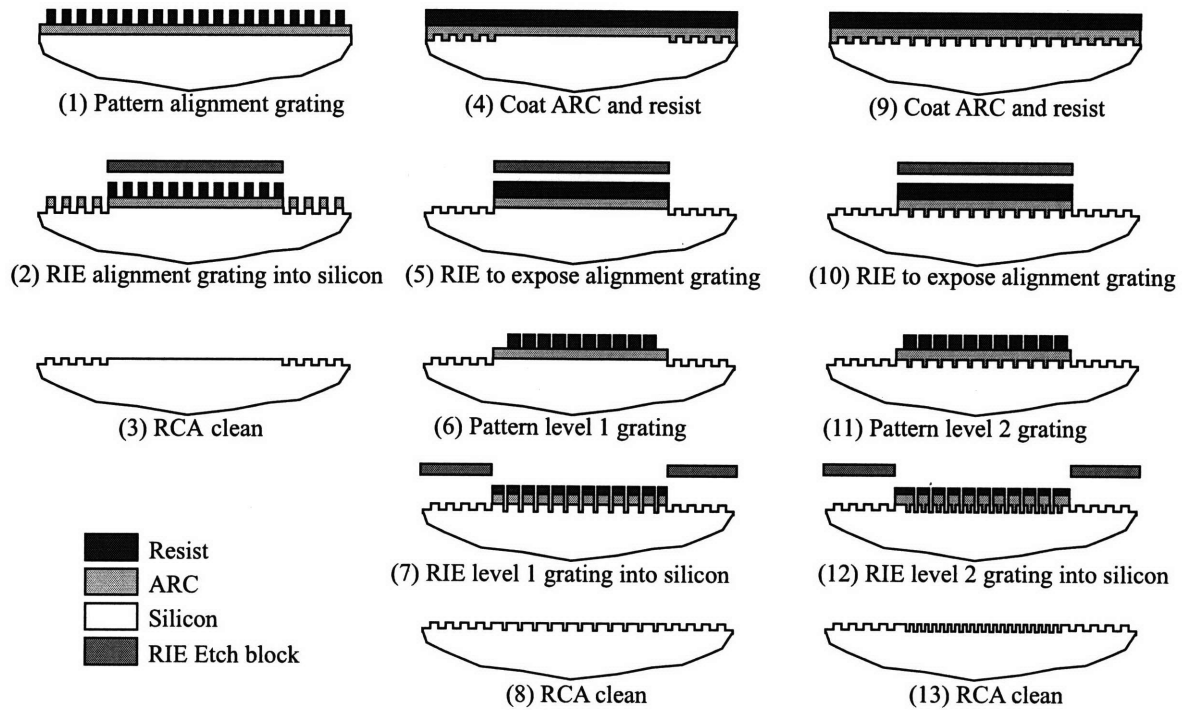
4.1 Introduction

In this chapter we will discuss how to accurately place grating patterns with respect to previous patterns when utilizing multi-exposure spatial frequency multiplication to fabricate high spatial-frequency grating patterns. Section 4.2 will introduce the process how to achieve spatial frequency doubling. In section 4.3 an interference fringe phase control technique will be discussed. The experiment results of spatial frequency multiplication will be shown in section 4.4. Section 4.5 will discuss the substrate distortion issues. The chapter will be summarized in Section 4.6.

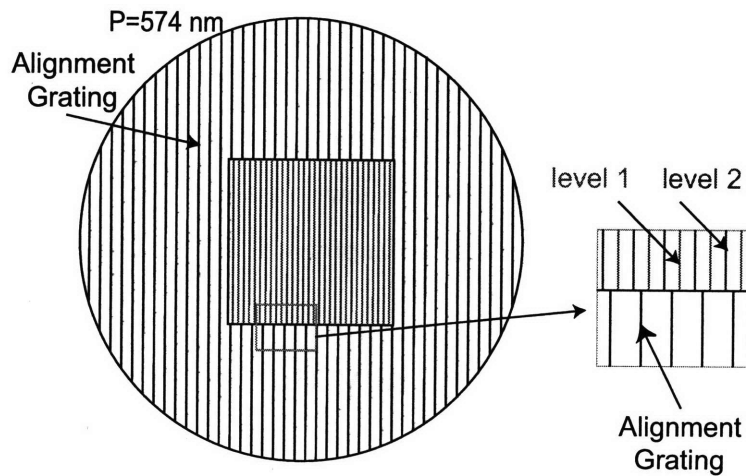
4.2 Spatial frequency doubling process

This section talks about the process of spatial frequency doubling. As discussed in Section 1.5, multi-exposure spatial frequency multiplication is a promising technique to achieve high spatial-frequency periodic patterns, which have many applications in nano-magnetics, nano-photonics, precision metrology, and other fields.

Fig. 4-1a summarizes our process for achieving frequency doubling. The first step (1-3) is to form a grating pattern of pitch $p = 574 \text{ nm}$ in the outer areas of



(a) Spatial Frequency Doubling Processing Steps



(b) Phase Control of Spatial Frequency Doubling

Figure 4-1: Schematic depiction of the spatial frequency doubling technique. (a) Spatial frequency doubling processing steps. (b) Phase control of spatial frequency doubling.

the photoresist, which is then developed and etched into the silicon substrate as the "alignment grating." (We expose the grating pattern with the pitch $p = 574 \text{ nm}$ because the Nanoruler was set at this pitch when the experiment was conducted.) The wafer is then coated with a new anti-reflection coating (ARC) and photoresist in the central area. In the second step (4-8), after measuring the angle, period, and phase of the alignment grating, the level 1 pattern is placed on the substrate in the central area with the same grating angle and period as the alignment grating but with a certain phase shift. This pattern is then developed and etched into a silicon substrate. Afterwards new ARC and photoresist are spun in the central area. In the final step (9-13), we place the level 2 pattern with the same grating angle and period as the alignment grating, but with a different phase shift.

Phase control of frequency doubling is shown schematically in Fig. 4-1b. As shown in the enlarged window, the level 1 pattern has a $\pi/2$ phase shift with respect to the alignment grating, and there is a $3\pi/2$ phase shift between the level 2 pattern and the alignment grating. Therefore, we achieve a π phase shift between the level 1 and level 2 patterns in the central area, which means the spatial frequency of the original pattern is doubled. At the beginning of the next Section, we will explain why we can not directly place the level 2 pattern with a π phase shift with respect to the level 1. My research will focus on the phase control techniques crucial to spatial frequency doubling. The nanofabrication process is developed by my labmate, Mr. Chih-Hao Chang.

The Nanoruler, which is introduced in Section 1.3, is utilized to fabricate grating patterns over large areas. Measuring the phase of the alignment grating is very important for correctly placing subsequent patterns on the substrate with respect to previous patterns. The nanoruler provides two phase detection schemes: homodyne and heterodyne reading modes (please see Section 1.3.2 for details).

4.3 Interference fringe phase control technique

In spatial frequency multiplication, one of the most critical tasks is to accurately place subsequent grating patterns with respect to the alignment grating, which is also called phase control of the overlay. Recall our overlay goal is to obtain a 1σ overlay error of less than 3 nm. Based on this objective, three key variables (the angle, period, and phase) of the alignment grating are measured with high accuracy and utilized to position subsequent patterns with respect to the alignment grating. Fig. 4-2 shows how errors in the angle, period, and phase measurements of the alignment grating will cause overlay position errors. When there is an angle offset (β) between two overlaid layers of gratings, an overlay position error, $E_{angle} = L \tan\beta$, will be induced, where L is the size of the overlay area. A ΔP period difference between two overlaid layers will result in a $E_{period} = \Delta P L/P_1$ overlay position error, where P_1 is the period of level 1 grating. For a phase error (Φ) between two overlaid layers, there will be a corresponding overlay position error of $P\Phi/2\pi$, where P is the grating period. As shown in table 1.2, alignment grating parameters measurement error is aimed to be controlled less than 2 nm. In this section, we will discuss how to achieve this goal.

First of all, we will discuss how to measure the grating phase with respect to the interference fringes using the homodyne reading mode (Section 1.3.2) because the angle, period, and phase measurements of the alignment grating are mainly based on this technique. The grating phase with respect to the interference fringes, Φ , can be detected by measuring the voltage readout from the linear photodiode (Fig. 1-5a). A photodiode, as a power sensor, integrates the light irradiance (i.e., intensity) over an active area [9]. The voltage measurement from a linear photodiode (V) is proportional to the intensity of the light irradiance (I) over the active area,

$$V = a \cdot I + b \quad (4.1)$$

where a is a proportionality constant and b is a voltage measurement offset.

With $I = c[1 + d \cdot \cos(\Phi)]$ and $\Phi = \Phi_{grating} - \Phi_{fringe} + \Phi_0$ [9], where c is a proportionality constant and d is the contrast of the image on the photodiode. We

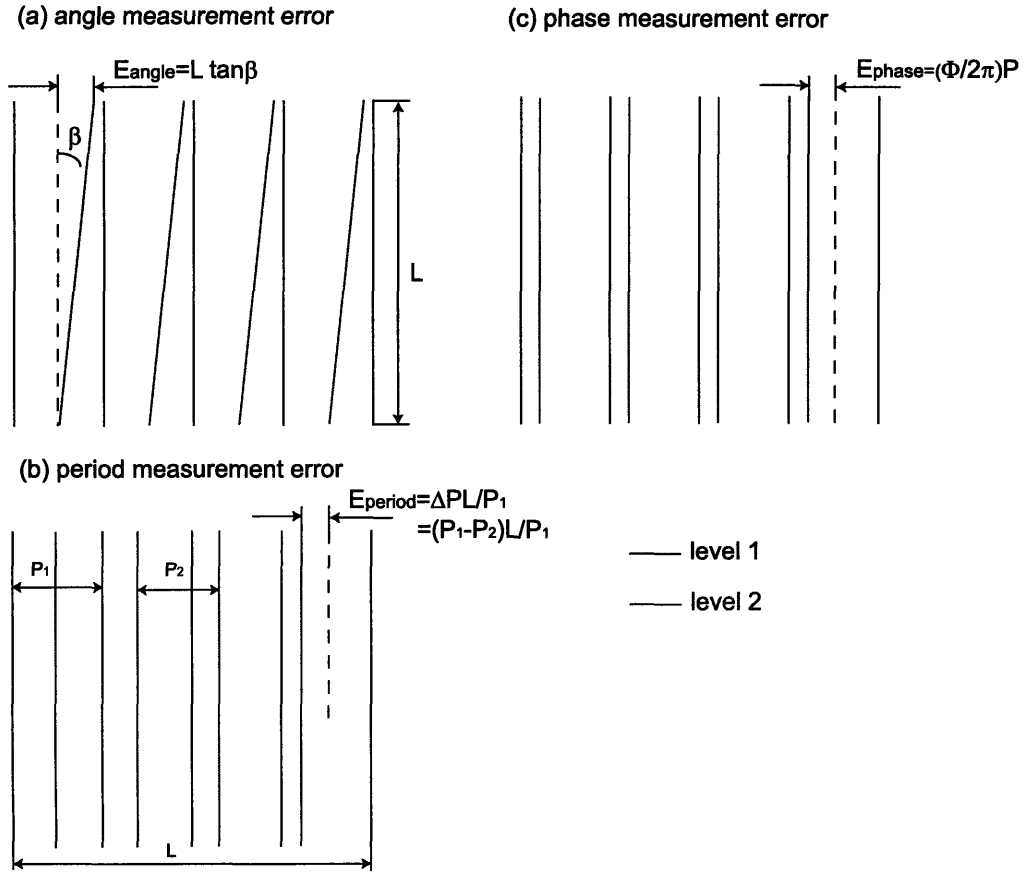


Figure 4-2: Schematic depiction of the alignment grating parameter measurement errors.

have,

$$V = ac + b + acd \cdot \cos(\Phi_{\text{grating}} - \Phi_{\text{fringe}} + \Phi_0) \quad (4.2)$$

where Φ_{grating} is the phase of the grating at the measurement point, Φ_{fringe} is the phase of the interference fringes, and Φ_0 is a phase offset dependent on the net change in OPL (optical path length) [9]. As we know in Section 1.3.1, the interference fringe locking function of the Nanoruler allows us to change the phase of the interference fringes with the AOM.

When taking the phase measurement at a single point, we can change the phase of interference fringes (Φ_{fringe}) to find the maximal and minimal measurements (V_{max}

and V_{min}) of the voltage readout. Based on Equation (4.2), we have,

$$V = \frac{V_{max} + V_{min}}{2} + \frac{V_{max} - V_{min}}{2} \cos(\Phi_{grating} - \Phi_{fringe} + \Phi_0) \quad (4.3)$$

Thus, the phase of the grating with respect to the interference fringes ($\Phi_{grating} - \Phi_{fringe}$) at the measurement location together with the phase offset (Φ_0), which is also referred as to the relative phase of the grating with respect to the interference fringes at the measurement location, is given by

$$\Phi_{grating} - \Phi_{fringe} + \Phi_0 = \Phi_{relative} = \arccos\left[\left(V - \frac{V_{max} + V_{min}}{2}\right) / \frac{V_{max} - V_{min}}{2}\right] \quad (4.4)$$

Note we can not obtain the absolute phase of the grating with respect to the interference fringes ($\Phi_{grating} - \Phi_{fringe}$) at the measurement location based on the voltage measurements since Φ_0 is unknown. Therefore, when conducting phase control between two overlaid grating patterns, we have to introduce another layer of grating (the alignment grating) to implement the phase control of the level 1 and level 2 patterns with respect to the alignment grating [35]. In this way, the effect of the phase offset Φ_0 can be counteracted.

When making the angle and period measurements of the alignment grating, we need to measure the phase variation between two points on the grating. First we measure the relative phase of the grating with respect to interference fringes at the first point (Φ_{start}). Then we translate the stage which holds the grating substrate from the first point to the second point. At the same time we count how many integral periods (N) the stage has traversed by counting the periodic changes of the voltage measurement of the photodiode. Finally we measure the relative phase of the grating with respect to the interference fringes at the second point (Φ_{end}). Thus the grating phase variation between these two points (Φ_{diff}) is,

$$\Phi_{diff} = \Phi_{end} - \Phi_{start} + 2\pi N \quad (4.5)$$

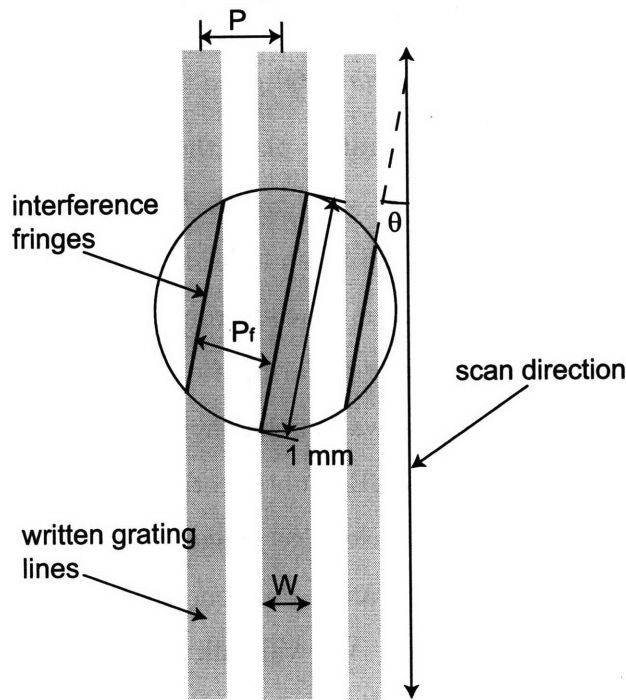


Figure 4-3: Demonstration that the angle difference between the scan direction and the interference fringes will increase the linewidth of grating patterns.

4.3.1 Angle measurement of the alignment grating

This subsection will discuss how to accurately measure the angle of the alignment grating. The angle of the alignment grating is utilized to pattern new gratings exactly along the direction of the alignment grating lines. In this way we place the two overlaid patterns (the level 1 and level 2 patterns) along the same direction. However, before exposing each level of pattern, we have to measure the angle difference between the alignment grating lines and the interference fringes and make sure this angle difference is small enough. Fig. 4-3 demonstrates when exposing grating patterns along the direction of the alignment grating lines, the angle difference between the scan direction (which is also the direction of the alignment grating lines since we scan the stage along the direction of the alignment grating lines) and the interference fringes, θ , will increase the linewidth of grating patterns by approximately $W = 1\text{ mm} \times \theta$, where the diameter of the interference image is 1 mm . In order to avoid bad contrast due to smearing in the exposed grating pattern, we need

$W < 0.1 p$, which means the angle difference between the alignment grating lines and the interference fringes $\theta < 0.1 p/1 \text{ mm} \approx 60 \mu\text{rad}$.

Now we will describe how we accurately place the substrate on the vacuum chuck to achieve a small enough θ (i.e., $10 \sim 30 \mu\text{rad}$). The Nanoruler is utilized in the Homodyne reading mode (Section 1.3.2) and the left and right arms meet at the alignment grating area of the substrate. The -1-order diffracted beam of the left arm and the 0-order diffracted beam of the right arm, after reflected by the pick-up window [9] will hit the same area of the side wall of the environmental enclosure. These two beams will interfere on the side wall. By subtly rotating the substrate on the chuck to maximize the contrast of the interference image, we place the substrate on the vacuum chuck. Then we measure the angle difference between the alignment grating lines and the interference fringes (θ). We will talk about how to measure θ during discussing how to accurately measure the angle of the alignment grating. If θ is larger than $30 \mu\text{rad}$, we will re-place the substrate using the same technique and measure θ again. We will re-place the substrate and measure θ till $\theta < 30 \mu\text{rad}$. In experiments, it usually takes me $2 \sim 3$ times to place the substrate with a $\theta < 30 \mu\text{rad}$. A rotatable chuck with micro-radian resolution will make the placement process much easier.

The scheme for measuring the angle of the alignment grating is illustrated in Fig. 4-4. The angle of the alignment grating, α , is defined as the angle of the alignment grating lines with respect to the Y axis. The XY frame is the laboratory frame, which has been discussed in Section 3.2.1. We first locate the stage at the beamsplitter position and utilize the beam alignment function of the Nanoruler to align the interference fringes to the beamsplitter interface with the tolerance of $\pm 5 \mu\text{rad}$ [9]. Then, still at the beamsplitter position, we measure the angle of the beamsplitter interface with respect to the Y axis, which is equal to the angle of the interference fringes with respect to the Y axis (θ_f). The method to measure the angle of the beamsplitter interface with respect to the Y axis can be described as the following. We locate the stage at the beamsplitter position, then scan the stage along different directions until we find a direction along which the interference fringe is scanned and the voltage measurement from the photodiode, which represents the phase of the

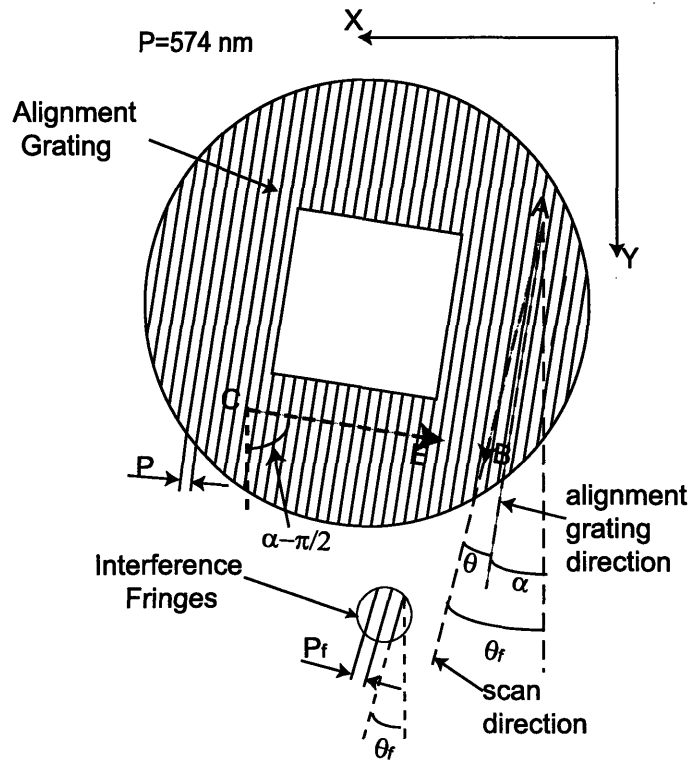


Figure 4-4: Scheme for measuring the angle (using path AB) and period (using path CE) of the alignment grating.

interference fringes with respect to the beamsplitter interface, is not changed. This direction is the angle of the beamsplitter interface with respect to the Y axis. Some readers may think the direction is the angle of the interference fringes with respect to the Y axis. We designed an experiment to confirm my claim. We measured this direction before and after rotating the interference fringes by $20 \mu rad$. The measurements of the direction were the same. Thus it is clear that the direction is the angle of the beamsplitter interface with respect to the Y axis.

Next we relocate the stage at point A. When scanning the interference fringes from point A with the angle of the interference fringes with respect to the Y axis (θ_f) to point B on the substrate, which is performed by moving the stage holding the substrate, the phase variation between two points is measured in the homodyne reading mode. The translation distance of the stage is measured by the stage interferometry system. The angle difference between the scan direction and the direction of the

alignment grating lines (θ), which is also the angle difference between the interference fringes and the alignment grating lines, is calculated by,

$$\theta = \frac{\phi_B - \phi_A}{2\pi K} p \quad (4.6)$$

where $\phi_B - \phi_A$ is the phase variation between points A and B on the grating (the measurement procedure has been discussed at the beginning of Section 4.3), p is the period of the alignment grating, and K is the distance between points A and B. Since the scan direction (θ_f) is known, the angle of the alignment grating with respect to the Y axis (α) can be obtained by

$$\alpha = \theta_f - \theta \quad (4.7)$$

Next we will discuss the magnitude of the angle measurement error and how large an overlay position error it will cause. In Equation 4.6 we approximate the actual value of p as the period by which we exposed the alignment grating. The period measurement variation of the grating is around 2 μm from day to day, which corresponds to less than 4 ppm for 574 nm-pitch grating. Since the angle difference between the alignment grating lines and the interference fringes, which is θ , is around 10 ~ 30 μrad , thus the angle measurement error due to the period approximation is less than 4 ppm \times 30 $\mu rad = 0.00012 \mu rad$. Another source of the angle measurement error is the phase measurement errors at points A and B. As we will discuss in Section 4.3.3, the phase measurement error at a single point is around 0.007 rad for 3σ when a 30-sec averaging filter is utilized. Thus the angle measurement error due to the phase measurement errors is $\sqrt{2} \times 0.007 \text{ rad} \times p/2\pi K = 0.028 \mu rad$ when the scanning distance $K = 30 \text{ mm}$ and $p = 574 \text{ nm}$. Thus the angle measurement error of the alignment grating is about 0.03 μrad . The corresponding overlay position error due to the alignment grating angle measurement error is 0.03 $\mu rad \times L = 0.9 \text{ nm}$, where $L = 30 \text{ mm}$ is the size of the overlay area.

4.3.2 Period measurement of the alignment gratings

This section will talk about the period measurement of the alignment grating. The period measurement of grating patterns on the substrate can change by $1 \sim 2 \text{ pm}$ daily, which is due to the variation of the stage laser wavelength ($\lambda = 632.8 \text{ nm} \pm 1 \text{ ppm}$) of the stage interferometer or the real period change of the grating patterns. Patterning new gratings using the just-measured period of the alignment grating can mitigate the effect of daily period change. A technique developed by Dr. Chen can be employed to measure the period of the alignment grating [9]. As shown in Fig. 4-4, we scan the interference fringes on the substrate with the angle of $\alpha - \pi/2$ with respect to the Y axis by a distance D . Using the homodyne reading mode, the phase variation during scanning is measured. The period of the alignment grating p is given by

$$p = \frac{2\pi D}{\phi_E - \phi_C} \quad (4.8)$$

where $\phi_E - \phi_C$ is the phase variation between points C and E on the grating (the measurement procedure has been discussed at the beginning of Section 4.3) and D is the distance between point C and point E.

The main error in the period measurement is due to the phase measurement errors at points C and E. As we will discuss in Section 4.3.3, the phase measurement error at a single point is around 0.007 rad for 3σ when a 30-sec averaging filter is utilized. The period measurement error due to the phase measurement error is $\sqrt{2} \times 0.007 \text{ rad} \times p/2\pi(D/p) = 0.01 \text{ pm}$ when the measurement distance (D) is 50 mm and $p = 574 \text{ nm}$, which results in a $0.01 \text{ pm} \times L/574 \text{ nm} = 0.6 \text{ nm}$ overlay position error, where $L = 30 \text{ mm}$ is the size of the overlay area. When the overlay area turns larger, in order to achieve the same overlay objective, the tolerance for the angle and period measurement errors turns smaller, which are inversely proportional to the size of the overlay area. Thus for the angle and period measurements, we have to increase the stage translation distance (K and D) proportional to the size of the overlay area.

When patterning new gratings with the just-measured period of the alignment

grating (p), the stage steps over by an integer number of p rather than the period of interference fringes (p_f). In order to avoid bad contrast due to smearing in the exposed grating pattern, we need the accumulated position error inside the interference image ($|p_f - p| \cdot S / p_f$) less than $0.1p$, where $S = 0.4285 \text{ mm}$ is the length that the stage steps between two consecutive scans. Thus $|p_f - p| < 80 \text{ pm}$, which means the difference of the period of the interference fringes and the period of the alignment grating should be less than 80 pm . After we measure the period of the alignment grating (p), we move the stage to the beamsplitter position to change the period of the interference fringes (p_f) so that $|p_f - p| < 80 \text{ pm}$. We can change the period of the interference fringes by changing the incident directions of the left and right beams of the Nanoruler. Dr. Chen discussed the beam alignment and period measurement in his thesis [9]. Also from his thesis, the angle adjustability of the left and right beams is $1.5 \text{ } \mu\text{rad}$. For the 574 nm -pitch grating, the period adjustability is $574 \text{ nm} \times \cot[\arcsin(351.1 \text{ nm}/2/574 \text{ nm})] \times 1.5 \text{ } \mu\text{rad} = 2.7 \text{ pm}$ [9], where 351.1 nm is the wavelength of the UV laser.

4.3.3 Phase measurement and control of overlaid gratings

This subsection will discuss how to carry out the phase measurement of the alignment grating and the phase control of overlaid patterns. In spatial frequency multiplication, it is critical that subsequent grating patterns have precisely controlled phase shifts relative to the alignment grating in order to insert new grating patterns between previous ones. Before patterning new grating patterns, the relative phase of the alignment grating with respect to the interference fringes (that creates the new grating patterns) at the measurement location is set to a desired value. At the beginning of Section 4.3, we have discussed the Nanoruler's capability of measuring the relative phase of the grating with respect to the interference fringes at a single point ($\Phi_{relative}$) with Equation 4.4 using the homodyne reading mode. As shown in Fig. 4-5(a), the photodiode (shown in Fig. 1-5a) voltage measurement noise is about $\pm 0.2 \text{ volt}$ (peak-valley), when we measure the relative phase of the alignment grating with respect to the interference fringes at a single spot over 200 seconds. By changing the phase of

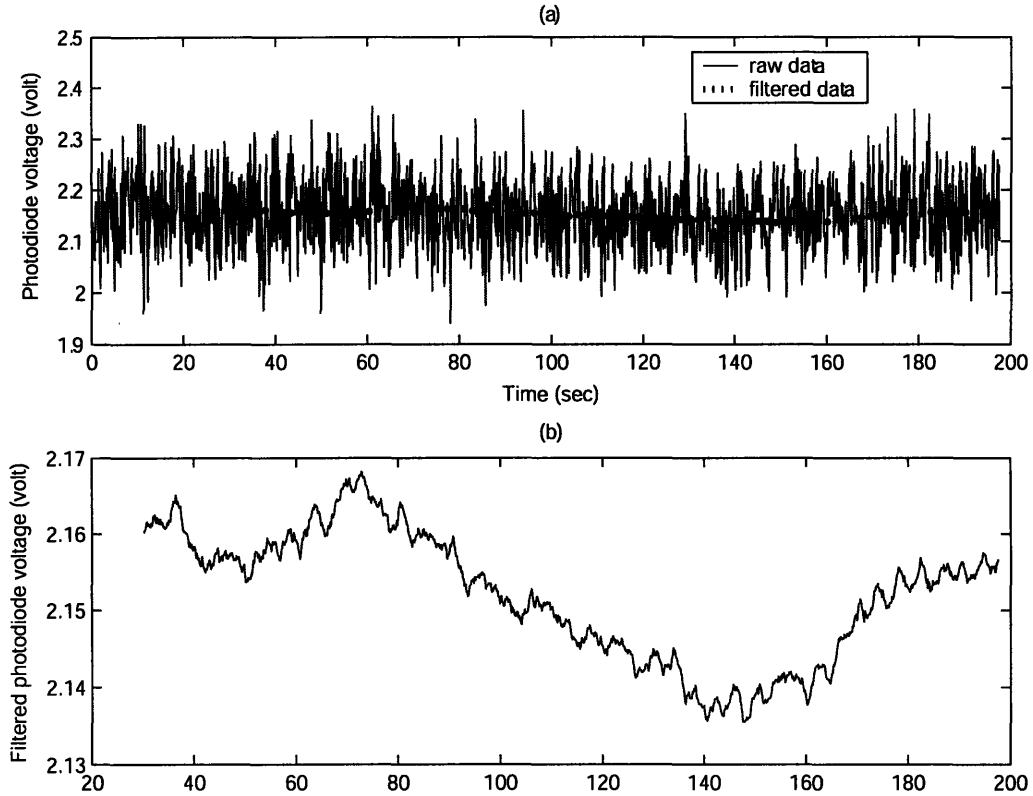


Figure 4-5: (a) The voltage measurements (raw data vs. filtered data) from the photodiode over 200 seconds for measuring the relative phase of the alignment grating at a single point. (b) The zoomed filtered measurements from the photodiode.

the interference fringes Φ_{fringe} , we find $V_{max} = 4.45 \text{ volt}$ and $V_{min} = 0.25 \text{ volt}$. With Equation (4.4), we can calculate the phase of the grating at the measurement location together with the phase offset, which is also referred to as the relative phase of the grating, as $1.618 \pm 0.048 \text{ rad}$. For a 574 nm-pitch grating, $\pm 0.048 \text{ rad}$ phase error corresponds to $\pm 4.4 \text{ nm}$ position error. Fig. 4-5(b) shows the photodiode voltage measurement data filtered by a 30-sec averaging filter. After filtering, the peak-valley noise of the voltage measurement shrinks to $\pm 0.015 \text{ volt}$, which is equivalent to $\pm 0.3 \text{ nm}$ position error. After measuring $\Phi_{relative}$, we can reset the relative phase of the alignment grating with respect to the interference fringes at the measurement location $\Phi_{relative}$ (that is equal to $\Phi_{grating} - \Phi_{fringe} + \Phi_0$) to a certain value by changing

the phase of interference fringes (Φ_{fringe}) with the interference fringe locking function of the Nanoruler (please refer to Section 1.3.1 for details). The Nanoruler can move the interference fringes with a precision of $574 \text{ nm}/512/2$ or about 0.6 nm . The accuracy of grating phase measurement and phase reset of the Nanoruler is about 1 nm . Table 4.1 summaries the errors of measuring alignment grating parameters. The total overlay position error due to alignment grating parameter measurement errors is around 1.6 nm , which satisfies our error budget.

Table 4.1: Errors of measuring alignment grating parameters

Error Category	Error amplitude	Corresponding overlay position error
Angle measurement error	$0.03 \mu\text{rad}$ (K=30 mm)	0.9 nm (L=30 mm)
Period measurement error	0.01 pm (D=50 mm)	0.6 nm (L=30 mm)
Phase measurement and reset error	0.007 rad (phase measurement) 0.6 nm (phase reset)	1.2 nm
Total		1.6 nm

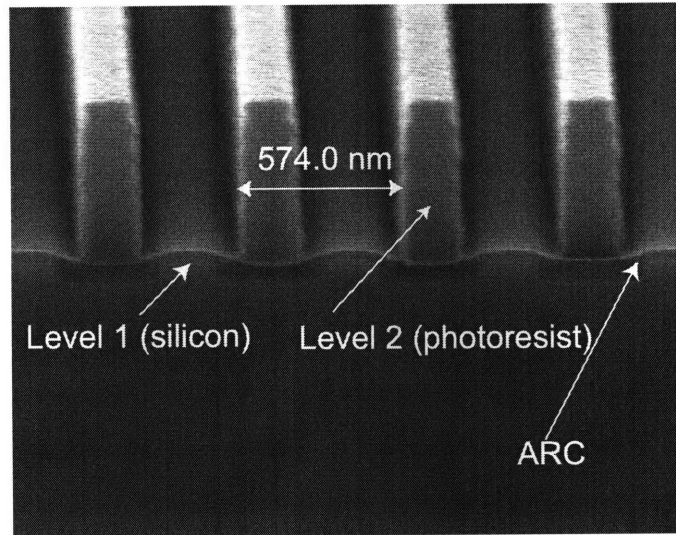
Remember that the level 1 pattern has a $\pi/2$ phase shift to the alignment grating and the level 2 pattern has a $3\pi/2$ phase shift to the alignment grating. Each time, before we pattern the level 1 and level 2 patterns, we measure the relative phase of the alignment grating with respect to the interference fringes at the measurement location ($\Phi_{grating} - \Phi_{fringe} + \Phi_0$) and set this relative phase equal to a certain phase value (i.e., $\pi/2$). For the level 1 pattern, we will directly expose the new gratings. For

the level 2 pattern, we will first change the phase of the interference fringes (Φ_{fringe}) by π using the fringe locking function of the Nanoruler so that the relative phase of the alignment grating at the measurement location is $3\pi/2$ and then expose the new gratings.

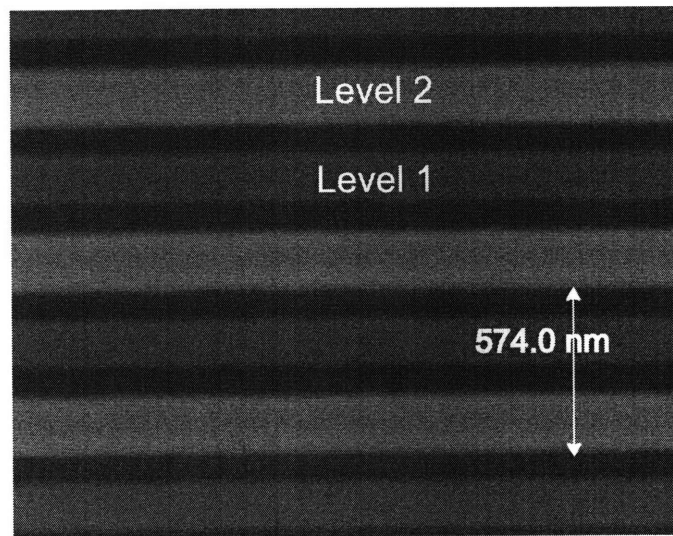
In order to minimize the alignment grating area, three small gratings could be used instead of a large one. Each grating should have an area no less than the area of the interference image whose diameter is around 1 *mm*. These gratings should be separately located at any three of four corners of the overlay area. Thus, the minimum area of the alignment grating could be as small as 3 *mm*².

4.4 Experimental results

This section will first show the experimental results of spatial frequency doubling with 574 nm-pitch pattern. After that 50 nm-pitch grating patterns fabricated by spatial frequency quadrupling will be shown. In Fig. 4-6 we show the result of a two-level overlay experiment at a single area of the wafer. Fig. 4-6(a) shows a cross-section SEM image of the overlay. The level 1 pattern has been etched into the silicon substrate and the level 2 pattern is exposed in the photoresist. Fig. 4-7 illustrates this cross-section SEM image. Top-view image with the same configuration of the level 1 and level 2 patterns is shown in Fig. 4-6(b), where the dark grey stripes represent the level 1 patterns and the light grey stripes represent the level 2 patterns. We utilized an electron microscope with X-Y automatic stage (Raith 150) to image the overlay area ($25 \times 32.5 \text{ mm}^2$) with a grid size of 2.5 *mm*. Fig 4-8 shows the Raith micrographs over $20 \times 12.5 \text{ mm}^2$ with a grid size of 2.5 *mm*. Based on the micrographs, the overlay phase errors between level 1 and level 2 gratings are calculated (Matlab code is attached in appendix). Fig 4-9 shows a 2-D overlay phase error map for a $25 \times 32.5 \text{ mm}^2$ area, demonstrating an average overlay error of -1.0 nm with a 1σ deviation of 2.8 *nm*. This level of accuracy can allow the fabrication of 50 *nm* pitch gratings via 4-factor spatial frequency multiplication starting from a period of 200 *nm*. Fig. 4-10 shows 50 nm-pitch grating patterns fabricated by spatial frequency quadrupling in the Space



(a) Cross-section SEM Image



(b) Top-view SEM Image

Figure 4-6: Electron micrographs of two-level overlay results. (a) Cross-section SEM image. The level 1 pattern has been etched into the silicon substrate. The level 2 pattern is exposed in the photoresist. (b) Top-view Raith image with the same configuration of the level 1 and level 2 patterns as (a). The photoresist is Sumitomo PFI-88 exposed with a wavelength of 351.1 nm.

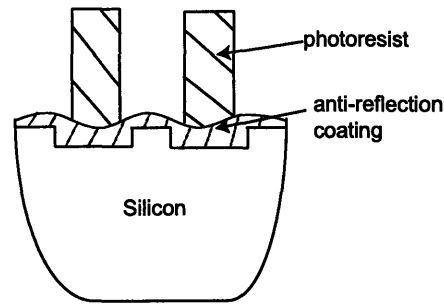


Figure 4-7: Illustration of the cross-section SEM image.

Nanotechnology Laboratory. An Intel 45-nm CMOS gate is also shown there with the same scale. Readers can see the linewidth of the 50 nm-pitch gratings, which is around 33 nm, is less than the smallest feature size of 45 nm CMOS device.

4.5 Substrate distortion issues

Recalling Table 1.2, another factor impairing the overlay accuracy is substrate distortion, which includes particle-induced substrate distortion, nonlinear distortion of the alignment grating, and pressure time-variance of the vacuum line of the chuck. In this section the effects of these factors are discussed and some techniques are described to minimize the corresponding effects.

4.5.1 Particle-induced Substrate Distortion

Any sizeable particle trapped between the back surface of the substrate and the chuck surface (Fig. 4-11) will cause in-plane distortion of the substrate [8], which results in measurement errors of the key variables (the angle, period, and phase) of the alignment grating, and results in the nonlinear distortion of grating patterns. The particle effect on the overlay is demonstrated in Fig. 4-12. Note that one particle trapped during the level 1 pattern exposure causes huge overlay phase errors (peak-to-valley error is more than 200 nm) over a large area. Improvement in the cleaning of the back surface of the substrate and the chuck surface can decrease the number of particles and limit the particle size, which can reduce the particle effect to some

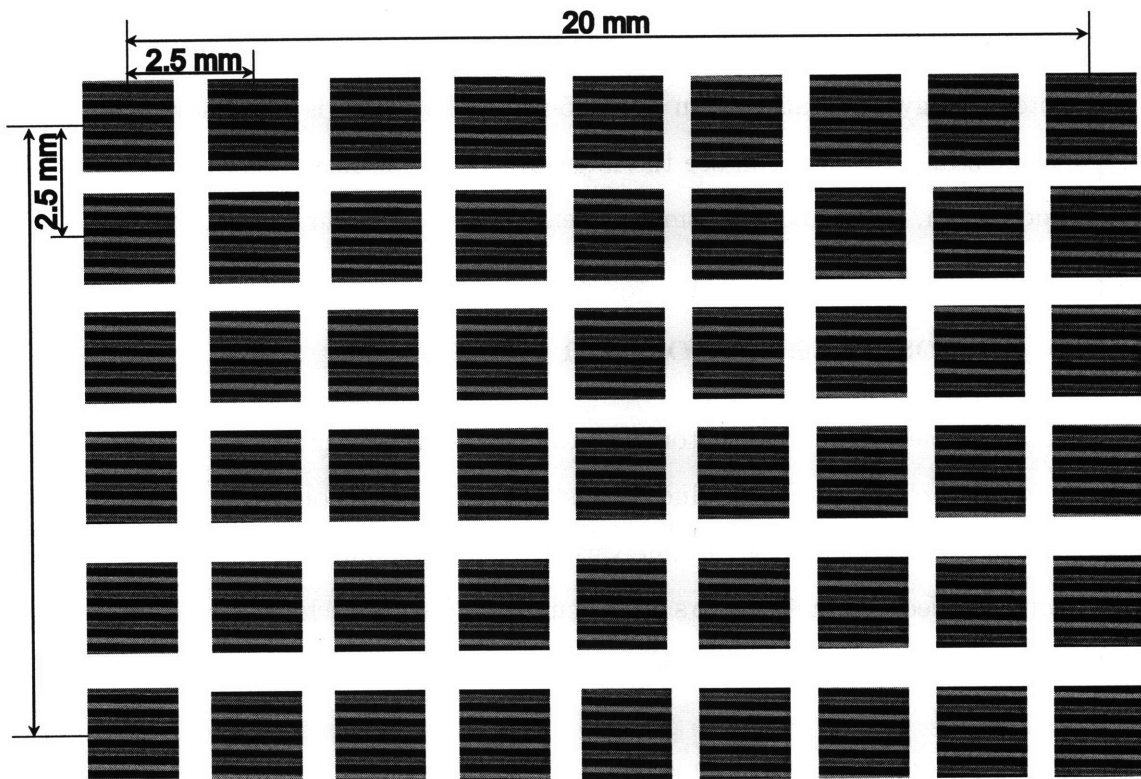


Figure 4-8: Top-view electron micrographs of two-level overlay results, taken by Raith 150 over $20 \times 12.5 \text{ mm}^2$ with a grid size of 2.5 mm . Each electron micrograph area is approximately $1.5 \times 1.5 \text{ }\mu\text{m}^2$.

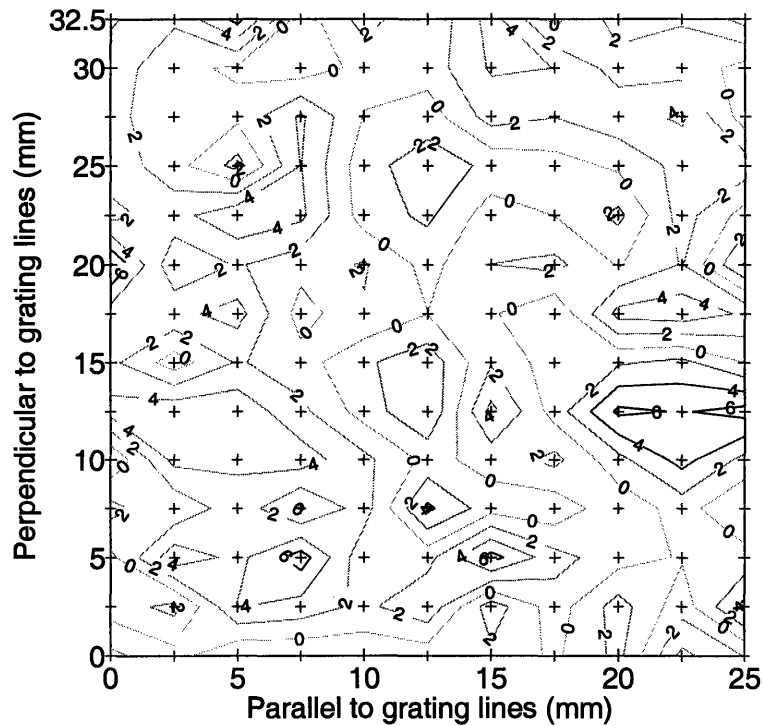


Figure 4-9: 2-D overlay phase error map (contours in nanometers) with a mean overlay error of $-1.0 \text{ nm} \pm 2.8 \text{ nm}$ (1σ).

extent. A vacuum pin chuck [27] is an alternative to minimize the particle problem.

4.5.2 The Nonlinear Distortion of the Alignment Grating

Nonlinear distortion of the alignment grating, which is mainly caused by particles between the substrate and the chuck during patterning of the alignment grating, will result in measured values of the angle, period, and phase that differ from those of the undistorted alignment grating. Local distortions of the alignment grating at start and end locations of the measurements for angle and period will cause errors in the measurement of the corresponding unwrapped grating phases and thus induce errors in the angle and period measurements. When measuring and resetting the phase of the alignment grating for the level 1 and level 2 patterns, if the local distortion at the measurement location for the level 1 pattern is different from that for the level 2 pattern, which easily occurs since the repositioning accuracy of the substrate is

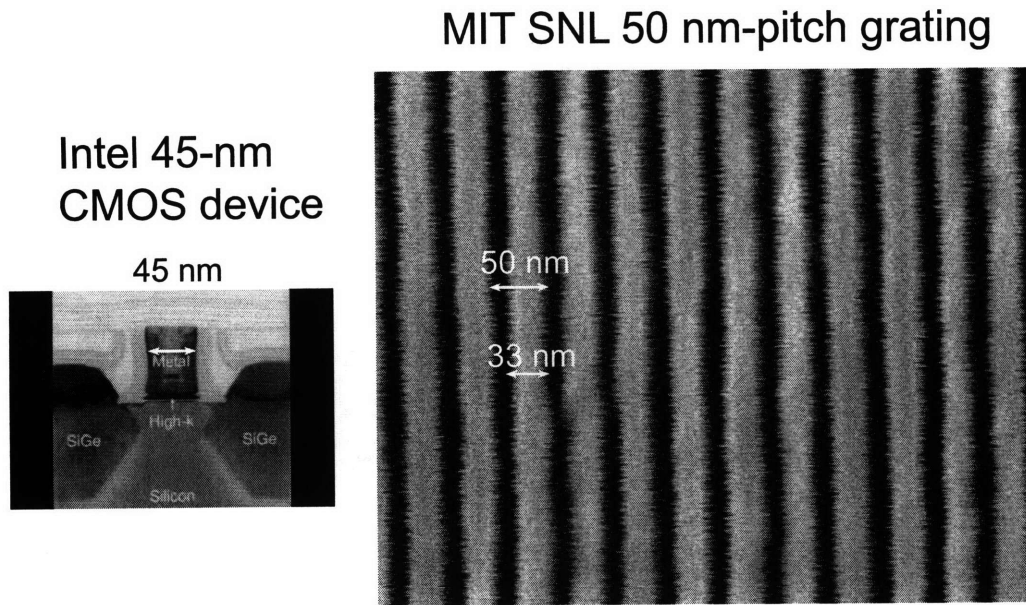


Figure 4-10: 50 nm-pitch grating patterns fabricated in MIT SNL and Intel 45-nm CMOS gate.

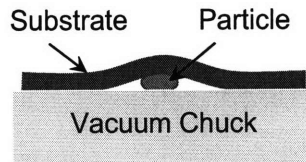


Figure 4-11: Depiction of substrate distortion due to particle between substrate and vacuum chuck.

only 1 ~ 2 mm, a constant overlay phase error over the whole overlay area will be introduced. The heterodyne reading mode provides an easy way to make a 2-D phase map of the alignment grating. Based on the phase map, non-distorted areas of the alignment grating can be selected to take the angle, period, and phase measurements and thereby avoid errors due to nonlinear distortions.

4.5.3 Pressure time-variance of the vacuum line of the chuck

Another factor causing substrate distortion is the pressure change of the vacuum line of the chuck, which was out of our original thinking. As shown in Fig. 4-13(a), the pressure of the chuck vacuum line has a 2-minute unstable phase every 10 minutes,

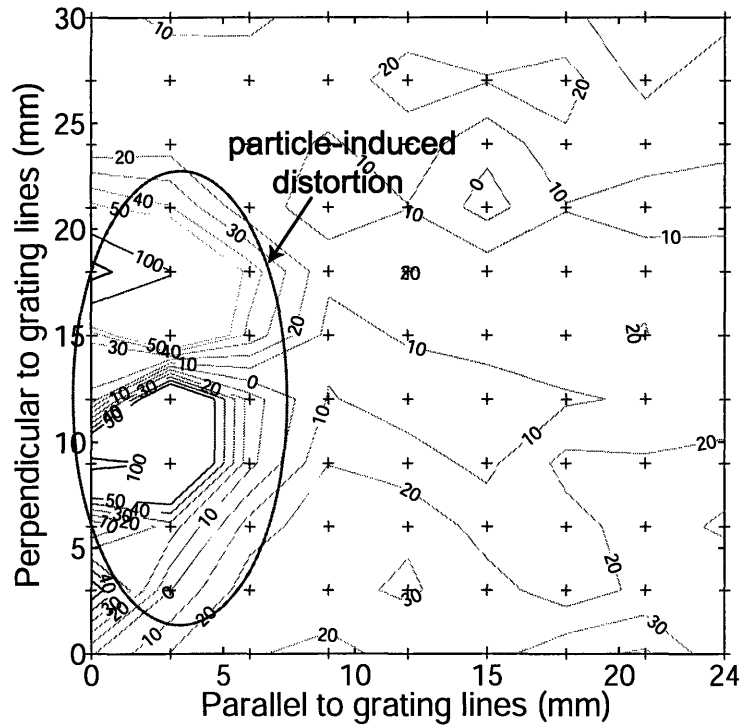


Figure 4-12: 2-D overlay phase error map (contours in nanometers) demonstrating particle-induced distortion.

which causes a large phase measurement error. The variation of the position measurement of the alignment grating, which corresponds to the phase measurement error of the alignment grating, is shown in Fig. 4-13(b). Besides of the phase measurement errors, pressure time-variance of the vacuum line can also induce phase error during patterning. After figuring out the problem, our lab manager, Mr. Robert Fleming, installed a dedicated vacuum pump system to improve the stability of the vacuum pressure and eliminate this effect.

4.6 Summary

In this chapter a phase control technique for accurately overlaying interference lithography exposures has been developed. The factors impairing phase control have been identified and corresponding approaches have been developed to minimize their impact. Based on the phase control technique, doubling the spatial frequency of a

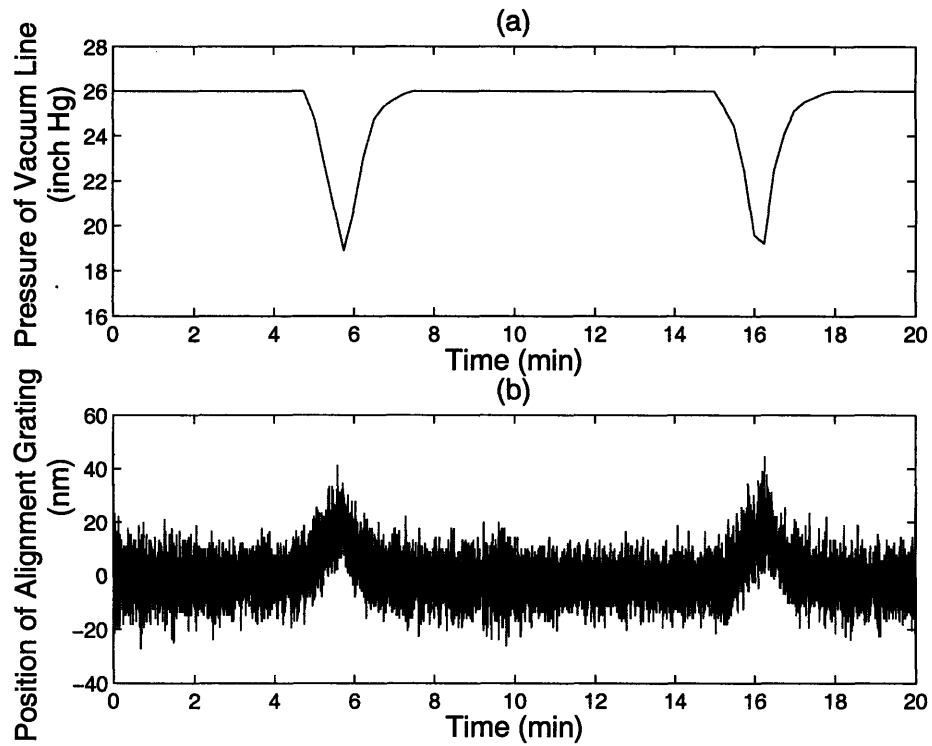


Figure 4-13: (a) Pressure measurement of the chuck vacuum line in 10 minutes. (b) Grating phase measurement with the heterodyne reading mode at the same time.

574 nm-pitch grating pattern has been achieved over a $25 \times 32.5 \text{ mm}^2$ area with an average overlay error of -1.0 nm and a 1σ deviation of 2.8 nm . Utilizing the same phase control technique, we have fabricated 50 nm-pitch grating patterns with spatial frequency quadrupling of a 200 nm-pitch grating pattern.

Chapter 5

Conclusions

In this thesis the main sources of error affecting the precision of the Nanoruler - thermal error of the environmental enclosure and the measurement errors of the X-axis stage mirror of the stage interferometry system - have been identified.

In order to reduce the thermal error, we designed a lead compensation controller together with a PI controller for the thermal control system of the environmental enclosure based on the measured system open-loop transfer function. Sub-millidegree air temperature stability at a single point inside the large-volume enclosure has been achieved. A method to rapidly monitor and map milli-degree temperature gradients over large volumes of enclosed space by mechanically scanning a network of thermistors has been developed and the temperature gradients within the critical tool volumes have been measured. Accurate cross calibration (within $1\text{ m}^\circ\text{C}$) of the thermistors has been performed. Self-heating errors have been shown to be less than $1\text{ m}^\circ\text{C}$. Sub-millidegree-relative-accuracy temperature gradients maps have been utilized to test the enclosure thermal system improvements.

A digital low-pass filter is utilized to reduce high spatial-frequency noise in the X-axis stage mirror non-flatness measurement. The factor that causes location-dependent mirror non-flatness measurement has been determined. A corresponding solution is developed to reduce this kind of error.

As an application of ultra-high precision patterning, multiple-exposure SBIL is utilized to multiply the spatial frequency of patterns over large areas. A phase con-

trol technique for accurately overlaying interference lithography exposures has been developed. A surrounding alignment grating is utilized as reference for subsequential patterns. Three key factors- the angle, period, and phase of the alignment grating- have been accurately measured and utilized to position subsequent patterns with respect to previous patterns. Some factors that can dramatically diminish the accuracy of phase control, such as particle-induced substrate distortion, nonlinear distortion of the alignment grating, and pressure time-variance of the vacuum line of the chuck, have also been considered and minimized in order to improve the accuracy of phase control. For spatial frequency doubling with a 574 nm principal pitch, we achieved overlay phase errors with a mean of $-1.0 \text{ nm} \pm 2.8 \text{ nm}(1\sigma)$ between overlaid grating patterns over a $25 \times 32.5 \text{ mm}^2$ area. Utilizing the same technique, we fabricated 50 nm-pitch gratings with spatial frequency quadrupling starting from a principal pitch of 200 nm.

In the future the next students can carry out 8-factor spatial frequency multiplication to fabricate 25 nm-pitch grating patterns starting with a principal pitch of 200 nm after shrinking the overlay phase error to less than 1.5 nm (1σ).

Appendix A

Matlab Codes for Mirror

Non-flatness Measurement

The following codes are used to recover the X-stage mirror non-flatness from the angle measurements θ_x and θ_y . Those angle measurements are given by a txt file "mirror713-1.txt". The codes are mainly based on Equations (3.18), (3.19), and (3.21).

```
HENERES = 3.236409608091024e+009; %counts/meter for stage interferometer
```

```
M=4000; N=2;
```

```
%Lets Now Find the Frequency Response B=zeros(3*N+1,1);
```

```
B(3*N+1,1)=-1; B(2*N+1)=-1; B(N+1)=1; B(1)=1;
```

```
figure(1);
```

```
zplane(B',1);
```

```
%Now for the Approximate Transfer Function q=roots(B)
```

```
A0=.85; % A0=.7;
```

```
z0=A0*exp(i*pi/2);
```

```
m=[.99,-.99,-z0,z0,-z0,z0];
```

```
q3=poly(m)
```

```
; figure(2);
```

```

zplane(q3,1);
filename = 'mirror713-1.txt';
data = load(filename); %X Theta, Y
dataextract2;
h=6.4; %mm %changed by Yong on Aug. 2nd, 2007
%h=6.375 %mm
figure(3);
[h2,w2]=freqz(q3,1,M);
[h1,w1]=freqz(B',1,M);
a=-1*abs(h2(400)/h1(400));
filtercoeff=1/a*q3;
[h2,w2]=freqz(filtercoeff,1,M);
freqz(filtercoeff,1,M);
hold on;
freqz(B',1,M);
yz_max=max(x(:,ycol));
yz_num=0; for i=1:size(x(:,ycol),1)
if ( yz_num ) && ( abs(x(i,ycol)-yz_max);1e5/2)
yz_num = i;
end
end
%***** Design Filter for Delta Theta
freNyquist=5; %Hz
Wp = 1.25/freNyquist;
Ws = 2/freNyquist; %Ws=3/freNyquist
[n,Wn] = buttord(Wp,Ws,3,40);
[b,a] = butter(n,Wn);
numExtra=max(length(a),length(b))-3; %delays
thetaxconv = 1/HENERES/(2*h*1e-3)*1e6;
startnum=7;

```

```

y=x(startnum:yz_num+numExtra,ycol)*1/HENERES;
xd=x(startnum:yz_num+numExtra,xcol)*1/HENERES;
xtheta=x(startnum:yz_num+numExtra,thetaxcol)*thetaxconv;
ytheta=x(startnum:yz_num+numExtra,ydaccol)*thetaxconv;
Comment="";
%***** Delta Theta
dtheta=(xtheta+ytheta);
c=sum(dtheta)/length(dtheta);
dtheta=dtheta-c;
%***** Filter Delta Theta
[dtheta_fil,zf]=filter(b,a,dtheta-dtheta(1));
dtheta_fil=dtheta_fil+dtheta(1);
%***** plot Delta Theta (before fil-
teration)
figure(4);
subplot(2,1,1);
plot(y(1:length(y)-numExtra)*1e3,dtheta(1:length(y)-numExtra));
ylabel('\Delta \theta (\murad)');
xlabel('Stage y position (mm)');
subplot(2,1,2);
four2=abs(fft(dtheta(1:length(y)-numExtra)))/sqrt(length(dtheta(1:length(y)-numExtra)));
xval=linspace(0,2,length(four2)); plot(xval,four2); xlim([0 1]);
xlabel('Normalized Frequency \omega /(f_s/2)');
ylabel('Frequency Content of \Delta\theta (\murad)');
%***** plot filtered
Delta Theta figure(5); subplot(2,1,1);
y=y(1:length(y)-numExtra)-0.000;
dtheta_fil=dtheta_fil(numExtra+1:length(dtheta_fil));
plot(y*1e3,dtheta_fil);
ylabel('\Delta \theta (\murad)');

```

```

xlabel('Stage y position (mm)')
subplot(2,1,2);
four2=abs(fft(dtheta_fil))/sqrt(length(dtheta_fil));
xval=linspace(0,2,length(four2)); plot(xval,four2); xlim([0 1]);
xlabel('Normalized Frequency  $\omega / (f_s/2)$ ');
ylabel('Frequency Content of  $\Delta\theta$  ( $\mu\text{rad}$ )');
figure(6);
xreconstruct=filter(4*h,filtercoeff,dtheta_fil-dtheta_fil(1));
plot(y,xreconstruct);
xlabel('Stage y position (mm)');
ylabel('Reconstructed MirrorProfile (nm)')
title(['Reconstructed Mirror Profile with Inverse Measurement Transfer Function'])
[P,S]=polyfit(y,xreconstruct,1);
linfit=polyval(P,y); hold on; plot(y,linfit,'k');
mirror=(xreconstruct-linfit);
figure(7);
subplot(2,1,1);
plot(y*1e3,mirror);
ylabel('Mirror nonflatness (nm)');
xlabel('Stage y position (mm)');
subplot(2,1,2);
plot(y*1e3,mirror);
ylabel('Mirror nonflatness(nm)');
xlabel('Stage y position (mm)')

```

Appendix B

Matlab Codes for Calculating Overlay Phase Error

The following codes are used to calculate the overlay position error between the level 1 and level 2 grating patterns. The information of the level 1 and level 2 patterns is provided by a top-view SEM image (e.g., "IMAGE090.bmp"). The algorithm of calculating the overlay position error is described as the following. We first separate two levels of grating patterns. Then we make fourier transform respectively on each level. The phase difference will given by subtracting the phase of the level 2 pattern from the that of the level 1. Finally convert this phase difference to the overlay position error.

```
clear all;
close all;
filename='IMAGE090.bmp';
img=imread(filename,'bmp');
ave=sum(img,2)/size(img,2);
figure;
plot(ave,'+');
background=min(ave)+20;
difference=3;
```

```

peakdown=1;
while (ave(peakdown)-ave(peakdown+1) <= difference)
peakdown=peakdown+1;
end
peakup=peakdown;
while (ave(peakdown+1)-ave(peakdown)<0)
peakdown=peakdown+1; end
while (peakup>0 & (ave(peakup+1)-ave(peakup)<=difference))
peakup=peakup-1;
end if (peakup<=0)
ave(1:peakdown)=background; end
while (peakup>0 & (ave(peakup)-ave(peakup+1)<0))
peakup=peakup-1;
end
if (peakup<=0)
ave(1:peakdown)=background;
end
if (ave(size(ave,1))> min(ave)+15)
backpeakup=size(ave,1);
while (ave(backpeakup)-ave(backpeakup-1) <= difference)
backpeakup=backpeakup-1;
end
while (ave(backpeakup)-ave(backpeakup-1)>0)
backpeakup=backpeakup-1;
end
ave(backpeakup:size(ave,1))=background;
end
peakdown=peakdown+10;
point=1024*100;
figure;

```

```

U = fft(ave,point);
Puu =sqrt( U.* conj(U) / point);
f = 1*(1:point/2)/point;
semilogx([10e-6,f],Puu(1:(point/2+1)));
title('Frequency Content of 2 layer Patterns')
xlabel('frequency (Hz)');
frestart=220;
[amax,fmax]=max(Puu(frestart:point/2+1));
spacing=point/(fmax+frestart-1-1);
periods=fix((size(img,1)-peakdown)/spacing/2+1);
z=ave;
y=zeros(size(img,1),1)+background;
for i=1:periods
if (peakdown+round(2*(i-1)*spacing) < size(img,1))
if (peakdown+round((2*i-1)*spacing) > size(img,1))
y(peakdown+round(2*(i-1)*spacing):size(img,1))=ave(peakdown+round
(2*(i-1)*spacing):size(img,1));
z(peakdown+round(2*(i-1)*spacing):size(img,1))=zeros(size(img,1)-
(peakdown+round(2*(i-1)*spacing))+1,1)+background;
else
y(peakdown+round(2*(i-1)*spacing):peakdown+round((2*i-1)*spacing))=
ave(peakdown+round(2*(i-1)*spacing):peakdown+round((2*i-1)*spacing));
z(peakdown+round(2*(i-1)*spacing):peakdown+round((2*i-1)*spacing))=
zeros(round((2*i-1)*spacing)-round(2*(i-1)*spacing)+1,1)+background;
end
end
end
bottom=0;
uplimit=190;
for i=1:size(img,1)

```

```

if y(i)<=background
y(i)=bottom;
end
if z(i)<=background
z(i)=bottom;
end
if y(i)>uplimit
y(i)=uplimit;
end
if z(i)>uplimit
z(i)=uplimit;
end
end figure;
plot(y);
figure;
plot(z);
figure;
Z = fft(z,point);
Pzz =sqrt( Z.* conj(Z) / point);
f = 1*(1:point/2)/point;
semilogx([10e-6,f],Pzz(1:(point/2+1)));
title('Frequency Content of One-layer Pattern')
xlabel('frequency (Hz)');
frestart1=220;
[amax1,fmax1]=max(Pzz(frestart1:point/2+1));
phase1=phase(Z(fmax1+frestart1-1));
figure;
Y = fft(y,point);
Pyy =sqrt( Y.* conj(Y) / point);
f = 1*(1:point/2)/point;

```

```
semilogx([10e-6,f],Pyy(1:(point/2+1)));  
title('Frequency Content of Another Layer Pattern')  
xlabel('frequency (Hz)');  
frestart2=220;  
[amax2,fmax2]=max(Pyy(frestart2:point/2+1));  
phase2=phase(Y(fmax2+frestart2-1));  
phase_difference=(phase2-phase1)/pi
```


Appendix C

Procedure of Measuring Non-flatness of the X-axis Stage Mirror

This appendix describes the procedure to measure the non-flatness of the X-axis stage mirror employing the Nanoruler 4.0 software, which was developed by Mr. Juan Montoya. This document mainly aims to provide some help to my colleagues in the Space Nanotechnology Laboratory on how to measure the X-axis stage mirror non-flatness.

First, load C programs to DSPs and run DSP A and B. Open the Nanoruler 4.0 and load C programs to DSP D. Hit the "feedforward on" button to make the stage homing and go back the center position.

Second, move the stage to an absolute position ($x=0.005$ m, $y=0.003$ m).

Third, set the velocity of the stage = 32 mm/s.

Forth, set data size = 200 under the menu of "Data".

Fifth, open the dialogue box under the menu of "Data". Check "X-theta", "Y-theta", "X-data", "Y-data", and "Down sample". Set "X position" = 0.005 m, "Y position" = 0.400 m, and "Downsample Factor" = 1000. Then click "OK" button. Immediately the stage starts to move.

Sixth, in 20 seconds transfer the data taken by DSP A to DSP D by click the "Data transfer (DSP A to DSP D)" button under the menu of "Data".

Seventh, when the data transfer is done, click the "Read Data" button to upload the data to a specified path in the Nanoruler computer as a specified name. (If needed, we can change the path and name in the right bottom dialogues.)

The X-axis stage mirror non-flatness can be recovered with the Matlab codes in the Appendix A.

Bibliography

- [1] C.A. Roos, Patterned magnetic recording media, *Annu. Rev. Mater. Res.*, 31, 2001.
- [2] A. Kikitsu, Y. Kamata, M. Sakurai, and K. Naito, Recent progress of patterned media, *IEEE Trans. Magn.*, 43, 2007.
- [3] S.H. Charap, P.L. Lu, and Y. He, Thermal stability of recorded information at high densities, *IEEE Trans. Magn.*, 33, 1997.
- [4] H.N. Bertram and M. Williams, SNR and density limit estimates: a comparison of longitudinal and perpendicular recording, *IEEE Trans. Magn.*, 36, 2000.
- [5] J.I. Martin, J. Nogues, K. Liu, J.L. Vicent, and I.K. Schuller, Ordered magnetic nanostructures: fabrication and properties, *J. of Magnetism and Magnetic Materials*, 256, 2003.
- [6] M.L. Schattenburg, C.G. Chen, R.K. Heilmann, P.T. Konkala, and G.S. Pati, Progress towards a general grating patterning technology using phase-locked scanning beams, *Proc. SPIE*, 4485, 2001.
- [7] C.G. Chen, P.T. Konkala, R.K. Heilmann, G.S. Pati, and M.L. Schattenburg, Image metrology and system controls for scanning beam interference lithography, *J. Vac. Sci. Technol. B*, 19, 2001.
- [8] P.T. Konkala, Design and analysis of a scanning beam interference lithography system for patterning gratings with nanometer-level distortions, *PhD dissertation, Massachusetts Institute of Technology, Department of Mechanical Engineering*, June 2003.
- [9] C.G. Chen, Beam alignment and image metrology for scanning beam interference

- lithography- fabricating gratings with nanometer phase accuracy, *PhD dissertation, Massachusetts Institute of Technology*, Department of Electrical Engineering and Computer Science, June 2003.
- [10] R.K. Heilmann, P.T. Konkala, C.G. Chen, G.S. Pati, and M.L. Schattenburg, Digital heterodyne interference fringe control system, *J. Vac. Sci. Technol. B*, 19, 2001.
- [11] K.P. Brich and M.J. Downs, Correction to the Updated Edlen equation for the refractive index of air, *Metrologia*, 30, 1994.
- [12] D. Sarid and D.S. Cannell, A ± 15 microdegree temperature controller, *Review of Scientific Instruments*, 45, 1974.
- [13] J. Dratler, A proportional thermostat with 10 microdegree stability, *Review of Scientific Instruments*, 45, 1974.
- [14] H. Ogasawara, Method of precision temperature control using flowing water, *Review of Scientific Instruments*, 57, 1986.
- [15] K.M. Lawton and S.R. Patterson, A high stability air temperature control system, *Precision Engineering*, 24, 2000.
- [16] P.T. Konkola, C.G. Chen, R.K. Heilmann, C. Joo, J. Montoya, C.-H. Chang and M.L. Schattenburg, Nanometer-level repeatable metrology using the Nanoruler, *J. Vac. Sci. Technol. B*, 21, 2003.
- [17] R.K. Heilmann, C.G. Chen, P.T. Konkola and M.L. Schattenburg, Dimensional metrology for nanometer-scale science and engineering: towards sub-nanometer accurate encoders, *Nanotechnology*, 15, 2004.
- [18] K.J. Astrom and B. Wittenmark, Computer-controlled systems: Theory and Design, *Prentice hall*, 3rd edition, 1996.
- [19] M.E. Harvey, Precision temperature-controlled water bath, *Review of Scientific Instruments*, 39, 1968.
- [20] K.M. Lawton and S.R. Patterson, Long-term relative stability of thermistors, *Precision Engineering*, 25, 2001.
- [21] K.M. Lawton and S.R. Patterson, Long-term relative stability of thermistors:

- Part2, *Precision Engineering*, 26, 2002.
- [22] ZYGO 2/20 Interferometer System Reference Manual OMP-0229B (Zygo Corp., Middle Field, CT), 1993
- [23] C.J. Evans, A.D. Davies, T. Schmitz, and R. Parks, Interferometric figure metrology; enabling in-house traceability, *Proc. SPIE*, 4450, 2001.
- [24] G. Schulz and J. Grzanna, Absolute flatness testing by the rotation method with optimal measuring-error compensation, *Applied Optics*, 34, August 1995.
- [25] J. Montoya, R.K. Heilmann, and M.L. Schattenburg, Measuring two-axis stage mirror nonflatness using linear/angular interferometers, *19th Annual Meeting of the American Society for Precision Engineering, Orlando, FL*, October 2004.
- [26] J. Montoya, Toward Nano-accuracy in Scanning Beam Interference Lithography, PhD dissertation, Massachusetts Institute of Technology, Department of Electrical Engineering and Computer Science, June 2006.
- [27] A. Une, P. Kunyoo, M. Mochida, K. Yoshitomi, and S. Matsui, A new vacuum pin chuck for ArF laser lithography, *Microelectronic Engineering*, Vol. 61-62, 2002.
- [28] S.R.J. Brueck, Optical and Interferometric Lithography - Nanotechnology Enablers, *Proceedings of the IEEE*, 93-10, 2005.
- [29] D.C. Flanders, A.M. Hawryluk, and H.I. Smith, Spatial period division - A new technique for exposure submicrometer-linewidth periodic and quasiperiodic patterns, *J. Vac. Sci. Technol.*, 16, 1979.
- [30] A.M. Hawryluk, et al., Deep-ultraviolet spatial-period division using an excimer laser, *Optics letters*, 7, 1982.
- [31] B.Cui, et al., Large area 50 nm period grating by multiple nanoimprint lithography and spatial frequency doubling, *Applied Physics Letters*, 90, 2007.
- [32] Z. Yu, et al., Fabrication of large area 100 nm pitch grating by spatial frequency doubling and nanoimprint lithography for subwavelength optical applications, *J. Vac. Sci. Technol. B*, 19, 2001.
- [33] S.H. Zaidi and S.R.J. Brueck, Nonlinear Process to Extend Interferometric Lithography, *Proc. SPIE*, 3676, 1999.

- [34] A.A. Freschi, et al., Phase-locking of superimposed diffractive gratings in photoresists, *Optics Communications*, 208, 2002.
- [35] Harry J. Levinson, Principles of Lithography, *SPIE Press*, 2nd edition, 2005.